Space Sci Rev
DOI 10.1007/s11214-016-0321-9

Selection of the InSight Landing Site

M. Golombek[1] · D. Kipp[1] · N. Warner[1,2] · I.J. Daubar[1] · R. Fergason[3] · R.L. Kirk[3] · R. Beyer[4] · A. Huertas[1] · S. Piqueux[1] · N.E. Putzig[5,6] · B.A. Campbell[7] · G.A. Morgan[7] · C. Charalambous[8] · W.T. Pike[8] · K. Gwinner[9] · F. Calef[1] · D. Kass[1] · M. Mischna[1] · J. Ashley[1] · C. Bloom[1,10,11] · N. Wigton[1,12] · T. Hare[3] · C. Schwartz[1] · H. Gengl[1] · L. Redmond[1,13] · M. Trautman[1,14] · J. Sweeney[2] · C. Grima[13] · I.B. Smith[5,6] · E. Sklyanskiy[1] · M. Lisano[1] · J. Benardini[1] · S. Smrekar[1] · P. Lognonné[15] · W.B. Banerdt[1]

Received: 8 June 2016 / Accepted: 22 November 2016

Abstract The selection of the Discovery Program InSight landing site took over four years from initial identification of possible areas that met engineering constraints, to downselection via targeted data from orbiters (especially Mars Reconnaissance Orbiter (MRO) Context Camera (CTX) and High-Resolution Imaging Science Experiment (HiRISE) images), to selection and certification via sophisticated entry, descent and landing (EDL) simulations. Constraints on elevation (≤ -2.5 km for sufficient atmosphere to slow the lander),

✉ M. Golombek
mgolombek@jpl.nasa.gov

1 Jet Propulsion Laboratory, California Institute of Technology, Pasadena, CA 91109, USA

2 Department of Geological Sciences, State University of New York at Geneseo, 1 College Circle, Geneseo, NY 14454, USA

3 Astrogeology Science Center, U.S. Geological Survey, 2255 N. Gemini Dr., Flagstaff, AZ 86001, USA

4 Sagan Center at the SETI Institute and NASA Ames Research Center, Moffett Field, CA 94035, USA

5 Southwest Research Institute, Boulder, CO 80302, USA

6 Present address: Planetary Science Institute, Lakewood, CO 80401, USA

7 NASM CEPS, Smithsonian Institution, 6th at Independence SW, Washington, DC 20560, USA

8 Department of Electrical and Electronic Engineering, Imperial College, South Kensington Campus, London, UK

9 German Aerospace Center (DLR), Institute of Planetary Research, 12489 Berlin, Germany

10 Occidental College, Los Angeles, CA, USA

11 Present address: Central Washington University, Ellensburg, WA 98926, USA

12 Department of Earth and Planetary Sciences, University of Tennessee, Knoxville, TN 37996, USA

13 Institute for Geophysics, University of Texas, Austin, TX 78712, USA

14 MS GIS Program, University of Redlands, 1200 E. Colton Ave., Redlands, CA 92373-0999, USA

15 Institut Physique du Globe de Paris, Université Paris Sorbonne, Diderot, Paris, France

Published online: 14 December 2016

latitude (initially 15°S–5°N and later 3°N–5°N for solar power and thermal management of the spacecraft), ellipse size (130 km by 27 km from ballistic entry and descent), and a load bearing surface without thick deposits of dust, severely limited acceptable areas to western Elysium Planitia. Within this area, 16 prospective ellipses were identified, which lie ~600 km north of the Mars Science Laboratory (MSL) rover. Mapping of terrains in rapidly acquired CTX images identified especially benign smooth terrain and led to the downselection to four northern ellipses. Acquisition of nearly continuous HiRISE, additional Thermal Emission Imaging System (THEMIS), and High Resolution Stereo Camera (HRSC) images, along with radar data confirmed that ellipse E9 met all landing site constraints: with slopes <15° at 84 m and 2 m length scales for radar tracking and touchdown stability, low rock abundance (<10 %) to avoid impact and spacecraft tip over, instrument deployment constraints, which included identical slope and rock abundance constraints, a radar reflective and load bearing surface, and a fragmented regolith ~5 m thick for full penetration of the heat flow probe. Unlike other Mars landers, science objectives did not directly influence landing site selection.

Keywords Mars · InSight, Landing Site · Surface characteristics · Landing ellipse · Corinto secondaries · Rocks · Terrains, Surface slope · Regolith · Radar

1 Introduction

The InSight (**In**terior Exploration using **S**eismic **I**nvestigations, **G**eodesy and **H**eat **T**ransport) mission is a Discovery Program lander to investigate the internal structure of Mars and the differentiation of the terrestrial planets (Banerdt et al. 2013). The spacecraft carries a seismometer (SEIS, Lognonné et al. 2015), heat flow probe (Heat Flow and Physical Properties Package, HP^3, Spohn et al. 2012) and a precision tracking system (Folkner et al. 2012) to measure the size and state of the core, mantle and crust. The lander is designed to operate on the surface for one Mars year after landing (November 2018) listening for marsquakes and impacts, measuring the heat flow (including the surface temperature), and tracking the precession and nutation of the spin axis. The spacecraft also carries a meteorology package, a magnetometer, two color cameras, and an arm to image the surface and deploy the instruments onto the surface that together allow investigations of the atmosphere, surface geology and physical properties of surface materials (Banerdt et al. 2013).

The spacecraft is based on the Phoenix (PHX) lander and consists of a cruise stage, aeroshell, and backshell. After launch in May 2018, and cruise to Mars, the spacecraft enters the atmosphere directly from approach and uses the aeroshell and friction of the atmosphere to initially slow itself. A parachute further slows the spacecraft and the heat shield is jettisoned. The lander uses a radar altimeter to measure the closing distance to the surface, deploy the lander legs, separate from the parachute, and throttle descent engines that slow the lander to touchdown on three legs, with the arm facing south. After landing, the spacecraft unfurls two large solar panels for power and after checkout, begins imaging the lander and martian surface. The workspace that the instruments can be deployed in by the arm will be imaged in stereo to select smooth and flat sites to deploy the SEIS and HP^3 instruments. After the seismometer is deployed, it levels itself, and a wind and thermal shield (WTS) is placed over it. Then the HP^3 instrument is deployed and the mole percussively hammers itself to a depth of up to 5 m.

The process for selecting the InSight landing site was broadly similar to that used for selection of the Mars Pathfinder (MPF) (Golombek et al. 1997), the Mars Exploration Rover

(MER) (Golombek et al. 2003a), PHX (Arvidson et al. 2008) and MSL (Golombek et al. 2012a) landing sites, which involved close coordination between the engineering and science teams to identify potential landing sites and to assess their safety. Engineering constraints on the landing sites were fairly mature at the beginning of the project, because they were largely inherited from the PHX landing site selection (Arvidson et al. 2008; Spencer et al. 2009; Adams 2008; Bonfiglio et al. 2011) and changed only modestly during project development. Elevation, latitude and ellipse size requirements more severely limited acceptable areas on Mars for consideration than any other successful selection activity. Like MSL, data gathered by orbiters, mostly MRO, during the selection process allowed detailed characterization of the landing site as well as definition of the atmosphere. A major difference from previous landing site selections is that there are no science objectives that influence the location of the landing site. Although there are several instrument deployment requirements, the science objectives of the mission can be met anywhere on Mars where the spacecraft can land safely and deploy the instruments. Finally, because the spacecraft does not move after landing, evaluation of traversability was not necessary (e.g., Golombek et al. 2012a).

Selection of the InSight landing site took over four years during project development, spacecraft assembly, and testing (Table 1). The GEophysical Monitoring System (GEMS) Discovery Program proposal submitted to NASA in September 2010 had already identified preliminary engineering constraints and identified western Elysium Planitia as a location that appeared to meet them in remote sensing data. After GEMS was selected for a Phase A study, the project evaluated and wrote these landing site engineering constraints as requirements. The latitude, elevation and ellipse size requirements were mapped onto Mars and global image mosaics and rock abundance derived from thermal data examined. Sixteen ellipses were identified in western Elysium Planitia that met the requirements in remote sensing data, and to dramatically reduce the mission design trade space all other areas were eliminated. By the time of the Concept Study Report (March 2012) and the site visit (May 2012) at the end of the now renamed InSight project Phase A, a few high-resolution images had been acquired in the region. InSight was selected as a Discovery Mission in late August 2012 and work began on Phase B. Because MSL is due south of the western Elysium landing site region (150–675 km) and MRO is in a near polar orbit, work with MRO began to determine how to communicate with MSL and take an image of the InSight landing site area on the same orbital pass. In addition, a Memorandum of Agreement with the Mars Exploration Program was prepared to provide landing site imaging, atmosphere characterization, and communications support for the InSight Mission. In less than one year, CTX (Malin et al. 2007) had acquired images at 6 m/pixel covering approximately 90 % of the landing site region. These images were of tremendous benefit, as terrains in the area could be identified and mapped. By the First Landing Site Workshop (June 2013), an additional six ellipses were identified and approximately 20 HiRISE (McEwen et al. 2007) images were acquired and HiRISE images of the landing site were being targeted and acquired at a rate of one per week. HRSC images (Neukum and Jaumann 2004; Jaumann et al. 2007) had been acquired and were being made into a digital elevation model (DEM). The project downselected to four ellipses (E9, E17, E5 and E8) in the northern part of the region in July 2013. The Second Landing Site Workshop, which included a peer review of the data products being produced and their use, occurred in September 2014 and the project provisionally selected ellipse E9 in January 2015 and eliminated backups in May 2015. The Third Landing Site Workshop (September 2015) included full hazard maps and landing simulations and was followed closely by an Independent Peer Review and Project Landing Site Certification and a Planetary Protection Review in October 2015. NASA Headquarters officials were briefed on the selection of the landing site in December 2015.

Table 1 Major InSight landing site selection activities

Date	Activity
9/10	GEMS Discovery Proposal Submitted Preliminary engineering constraints determined Western Elysium Planitia identified as area that met constraints
5/11	GEMS Selected for Phase A Study
3/12	InSight Concept Study Report Submitted Engineering constraints written as project requirements Regions that meet elevation, latitude and ellipse size mapped 16 ellipses in western Elysium Planitia selected Other areas eliminated, First few HiRISE and CTX images acquired
8/12	InSight Selected as Discovery Mission
6/13	First Landing Site Workshop MEP MOA[a] to support landing site imaging, atmosphere characterization and communications Conflict of imaging landing site and communication with MSL resolved CTX images 90 % area, 20 HiRISE images, terrains mapped 22 ellipses identified, Thermal/power studies prefer 3–5°N latitude
7/13	First downselection, Four ellipses selected (E9, E17, E8, and E5)
2/14	Council of Terrains and Council of Atmospheres formed
9/14	Second Landing Site Workshop, ~50 HiRISE images of 4 ellipses Peer review of data products and their use, Creation of hazard maps
1/15	Second downselection, Engineering landing simulations Ellipse E9 provisionally selected
5/15	Ellipse E9 selected, Backup sites eliminated, ~40 HiRISE images of ellipse E9
9/15	Third Landing Site Workshop ~50 HiRISE images of ellipse E9, Hazard maps and landing simulations of ellipse E9
10/15	Independent Peer Review and Project Landing Site Certification
10/15	Planetary Protection Review of Selected Landing Site
12/15	NASA Headquarters Briefing
12/15	InSight launch in 2016 suspended
3/16	InSight reconfigured and authorized for 2018 launch by NASA No change to landing site

[a]Mars Exploration Program Memorandum of Agreement

The InSight launch, originally scheduled in 2016, was suspended in late December 2015 due to a leak in the SEIS vacuum sphere. The project was reconfigured for a 2018 launch and authorized by NASA to proceed with development. The 2018 launch opportunity is generally more favorable than 2016, with less propulsion needed for the transfer trajectory, lower entry velocity at Mars, and an almost identical atmospheric pressure at arrival. Similar atmospheric pressure translates into the same elevation constraints as for 2016. The other

Table 2 Membership and analyses of the InSight Council of Terrains

Data product and surface characterization	Investigator
Terrain Mapping	N. Warner, JPL & SUNY Geneseo, N. Wigton, U. Tennessee, Knoxville
MOLA slope, RMS slopes, Allen deviation, and pulse spread	M. Golombek[a], JPL, C. Bloom, Occidental
HRSC DEM	K. Gwinner, DLR
HiRISE and CTX DEMs, slope statistics Integrated hierarchical DEM	R. Kirk, R. Fergason, USGS Flagstaff
HiRISE photoclinometry slope maps	R. Beyer, SETI Institute & NASA Ames
Rock maps and size-frequency distributions	A. Huertas, M. Golombek, D. Kipp N. Warner, J. Ashley, JPL
Radar and SHARAD surface and subsurface analysis	N. Putzig, SwRI, B. Campbell, Smithsonian
Thermophysical Properties	S. Piqueux, JPL
Rocky ejecta craters, regolith thickness	N. Warner, JPL & SUNY Geneseo, M. Golombek, JPL, C. Charalambous & T. Pike, Imperial
Corinto secondary analysis	C. Bloom, Occidental, I. Daubar, M. Golombek, JPL
Cartography and data product registration Hazard maps	F. Calef, N. Warner, I. Daubar, JPL
Landing simulations and safety	D. Kipp[a], JPL

[a]Co-Chairs

major constraints on the landing site (ellipse size and azimuth, and latitude) are also largely unchanged, leading to the same region in Elysium Planitia and no change in the landing site location (within a few km).

The landing site selection activity for InSight was carried out within the JPL project without open workshops with the science community for two reasons. First, because the InSight project is a competed mission through the Discovery Program and the landing site selection was part of the proposal, it was handled similar to other competed missions in which site selection was part of the proposal (e.g., PHX Scout Mission, Arvidson et al. 2008). Second, because the science objectives of InSight can be met almost anywhere on the planet, there are no science factors that feed into landing site selection. Consequently, landing site selection requirements centered solely on landing site safety and instrument deployment requirements, rather than landing site geology that the science community is typically asked to evaluate in open landing site workshops. Nevertheless, the expertise of the science community was solicited on topics relevant to landing safety via a request for proposals issued by JPL that focused on surface and subsurface properties relevant to landing and instrument deployment and on defining atmospheres for EDL. In February 2014, the 'Council of Terrains' and the 'Council of Atmospheres' were established to provide specific data products to the project with membership composed of awardees as well as interested members of the science team (Table 2). The overall landing site selection process was managed by InSight Co-Investigator, M. Golombek, who is the Geology and Landing Site Lead for the project. He co-chaired the Council of Terrains with D. Kipp, the engineer leading the landing simulations. The Council of Atmospheres was chaired by D. Kass. Landing site activities and atmosphere definition were reported internally to the project through the EDL and system engineering teams and were included in all project reviews during development. In addi-

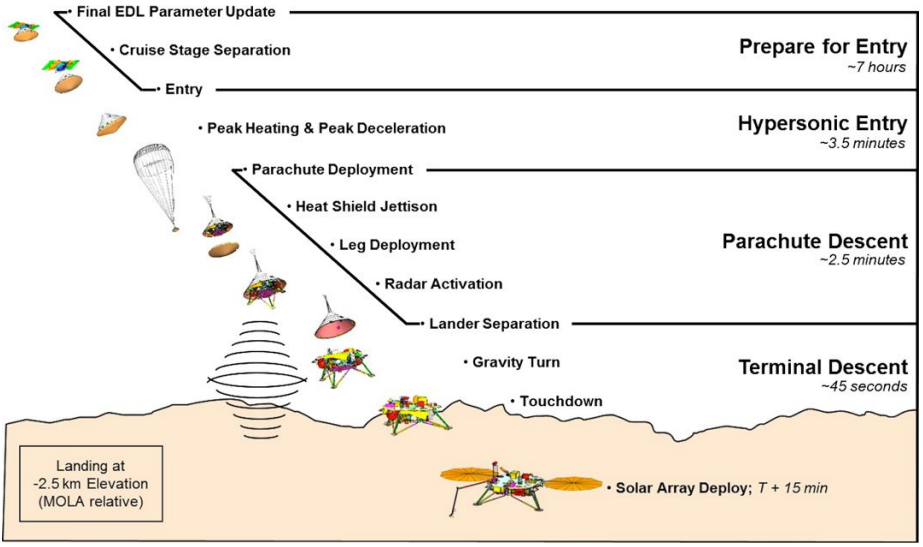

Fig. 1 Graphical depiction of critical events during InSight's entry, descent and landing

tion, members of the standing review board of the project attended all project landing site downselection meetings.

This paper documents the selection of the InSight landing site. We begin by describing the engineering (e.g., ellipse size, latitude, elevation, slopes, rocks and surface properties), instrument deployment, and planetary protection constraints on landing site selection (Sects. 2 and 3). Next we describe the data and models used to evaluate surface characteristics and the definition of the atmosphere used for EDL analysis (Sects. 4 and 5). Because landing site selection decisions are based on incomplete information (e.g., only the images acquired and work accomplished up to that time), a description of the history of landing site selection is required to understand why the final landing site was selected. As a result, the landings site history is described along with the downselections and decisions made during the process, including the independent peer and planetary protection reviews (Sect. 6). The surface characteristics of the landing sites are described and compared to other landing sites and the engineering constraints (Sect. 7), and landing success is assessed via engineering simulations of landing (Sect. 8) on hazard maps derived from surface data products (maps of slopes and rocks).

2 Landing Site Constraints

2.1 Entry, Descent and Landing

InSight's EDL architecture is inherited directly from the PHX mission that landed safely on Mars in May 2008. Only minor modifications to the system implementation and EDL profile were necessary to accommodate differences between the 2008 and 2016 or 2018 mission opportunities.

The InSight EDL sequence of events is shown in Fig. 1. Preparations for entry begin 10 minutes prior to atmospheric entry—defined to occur at a radius of 3522.2 km from the

center of the planet. In this period, the spacecraft jettisons the cruise stage and orients itself so that the nose of the heatshield is aligned with the planet-relative velocity vector when the vehicle encounters the atmosphere. The entry vehicle is a 2.65 m diameter aeroshell with a 70° half angle heatshield, a heritage geometry established by the Viking landers and maintained through all subsequent NASA Mars landers. Like PHX, the vehicle's trajectory is unguided and spacecraft attitude is 3-axis controlled during hypersonic flight. Attitude control limits are wide to avoid unnecessary thruster activity for the aerodynamically stable entry vehicle.

Parachute deployment is triggered autonomously based on on-board estimates of navigated velocity and measurements of vehicle acceleration. Trigger thresholds are parameterized and tuned to deploy the parachute as soon as the dynamic pressure is low enough to ensure that parachute inflation loads will be below the flight limit of 15,000 lbf. Following parachute deployment, an onboard sequence commands heatshield separation, leg deployment, and radar activation according to a pre-defined timeline. The Phoenix heritage radar begins obtaining ground-relative measurements of altitude and velocity once the vehicle descends to approximately 2.5 km above the surface and lander separation is triggered once the combination of ground-relative altitude and velocity meet the conditions for initiation of terminal descent.

Terminal descent begins with lander separation at an altitude between 1000 m and 1500 m above the surface. Terminal descent consists of: 1) a short period of free-fall to clear the lander from the backshell, 2) a turn to orient the thrust vector in the desired direction, 3) a constant deceleration-modified gravity turn to reduce vertical velocity and nominally eliminate horizontal velocity, and 4) a transition to constant velocity vertical descent at 2.4 m/s. Touchdown is detected once the lander legs come into contact with the surface and the descent engines are shut down.

The EDL scenario and spacecraft and sensor capabilities are what define the engineering constraints on landing sites described next and summarized in Table 3.

2.2 Latitude

Work for the GEMS proposal used PHX-build-to-print solar arrays and battery design and required the lander to operate for the entire Martian year in conservative dust opacity conditions. Analysis of power with this design required that the lander be in a latitude band from 1°N to 14°S (Lisano and Bernard 2014). During Phase A, the project incorporated larger-area solar arrays, grown to the mechanical limit that could fit folded-up inside the PHX-heritage entry aeroshell, with newer, higher-efficiency photovoltaics, plus a higher-charge-capacity battery design, thereby expanding the northern landing site latitude limit to 5°N. As described in Sect. 6.2, this opened up a large number of potential landing sites in western Elysium Planitia during Phase A. During Phase B, and by the Second Landing Site Downselection, the latitude band was narrowed to 3°N to 5°N, to enable deployment and science operations under worse case atmospheric and thermal conditions. The northern latitude limit was established around perihelion with arrays tilted north in worst observed global dust storm conditions and a southerly noontime sun. The southern latitude limit resulted from powering instrument heaters each sol in the cold, clear conditions around aphelion, with arrays tilted south and a northerly noontime sun. As described in Sect. 6.6, this narrower latitude range directly influenced the selection of the four northern ellipses at the Second Landing Site Downselection.

Table 3 Landing site engineering constraints

Parameter	Requirement	Origin
Latitude	15°S to 5°N (initial) 3°N to 5°N	Power Thermal management
Elevation	<-2.5 km with respect to MOLA geoid	Sufficient atmosphere to slow spacecraft
Ellipse dimension	130 km by 27 km Roughly E-W at middle of launch period	Ballistic trajectory
Rock abundance	<10 %	$<\sim$1–2 % probability of failure at touchdown Sufficiently few rocks >6 cm diameter to deploy instruments
Slopes at		
1–5 m length scale	$<15°$	Touchdown stability Leveling limit of SEIS
84 m length scale	$<15°$	Radar tracking
Fragmented regolith	3–5 m thick	Full penetration of HP^3 mole
Radar reflectivity	C band radar reflective	Radar returns during descent
Load bearing surface; No thick dust deposits	Thermal inertia >100–140 J m^{-2} K^{-1} s$^{-1/2}$	No sinkage during touchdown Solid surface for SEIS Low dust accumulation on solar panels

Table 4 Main differences between InSight in 2016 and 2018 and PHX that affect EDL

	InSight 2018	InSight 2016	Phoenix
Arrival Date	November 26, 2018	September 28, 2016	May 25, 2008
Inertial Entry Velocity (km/s)	5.5–5.6	6.1	5.6
Entry Mass (kg)	<625	<625	572.2
Landing Site Elevation (km, MOLA)	<-2.5	<-2.5	-4.1
L_s/Season	296° (Northern Winter, Southern Summer, Late Global Dust Storm Season)	226° (Northern Autumn/Southern Spring, Global Dust Storm Season)	76.7° (Northern Late Spring)
Surface Atmospheric Pressure (mbar) at Landing Site	7.3	7.4	8.5

2.3 Elevation

Early during project formulation the EDL team was tasked to define a maximum landing elevation capability to constrain the search for a suitable landing site. This effort required first capitalizing on the excess margin inherent in the EDL timeline to accommodate increases in entry velocity and spacecraft mass relative to the PHX opportunity (Table 4), as well as differences in the atmosphere due to a different season at arrival. Subsequently, remaining

excess margins were assessed to determine the maximum landed altitude capability. It was determined that landing elevations as high as −2.5 km with respect to the Mars Orbiter Laser Altimeter (MOLA) geoid (Smith et al. 2001a, 2001b) were achievable while retaining safe altitude and timeline margins consistent with the maturity of the design. During Discovery proposal preparation and the initial search for landing sites, it became clear that any increase in elevation would severely reduce the number of potential landing sites (Sects. 6.1 and 6.2).

As the design matured, and improved atmospheric models became available for the arrival season (Sect. 5), the EDL margins became unacceptably small. To preserve the ability to land safely at the defined altitude of −2.5 km, the maximum allowable parachute inflation load was increased from 12.7 klbf to 15 klbf by making structural modifications to both the lander and the parachute. This change enabled recovery of lost margins, and preserved the ability to land at −2.5 km, by allowing the parachute to be deployed earlier during the EDL sequence.

2.4 Ellipse Size

The ellipse dimension specification (130 km by 27 km) is based on the estimated landing accuracy of the vehicle relative to a target location. The ellipse is specified such that there is a 99 % probability of landing within an ellipse of the specified dimensions centered at a particular target location. Primary factors dictating the size of InSight's landing ellipse are: 1) navigated position and attitude state and uncertainty at entry, 2) atmospheric uncertainties related to encountered wind and density profiles, and 3) vehicle aerodynamic uncertainties.

The estimated landing ellipse dimensions have fluctuated as the project matured. Initial study during the Discovery proposal preparation identified a 150 km by 30 km ellipse (Sect. 6.1), but during Phase A, an ellipse of 130 km by 27 km was defined and has remained unchanged since. Notable factors include: 1) larger than expected atmospheric dispersions associated with the potential for a global dust storm coincident with InSight's arrival led to an increased ellipse size, and 2) subsequent tightening of the entry flight path angle error requirement from 0.3° down to 0.21° reduced ellipse size. Analysis of the selected landing region has shown that ellipse sizes ranging from 85 km by 20 km to 150 km by 35 km are possible depending on the state of the atmosphere during EDL (Sect. 5).

2.5 Radar Reflectivity and Surface Dust

The surface of the landing site must be radar reflective and bear the load of the spacecraft at landing and instruments at deployment. These requirements constrain the radar and thermophysical properties of the surface materials, including albedo, thermal inertia (resistance to a change in temperature, see full definition in Sect. 7.3), and radar reflectivity (and inferred bulk density).

The landing radar on InSight, as on PHX, uses a 1.3 GHz (C-Band) pulsed radar for both altimetry and velocimetry. PHX developed a high-fidelity radar model with the goal of faithfully representing hardware, software, and environmental effects that influence the radar's accuracy. The EDL simulation uses a radar scattering model that is varied well beyond the bounds of the expected backscatter properties based on surface observations. The simulation has demonstrated that the radar is robust to a wide range of surface reflectivity properties.

Broad tracts of Mars with very low thermal inertia and high albedo have been interpreted to be loose atmospherically-deposited dust (e.g., Christensen and Moore 1992; Mellon et al. 2008). Experience and extrapolation from the existing landing sites argues that loose dusty material is not load bearing (e.g., Christensen and Moore 1992; Golombek et al. 2008a).

In addition, radar reflectivity is related to the bulk density of dry materials, so areas with low radar reflectivities might have surfaces with low bulk density (e.g., see Golombek et al. 1997 and references and discussion therein). Global thermal inertia and albedo data show a mode with thermal inertias less than 100 $J\,m^{-2}\,K^{-1}\,s^{-1/2}$ and albedo higher than 0.25 that corresponds with these very dusty surfaces (Putzig et al. 2005; Mellon et al. 2008) that could be meters (Christensen and Moore 1992) to tens of meters thick (Mangold et al. 2009). Surfaces with these characteristics are not suitable for landing spacecraft, driving rovers, or firmly placing instruments (e.g., Golombek et al. 1997, 2003a, 2012a). Finally, because InSight is a long-lived, solar powered lander and experience with the solar-powered MER Spirit and Opportunity in which dustier locations (Spirit) have greater dust buildup on the panels (and fewer dust cleaning events) (Stella and Herman 2010), the thermal inertia is further restricted to $>140\,J\,m^{-2}\,K^{-1}\,s^{-1/2}$. The Gusev cratered plains where Spirit landed has a dust cover index (DCI) of 0.93–0.97 (Ruff and Christensen 2002) and landing sites that are no dustier than this (i.e., DCI > 0.93) are preferred.

2.6 Rock Abundance

The lander's ability to tolerate rocks varies depending on the touchdown velocity and local topography at the landing site (see Sect. 8.1.3). The lander is tolerant of rocks up to 45 cm high underneath a footpad, rocks up to 45 cm high underneath the lander, and rocks up to 55 cm high underneath the deployed solar arrays and 10 cm less in all cases if excess energy is absorbed by crushable material inside the lander legs. If the rock size-frequency distribution (SFD) is similar to models based on measured distributions at existing landing sites (e.g., Golombek and Rapp 1997; Golombek et al. 2003b, 2008b, 2012b), then this translates to an overall rock-induced failure rate of ~0.35 % in regions with a 5 % cumulative fractional area (CFA) and a failure rate of ~2.5 % in regions with a 10 % CFA.

In the GEMS proposal, a rock requirement of 10 % CFA was imposed on the landing site. This requirement was based on the PHX requirement, which necessitated that "one or both" solar arrays be deployed to enable mission success. InSight has since modified this requirement to necessitate that both solar arrays be deployed to enable mission success.

2.7 Surface Slopes

Surface slope constraints exist at two different baselines. At lander length scales (1–5 m), a requirement of $<15°$ is imposed to ensure stability of the lander during touchdown and to ensure proper orientation of the lander vehicle during surface operations. This requirement is inherited directly from the PHX lander. Monte Carlo simulations of the touchdown event performed using multibody simulation software (ADAMS) demonstrated a 0 % probability of tipover when landing within EDL specifications on planar surfaces having slopes up to 15°. When simulating touchdown on planar surfaces of 20°, the tipover rate increased to 10 % indicating there is a graceful degradation in vehicle performance as surface slopes exceed 15°.

A separate requirement of $<15°$ slope is imposed at an 84 m length scale to ensure that the landing radar performs as expected during EDL over the selected site. Specifically, the concern is that surface slopes can result in velocity knowledge errors that may result in out-of-spec horizontal velocity magnitudes at touchdown. The relevant length scale (i.e., 84 m) is determined from the diameter of the terrain being queried by the radar when the vehicle transitions to the constant velocity portion of terminal descent (i.e., altitude of $\leq$250 m). A 15° slope at this length scale would contribute ~0.6 m/s of horizontal velocity error at touchdown. This error is treated as a sub-allocation of the overall horizontal velocity requirement of <1.4 m/s at touchdown.

2.8 Instrument Deployment

After landing, the SEIS, WTS and the HP^3 must be placed on the surface from the deck using the arm. The instruments must be placed on a smooth, relatively flat surface with their feet placed firmly on the ground. This results in slope, rock, and material property constrains on the location where they are placed. The arm can place the instruments in an annular workspace 0.5 to 2 m away from the lander over a little less than 180° of arc ($\sim$7 m^2, depending upon the instrument) south from the lander. Preferred locations from noise considerations would place the SEIS to the west and HP^3 to the east, both as far away from the lander and each other as possible.

The instruments can accommodate rocks or relief of up to 3 cm. The WTS can accommodate up to 6 cm relief and must be placed over the SEIS without touching it. In addition, SEIS has a leveling system that can accommodate slopes up to 15°. The long axis of the HP^3 and the diameter of the SEIS are around 0.5 m and the WTS is just over 0.7 m diameter. Because slopes at the landing sites can be measured using photoclinometry at 0.25 m and in DEMs at 1 m per elevation posting (Sect. 7.6), the same 1 % area greater than 15° slope constraint for landing was adopted for the instruments. In addition, the SEIS feet must be placed firmly on the surface with no pebbles under their feet. This requires that no dust obscures the surface, and both instruments must be placed on load bearing soils. There was some discussion early on during project development to deploy the SEIS on bedrock, but it was viewed as impractical and contrary to the requirement for a fragmented regolith needed for penetration of the HP^3 mole (Sect. 2.9). These requirements are consistent with the landing site requirements on a load bearing surface and no thick deposits of dust (Sect. 2.5).

The 3 cm and 6 cm height of a rock beneath the instruments and WTS, respectively, was evaluated for different rock abundances using three techniques. The first technique used rock maps at the three fixed landers with arms: Viking Lander 1 (VL1), Viking Lander 2 (VL2), and PHX. Two InSight deployment areas were located in each surface rock map (Moore and Keller 1990, 1991; Arvidson et al. 2009; Heet et al. 2009), and evaluated for the number of SEIS/WTS and HP^3 deployments in each for the local rock abundance. Results indicated that for the landing constraint of 10 % rock abundance, there should be multiple SEIS/WTS (3–11) and HP^3 (6–15) deployment sites that are free from 6 cm diameter (3 cm high) rocks. The second technique used Poisson statistics to evaluate the probability that a rock of a given diameter or larger would be present in a single random sample of a given area for a given rock abundance, which has been used to evaluate the probability of failure for landing MER, PHX and MSL in observed and modeled rock abundances (Golombek et al. 2003b, 2008b, 2012b). The placement probabilities were determined for multiple discrete placement options for each instrument and WTS in the workspace and then made conditional on finding locations that are free from rocks >6 cm diameter for both instruments for a 10 % model rock abundance. Results indicate at least a 99 % probability of having at least one SEIS/WTS and 6–10 HP^3 acceptable deployment sites within the workspace. The third technique involved generating an 8000-case Monte Carlo simulation of rock fields that match the exponential SFD model for 10 % total rock abundance (Golombek and Rapp 1997; Golombek et al. 2003b, 2008b, 2012b) and identifying instrument placement locations. Results agree with the analytic probability calculations. As a result, all three techniques indicated that landing surfaces that meet the landing site slope (<1 % area >15°) and rock abundance requirements (<10 % rock abundance) would also be acceptable for deploying the instruments.

2.9 Fragmented Regolith >3–5 m Thick

The HP^3 mole is designed to percussively penetrate 3–5 m below the surface to measure the heat flow in one Martian year. The thermal gradient below 3 m is unaffected by the annual temperature wave, and can thus be measured as soon as the mole and tether come to thermal equilibrium. If the mole penetrates to 3 m, the thermal gradient between 2 and 3 m will include a small amplitude temperature change due to the annual thermal wave. Thus the thermal gradient measurement requires a longer duration—approximately half a martian year—to allow for monitoring the annual wave temperature variation so that it can be removed from the gradient due to interior heat. Testing of the mole shows it can penetrate loosely bound soils, sand or regolith with a range of grain sizes, but not hard intact rock or bedrock. Further, tests show that 10 cm diameter rocks are displaced by the mole, 15 cm diameter rocks will likely be displaced by the mole, and that if flat rocks embedded in the sand are encountered at $<45°$ relative to the descending mole, it deflects around the rock and keeps descending along the gravity vector once it clears the rock. A tether length monitor and accelerometers are used to track the path of the mole, so deflection around rocks is not an issue for reconstructing the mole path.

Early in project development, initial mean free path calculations indicated a high probability of penetrating 3–5 m deep for a regolith volume with <10 % rock abundance. Subsequent effort during project development focused on estimating the rock abundance and size-frequency distribution at the landing site (Sect. 7.5), understanding the shallow subsurface structure from observations of exposed cross sections in scarps (Sect. 7.8), measuring the thickness of the fine-grained regolith from the onset diameter of rocky ejecta craters (Sect. 7.8), and the development of fragmentation theory and modeling based on the cratering record (Sect. 7.10). All of these results indicate a fine-grained regolith 3–17 m thick with low rock abundance that should be conducive to penetration by the mole. Mean free path calculations (Sect. 7.10) for various assumptions of rock abundance and size-frequency distributions, the size of a rock that will stop the mole, and the deflection of the mole around rocks indicate the probability of penetrating 3–5 m deep ranges from 41 % to 98 %.

2.10 Other Considerations

2.10.1 Winds

Landing systems with parachutes cannot tolerate high winds or significant wind shear while on the parachute (e.g., Golombek et al. 1997, 2003a; Crisp et al. 2003). Horizontal winds impart a lateral velocity on the parachute and lander. The horizontal velocity needs to be removed before landing and there is a limit to the velocity that can be eliminated during terminal descent. Wind shear, which is often associated with moderate and high wind velocities, causes the parachute to induce oscillations in the lander as if on a pendulum (Tamppari et al. 2008). The oscillation can cause the lander to be in an undesirable orientation when it starts turning to orient the thrust vector.

SEIS is an extremely sensitive instrument and winds create noise that interfere with detecting seismic signals (Lognonné and Mosser 1993; Lognonné and Johnson 2007; Longonne et al. 2015; Mimoun et al. 2016, this issue; Murdock et al. 2016, this issue). It can detect the local winds that create turbulence and Reynold stresses on the WTS and SEIS. In addition, the wind moves the InSight lander and tether (Murdock et al. 2016, this issue) and creates micro-seismic noise from short period surface waves trapped in low velocity surface

layers (Withers et al. 1996) as well as the effect of the atmospheric movement coupling to the surface over a broader region (Sorrells et al. 1971).

Although no formal wind related engineering requirements were developed during the landing site selection process, the sensitivity of both the landing system and SEIS to the winds influenced the selection. A number of regions on Mars are known to have relatively high winds due to dust storm tracks (Hollingsworth et al. 1996) and from experience in searching for low wind sites in the equatorial region during the MER site selection (Golombek et al. 2003a; Kass et al. 2003). In addition, regions with significant local and regional topography (such as Valles Marineris) are subject to strong katabatic winds (Toigo and Richardson 2003; Rafkin and Michaels 2003). This led to an early triage of possible landing regions based on the expected winds and their location relative to storm tracks (see Sect. 6.1). Finally, surface winds and their effect on SEIS were considered during the downselection process (Sects. 6.4, 6.6 and 6.7), although wind noise was eventually modeled and found to be below system level requirements (Murdock et al. 2016, this issue).

2.10.2 Surface Alteration

The use of retropropulsive thrusters when landing will necessarily result in modification as the plumes interact with the surface. The potential for such surface alteration to impact landing safety or surface operations was identified as a project risk early during GEMS proposal development. The InSight lander is nearly identical to the PHX lander, whose thrusters eroded down through 5–18 cm of soil to a shallow layer of hard subsurface ice, which prevented deeper excavation. The thrusters on PHX and InSight are pulsed leading to explosive erosion via cyclic shock waves that fluidize soils, producing ten times greater erosion than conventional jets (Mehta et al. 2011). Because the subsurface at the InSight landing site is required to be unconsolidated or poorly consolidated soil for the mole, the potential of increased significant surface alteration during touchdown was a concern (and seeking a more cemented surface would be contrary to the requirement for a fragmented regolith for the HP^3 mole).

While the physical mechanisms governing erosion are generally understood for jet impingement on soil, the use of pulse-modulated thrusters introduces complex erosional mechanisms that are more poorly understood and more difficult to model than conventional jets. Under the cost-capped constraints of the InSight mission, it was not practical to develop and validate a rigorous method to accurately model pulse-modulated thruster interactions with the surface. Instead, an approximate method to bound the risk based on conservation principles was developed and used to characterize the potential for site alteration during InSight landing. It was determined that the total amount of momentum imparted to the surface soil from the thrusters was insufficient to generate craters large enough to pose a risk to landing safety. It is expected that craters will form at the jet impingement locations but they will not be large enough, under nominal conditions, to appreciably alter the surface topography at the lander footpad locations. Associated risks to the surface phase of the mission were also deemed to be relatively minor, involving deposition of sand and pebbles in the workspace where the instruments will be deployed and removing fine dust, which will lower the albedo of the surface, creating a change in surface temperature (important for the HP^3).

3 Planetary Protection Requirements

To comply with international agreements (Committee on Space Research, COSPAR, of the International Council of Science), NASA places requirements on spacecraft cleanliness to

prevent forward contamination of Mars. The InSight lander, which carries no life detection instruments and is not bound for a special region, has been designated as a Category IVa, which sets bioburden requirements typically accomplished by cleaning and subsequent verification, but not sterilization. In addition to verifying spacecraft cleanliness, the Category IVa designation places constraints on the landing site. For InSight, the landing site cannot have: water or ice within 5 m of the surface (i.e., it cannot be a special region, e.g., Rummel et al. 2014), subsurface discontinuities, high concentrations of water bearing soils or minerals, or liquid water created by the mole that could mobilize a 50 nm particle (Benardini and Newlin 2013). Compliance with these planetary protection requirements was via documentation, test, analysis, and a formal Planetary Protection Landing Site Review with the NASA Planetary Protection Officer.

4 Data and Models Used to Evaluate Surface Characteristics

4.1 Introduction

The data and models used to evaluate the InSight landing sites are very similar to those used for the MSL landing site selection, which included complete high-resolution image (CTX and HiRISE) coverage targeted by MRO (Golombek et al. 2012a). The ability to target high-resolution images of the landing sites by MRO has set a new standard for characterizing the surface from orbit. Golombek et al. (2012a) includes a detailed description of the various remote sensing data used to characterize the MSL landing sites to which the reader is referred. In this paper, only differences and advances from the MSL site selection effort are described. These differences are in producing slope maps across the ellipse using photoclinometry with a sample of DEMs, creating combined hierarchical HRSC, CTX, HiRISE DEMs, and specifically investigating and mapping the thickness of the fragmented regolith to address the penetrability of the mole (which had not been part of previous landing site selections).

The major difference in InSight ellipse characterization compared to MSL, is the availability of nearly continuous coverage of the MSL site by stereo HiRISE images and DEMs. The MSL landing ellipse was less than 25 km by 20 km because of aeromaneuvering, so that acquiring stereo HiRISE images and making nearly contiguous DEMs with 1 m elevation postings was possible (Golombek et al. 2012a). The InSight landing ellipse is much larger ($\sim$130 km long), making it impractical to collect continuous stereo HiRISE images. Instead, stereo HiRISE images were acquired at regularly spaced intervals (roughly every fifth image) and photoclinometry on HiRISE mono images were tuned to the adjacent DEM, or adjacent image that was tuned to the DEM (e.g., Beyer and Kirk 2012; Beyer, 2016, this issue). Using this method, nearly continuous slope maps across the landing ellipses were produced. Finally, HRSC images were targeted and DEMs were produced combining images acquired during multiple orbits (Gwinner et al. 2009, 2010a).

Although HRSC, CTX and HiRISE DEMs were generated and used in the MSL landing site selection, combined multi-instrument generated DEMs were not merged into a single DEM, partly because CTX DEMs were produced late in the process. In particular, adjacent HiRISE DEMs for MSL often had elevation offsets between them that had to be smoothed out individually to prevent simulation failures (e.g., Golombek et al. 2012a). For InSight, HRSC, CTX and HiRISE DEMs were made concurrently, and merged during leveling to the MOLA base. This reduced the elevation offsets and produced a superior DEM for use for radar interaction simulations.

InSight is the first lander with a mole designed to penetrate 5 m below the surface. Because the success of the heat flow experiment is dependent on the penetration of the probe and this is included as an instrument deployment constraint on landing site selection, investigation of the physical properties of the near surface crust became, for the first time, part of the investigation and landing site selection. The new data set that was specifically interrogated for this purpose during InSight landing site selection was from SHARAD (Seu et al. 2004, 2007), the Shallow Radar instrument on MRO, which is described below.

4.2 Georeferencing Data Sets

The geospatial data used as input for the hazard maps were georeferenced in a "pyramid" of increasing resolution, i.e. decreasing pixel scale and footprint size. Each successive layer of increasing resolution was georeferenced to the underlying layer, similar to the work by Kim and Mueller (2009) and Golombek et al. (2012a). Starting from the base of the pyramid, the data used in order were: MOLA elevation maps, 463 m/pixel; HRSC data, 12.5 m/pixel; CTX 5–6 m/pixel; and HiRISE ~0.25–0.3 m/pixel. The MOLA binned DEM at 463 m/pixel currently serves as the geodetic reference dataset for Mars. It uses a positive east planetocentric coordinate system referenced to the IAU/IAG 2000 frame, compatible with the inertial coordinates used by spacecraft navigation teams. Due to their large difference in resolution, it is not straightforward to co-register the high-resolution Mars imaging datasets to the global MOLA reference system directly. HRSC data products serve as an intermediary geometric reference dataset bridging between MOLA and higher resolution stereo (and mono) datasets from CTX and HiRISE. Because the HRSC orthophoto and DEM layers are well tied to the MOLA, no adjustments were made to their default horizontal or vertical position. For the CTX data, orthophotos created from the corresponding DEMs were georeferenced first, then regular map-projected CTX visible images in order of lowest to highest emission angle. For each image, ~20–50 tiepoints were used to achieve an estimated spatial accuracy of ±10–20 m. For the HiRISE data, orthophotos created from the corresponding DEMs were georeferenced first, then regular map-projected HiRISE visible images. For each image, ~20–30 tiepoints were used to achieve an estimated spatial accuracy of ±10 m to the CTX base. Finally, NOMAP HiRISE products (non-standard stitched, but not map-projected) were tied to the map-projected versions of the same georeferenced HiRISE images. All tiepoints were saved, and the NOMAP tiepoints were reused in subsequent processing steps. The rock and photoclinometry data were derived from NOMAP images, so the same tiepoints could be used to place those data in the correct locations.

4.3 HRSC DEM and Orthoimage Mosaic

A regional DEM at 100 m grid spacing of the InSight landing site area has been produced from stereo HRSC images (Neukum and Jaumann 2004; Jaumann et al. 2007; Gwinner et al. 2016), as well as a seamless mosaic of panchromatic orthoimages at 12.5 m/pixel. These regional base maps are tied to the global MOLA dataset (Smith et al. 2001b) and cover the latitude range 2.5°S to 5.5°N and the longitude range 133.5°E to 141.0°E. Two versions of the DEM have been produced, one representing heights above the Mars spheroid of radius $r = 3396.0$ km and one version with heights above the geoid surface. Orthoimage gray values initially represent calibrated reflectance but a contrast-enhanced mosaic has also been produced, using Lambert normalization and weighted averaging.

As the surface coverage by HRSC initially was incomplete for the InSight area, two targeted campaigns were planned and HRSC observations obtained in 2013. Mars Express

orbit constraints allowed for medium-scale image ground resolution in this period only. The nadir image ground resolution of the stereo image strips finally available for surface reconstruction is higher than 15 m/pixel in most cases (compared to maximum resolution of 10 m/pixel). Photogrammetric processing was based on the methodology applied to the generation of HRSC Level-4 datasets for the planetary data archives, i.e. image preprocessing, stereo matching, and surface reconstruction (Gwinner et al. 2009), photogrammetric adjustment and co-registration to MOLA (Spiegel 2007; Gwinner et al. 2010a), bundle block adjustment (Spiegel 2007; Bostelmann and Heipke 2014), and DEM generation techniques allowing for variations in density and precision of the points derived from multiple orbits (Gwinner et al. 2010b, 2016).

4.4 Combined HRSC, CTX, HiRISE DEMs

One input into EDL and in particular radar tracking simulations is elevation and slope values at 20 m/pixel, and a combined DEM mosaic was generated using images from HRSC, CTX and HiRISE (see Fergason et al. 2016, this issue, for additional detail on methods). There was near complete coverage in CTX across the landing ellipse. However, the EDL simulations required areas outside of the landing ellipse where we did not have CTX or HiRISE DEMs, and therefore it was necessary to include HRSC data. We also included the HiRISE DEMs down-sampled to 20 m/pixel resolution because, generally, more terrain detail is preserved in the down-sampled HiRISE DEM then what was originally sampled with CTX (Golombek et al. 2012a).

The simulations have difficulties if the DEM has data gaps or seams between adjacent DEMs with different elevations. Using the HRSC DEM described in Sect. 4.3, we refitted CTX DEMs to HRSC and then HiRISE to the CTX, so that all DEMs were registered to a consistent, high-resolution base. To produce a seamless mosaic, smoothing across the image boundaries was necessary. CTX to HiRISE elevation data at the seams were often similar and minimal smoothing at these junctions was needed to produce acceptable seams. However, HRSC to CTX image boundaries required significant smoothing, because upscaling to 20 m/pixel involved a scale change by a factor of five compared to the original resolution of the HRSC DEM. The landing ellipse region is generally flat with smooth topography. In these smooth areas, stereo matching results tend to show increased noise in particular when image resolution is lower, as for HRSC. Consequently, the transitions from HRSC to CTX had significant elevation differences ($\sim$40 m is a common difference that compares well to the three sigma range of HRSC three dimension point precision estimated from redundant intersections). These extreme differences cause slopes as high as 15° that would cause the EDL simulations to fail.

To generate the DEM mosaic with smooth image seams, the NASA Ames Stereo Pipeline DEM generation software package (ASP; Broxton and Edwards 2008; Moratto et al. 2010; Beyer et al. 2016) program dem_mosaic was used. In the dem_mosaic program, no filters are used and instead a weighted combination of the input DEMs is implemented. A key component of the dem_mosaic method is that it allows for a Gaussian (rather than linear) blending, which significantly reduced the sharp appearance at the start of the blended region that was observed in other methods tested (Fergason et al. 2016, this issue). The best result was produced by blending over 50 pixels (1 km) and using the default value of 5-sigma for the Gaussian blending. Although the program required a large number of pixels to be affected, this process resulted in an HRSC-CTX-HiRSE merged DEM mosaic in which image seams were minimized, and no slopes above the EDL simulation threshold of 15° were present along the seams. For the HRSC-CTX-HiRISE DEM mosaic, 98.5 % of the

mosaic has slopes less than 15°, 97.1 % of the mosaic has slopes less than 10°, and 90.2 % of the mosaic has slopes less than 5°.

4.5 Radar Data

We assessed near-surface roughness and layering in the InSight region with radar data, which provide unique constraints for landing-site safety considerations and instrument operations (e.g., Golombek et al. 2008a). For a more detailed description of the radar study, see Putzig et al. (2016, this issue).

4.5.1 Arecibo Roughness and Reflectivity

The Arecibo Observatory's S-band radar at 12.6-cm wavelength (Harmon et al. 1999; 2012) provides information on the near-surface radar reflectivity and dielectric and roughness properties for the InSight region. The radar images have a best spatial resolution of ∼3 km, but the echoes are sensitive to small-scale (0.1–1 m) surface roughness and to rocks larger than a few cm within the signal's penetration depth (1–3 m). Arecibo image data provide a strong constraint on surface roughness by comparison with well-calibrated observations of terrestrial-analog surfaces (e.g., Campbell 2001; 2009; 2012). Low-power returns may indicate a fine-grained mantling material, which can be further investigated by other means.

4.5.2 SHARAD Roughness

MRO's SHARAD (Seu et al. 2004, 2007) offers a measure of surface roughness (Root Mean Square or RMS slope) on horizontal scales of 10–100 m and in footprints of ∼0.5–4.0 km, depending on local topographic variability (Campbell et al. 2013). Additionally, a model-based statistical analysis may be applied to SHARAD returns to estimate material properties and roughness in terms of RMS heights (Grima et al. 2014). These techniques complement smaller-scale information from the Arecibo data and MOLA pulse-width measurements (Neumann et al. 2003) as well as larger-scale (0.1–1.0 km) roughness estimates from MOLA (Kreslavsky and Head 2000; Anderson et al. 2003). Past landing sites have been targeted extensively with SHARAD, yielding roughness estimates consistent with landed observations and other data (Putzig et al. 2014).

4.5.3 SHARAD Sounding

With penetration depths for mid-latitude targets extending to several hundred meters, SHARAD is used to map returns from subsurface interfaces, including those in volcanic deposits located a few 100 km east of the InSight landing area (Morgan et al. 2013). Subsurface detections at landing sites with SHARAD data have thus far been confined to the 'Green Valley' of the PHX site, with returns from ∼25 m depth mapped over 2900 km^2 that may represent the base of ground ice (Putzig et al. 2014). Important to these studies is the use of techniques to distinguish subsurface returns from off-nadir surface returns (clutter) and surface sidelobes. Clutter simulations using MOLA or higher-resolution DEMs are typically performed for this purpose.

5 Atmosphere Definition

The atmosphere is a strong constraint on acceptable landing sites on Mars. In particular, there needs to be sufficient atmosphere (integrated density) available to slow the spacecraft both ballistically and on the parachute as well as providing sufficient time for the lander to softly touch down on the surface. The total atmosphere encountered is controlled by the elevation of the landing site and the landing season due to the annual CO_2 pressure cycle, which varies by 25 % (Kieffer et al. 1992). The InSight landing seasons are near the peak of the annual pressure cycle (2016 just before, and 2018 just after). In addition to the total density, the landing system needs to be robust to the expected density structure as well as the winds and wind shear during EDL (see also Sect. 2.10.1). Because the InSight landing system is almost the same as for PHX, the atmospheric constraints are very similar. However, models of the density structure and winds need to account for both the climate and the weather expected at the landing season and location, making the PHX models unusable for InSight (McCleese et al. 2010). The identical landing system does, however, allow the modeling development approach for InSight to be similar to the one for PHX (Tamppari et al. 2008), though modified for the new season and location.

The atmospheric models for EDL were developed by a Council of Atmospheres, a competitively selected, project-chartered group to produce atmospheric data products needed for EDL (see Sect. 6.5). Density models for EDL analysis were developed based on temperature profiles from Thermal Emission Spectrometer (TES, Christensen et al. 2001) and Mars Climate Sounder (MCS, McCleese et al. 2007) with a measure of variability and uncertainty provided by mesoscale models (OSU MMM5, Tyler et al. 2002; SwRI MRAMS, Rafkin et al. 2001; LMD MMM, Spiga and Forget 2009). The mid-afternoon landing, which matches the sun synchronous afternoon orbits of the two remote sounding instruments on MGS and MRO, allows their data to be used directly. Temperature profiles were acquired at the appropriate season and dust scenarios for the mesoscale modeling of four primary atmospheres. The profiles and models were then combined into an Engineering Density Model (e.g., Tamppari et al. 2008; Golombek et al. 2003a, 2003b). The wind field of the mesoscale model output was also analyzed and used to develop engineering wind models in a manner similar to MER (Kass et al. 2003) and PHX (Tamppari et al. 2008).

Both the landing season for the original launch (L_s 231° in 2016) and the landing season for the revised launch (L_s 295° in 2018) are during the dust storm season on Mars (Zurek and Martin 1993). During the dust storm season, local storms are routine, large dust storms are common and there is a chance for the largest of global storms that significantly affect the global temperature structure. Thus the landing season for InSight presented new challenges to EDL. Note that while Spirit landed at the tail of the dust storm season, the available observations underestimated the potential effects (Natarajan et al. 2015; Golombek et al. 2003a, 2005).

Given the landing season, we evaluated possible dust conditions based on available observations and analysis (Cantor 2007; Wang and Richardson 2015; Kass et al. 2016). A number of cases were selected to take into account the expected uncertainty and variability that will be encompassed by each model for EDL. The first was a background case, representing the seasonal atmospheric behavior at times when no large regional or global dust storm was ongoing. The second case was a large regional dust storm case representing the early onset phases of all large dust storms and the peak phase of a regional dust storm. The third case was a global dust storm and represents one as it finishes growing to its peak opacity, while at its peak, and the early stages of its decay. The final case was a decaying dust storm, which represents the extended decaying phase of a global dust storm back to near-seasonal

conditions. It also encompasses the decaying phase of large regional dust storms. The dusty conditions also increase the modeling difficulty due to the increased uncertainty in the behavior of numerical models under high dust conditions.

In addition to the four primary modeling cases, three supporting cases were identified. The first was a local dust storm at or near the landing site. This has a low probability of occurrence, but it is not predictable based on latency of observations just prior to EDL, which is longer than the expected storm duration. As such, the local dust storm model is more designed to assess the robustness of the landing system to such conditions. Two other cases are identified to help bound the overall atmospheric conditions. The first is an extremely (unrealistically) clear condition for the season—a much colder atmosphere than ever observed. The second is an extremely thick global dust storm, equaling or exceeding the largest one ever seen (in 1972 by Mariner 9, Zurek and Martin 1993). This will result in a somewhat warmer atmosphere.

The early selection of a compact landing region helped compensate for the broad possible atmospheric conditions. From an atmospheric perspective, all four downselected ellipses are indistinguishable. Thus a single model based on the conditions over the region is applicable (with the appropriate surface elevation) for any of the ellipses. The specific location chosen is also helpful for minimizing the impact of the atmosphere on the EDL design. It is in a region that avoids common tracks of dust storms (Wang and Richardson 2015), minimizing the chance for a local dust storm. Likewise, the tropics are the least affected region during most regional dust storms (Kass et al. 2016).

The landing season is a large driver for the atmospheric modeling, unlike the surface characteristics. Thus the shift from landing in 2016 at $L_s = 231°$ to landing in 2018 at $L_s = 295°$ essentially requires new atmospheric modeling even though there is no change in landing region. There was one fortunate aspect in the new and old seasons—the expected surface pressure was almost identical. Evaluation of VL lander surface pressure data (Chamberlain et al. 1976) and MSL REMS surface pressure data (Gomez-Elvira et al. 2012) for the two seasons at the landing local time indicated that the pressure at $L_s = 295°$ was ~0.4 % higher. However, due to changes in the temperature structure at the two seasons, the density profile will change noticeably. Atmospheric modeling for the 2018 landing is ongoing.

6 Landing Site Downselection History

6.1 Sites Identified During Discovery Proposal Preparation

Engineering constraints had been identified during the preparation of the Discovery proposal that are almost the same as those described in Sect. 2, except the latitude limits were initially 1°N to 14°S (slightly more restrictive than 5°N to 15°S) and the ellipse was larger (150 km by 30 km). The elevation, latitude and ellipse size requirements severely constrain potential areas to land InSight. Because most of the equatorial region of Mars consists of highlands, very few areas meet the latitude and elevation requirements. Only two areas on Mars are below −2.5 km elevation and within 1°N and 14°S latitude (Fig. 2). Areas inside the Vallis Marineris canyons and outflow troughs meet these constraints, but placing 150 km by 30 km ellipses on smooth, flat surfaces is problematical and rock abundance in global thermal differencing data sets far exceed 10 % (Christensen 1986; Nowicki and Christensen 2007). In addition, experience searching for low-wind MER ellipses in the equatorial latitudes has shown that this area is on storm tracks from weather systems generated at high northern latitudes (Golombek et al. 2003a and Sect. 2.10.1).

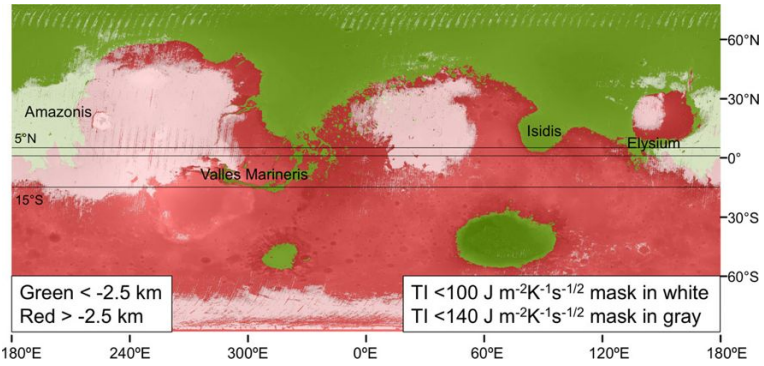

Fig. 2 Global map showing engineering constraints on InSight landing sites. Topography is color coded by elevation with elevations below −2.5 km in *green*. Latitude constraints shown as *horizontal lines*; unlabeled line is 1°N showing initial northernmost latitude during GEMS proposal preparation. Areas low enough and within the latitude bands are labeled in *black*. Very low thermal inertia (*white* and *gray masks*) eliminates eastern Elysium and Amazonis Planitiae. Topography with respect to the MOLA geoid from Smith et al. (2001b); nighttime thermal inertia from TES (Putzig and Mellon (2007a)

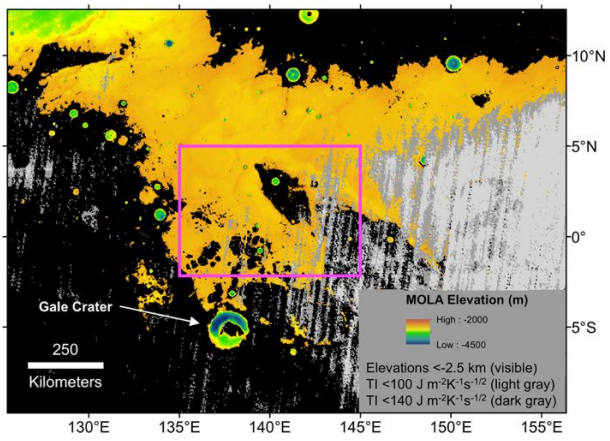

Fig. 3 Western Elysium Planitia showing elevation, thermal inertia and area (*pink box*) between 5°N–2°S and 135°E–145°E in which InSight ellipses were sited (Fig. 4). *Areas in black* are higher than −2.5 km elevation. *Areas in grey* have low thermal inertia. Areas east of 145°E within the latitudes of 5°N–2°S that meet the elevation and thermal inertia constraints are composed of young lava flows without a thick regolith. The Curiosity rover is in Gale crater several hundred kilometers south of the InSight pink box. Topography from MOLA (Smith et al. 2001b); nighttime thermal inertia from TES Putzig and Mellon (2007a)

The second area that meets the elevation and latitude requirements is a region that spans Elysium and Amazonis Planitiae. However, all of Amazonis and the eastern portion of Elysium have very low thermal inertia (<140 J m^{-2} K^{-1} s$^{-1/2}$) indicating potentially thick accumulations (meters) of fine-grained dust that is not load bearing and not suitable for landing a solar powered vehicle (Christensen and Moore 1992; Mellon et al. 2008; Mangold et al. 2009). Western Elysium Planitia, however, has higher thermal inertia and broad smooth and flat surfaces at hundreds of meters scale in THEMIS thermal image mosaics (Fig. 3). Several potential landing ellipses were found in the western Elysium region that are below −2.5 km elevation (and close to potential seismic sources in Elysium, includ-

ing Cerberus Fossae). A reference landing site with coordinates of 0.83°S, 141.48°E was identified in the proposal.

6.2 Sites Identified During Phase A

After GEMS was selected for Phase A study (step 1) in May 2011 preliminary engineering requirements were written as project requirements. The engineering requirements changed somewhat during this process with the latitude range increased to 5°N to 14°S and the ellipse size reduced to 139 km by 27 km to increase the number of potential ellipses. The higher northern latitude limit and the smaller ellipse increased the number of areas and number of ellipses that could be considered. Southernmost Isidis Planitia is accessible as well as additional areas in the Vallis Marineris outflow channels (Fig. 2). The smaller ellipses were still too large to fit in the outflow canyons, rock abundance is too high, and atmospheric winds are an issue. Southern Isidis Planitia is large enough to place several ellipses on relatively smooth and flat surfaces, but rock abundance is generally too high, the thermal inertia is high raising concerns the soils may be cemented and difficult for the mole to penetrate (Murphy et al. 2007), and this area is also expected to be on storm tracks and thus likely windy. Trade studies evaluating higher elevations did not open up much new terrain due to the large elevation difference between the highlands and lowlands and the difficulty finding smooth, flat surfaces large enough to place the ellipses in heavily cratered highland terrain. Going further south than 15°S didn't open up any new areas because of the high elevation. Finally, expanding further north helped, but solar power and thermal management suffered beyond 5°N. To increase the number of ellipses possible in western Elysium Planitia from several to 16, the project agreed to further reduce the ellipse size to 130 km by 27 km, by narrowing the entry flight path angle uncertainty, and to increase the northern latitude limit to 5°N, enabled by improvements in the power system and larger solar arrays. This region has extensive Hesperian plains surfaces that appear relatively smooth and flat with low winds (e.g., Golombek et al. 2003a). Experience suggested that there were enough initial candidate sites (16) in the western Elysium area that an acceptable final site would be found.

Using available remote sensing data, 16 prospective landing sites on Hesperian plains in western Elysium Planitia were identified that appeared to meet the engineering and instrument deployment requirements (Fig. 4; Table 5). Ellipses in smooth, flat regions in THEMIS thermal images (the highest resolution images available at the time) were identified that were below −2.5 km between 2°S–5°N and 135°E–145°E (Golombek et al. 2013a). Ellipses were placed so that Infrared Thermal Mapper (IRTM) and TES rock abundance estimates (Christensen 1986; Nowicki and Christensen 2007) were dominantly below 10 %. To reduce the engineering trade space that would be necessary to model atmospheric and thermal conditions at disparate regions, the project made the decision to eliminate Vallis Marineris and Isidis from further consideration. This dramatically reduced the impact of subsequent landing site decisions on the project, as an atmosphere at only one location needed to be modeled (Sect. 5) and no major engineering trade studies were needed for power or thermal management. By the time of the site review in May 2012 after the Concept Study Report had been submitted, several CTX and HiRISE images of the landing site region had been acquired. They showed one of the terrains was smooth, relatively free of rocks, and likely had a fragmented regolith roughly 5 m thick conducive to full penetration of the mole (Golombek et al. 2013b).

6.3 First Landing Site Workshop

Ten months after InSight was selected as the next Discovery Program mission (August 2012), the First InSight Landing Site Workshop was held in Paris on June 27, 2013. Im-

Table 5 Remote sensing data for 16 InSight landing sites in western Elysium Planitia

Ellipse	Latitude, Longitude	Elevation	TES TI	TES RA	IRTM RA	DCI	Albedo
E1	4.959, 142.359	−2630	237	5 (1–8)	4, 8, 8 (6, 10)	0.94	0.25
E2	3.72, 143.945	−2636	183	5 (2–10)	3, 10 (5, 8)	0.94	0.26
E3	4.262, 142.941	−2608	219	5 (2–10)	8, 6 (4, 6)	0.94	0.25
E4	1.812, 138.89	−2693	278	3 (3–10)	4, 7 (1, 11, 12)	0.95	0.24
E5	3.278, 138.154	−2691	283	5 (1–12)	9, 10 (2)	0.94	0.24
E6	3.231, 135.77	−2640	269	6 (1–8)	6, 10 (9)	0.94	0.24
E7	3.553, 136.758	−2650	272	6 (2–12)	9, 10 (6)	0.94	0.24
E8	4.082, 137.303	−2696	283	6 (3–8)	9, 10	0.94	0.24
E9	4.323, 135.663	−2664	259	4 (1–7)	4, 9	0.94	0.24
E10	4.744, 136.165	−2677	265	4 (2–7)	4, 9 (10)	0.94	0.24
E11	1.477, 138.957	−2699	276	6 (2–10)	4, 7 (1, 11)	0.94	0.25
E12	0.881, 138.408	−2641	247	11 (2–23)	1, 5, 14 (7)	0.95	0.25
E13	0.312, 137.652	−2630	240	6 (1–16)	1, 5, 12	0.93	0.26
E14	−0.833, 141.856	−2687	234	6 (3–11)	2, 9 (6, 11)	0.94	0.25
E15	−1.281, 141.85	−2700	232	6 (2–12)	8, 9 (6, 7)	0.94	0.25
E16	−1.864, 136.962	−2561	248	12 (1–19)	11, 11 (3, 8, 10)	0.94	0.26

Latitude and longitude in °, positive north and east, planetocentric; elevation in m with respect to MOLA geoid from Smith et al. (2001b); TES thermal inertia (TI) in J m^{-2} K^{-1} $s^{-1/2}$ from Mellon et al. (2000); TES and IRTM rock abundance (RA) in % from Christensen (1986) and Nowicki and Christensen (2007), with values in parentheses partially in ellipse; Dust cover index from Ruff and Christensen (2002); albedo from Christensen et al. (2001)

mediately after selection, a large number of landing site activities were initiated. The first and most important was to begin high-resolution imaging of the InSight ellipses with CTX and HiRISE on MRO. However, because the western Elysium region is directly north of Gale crater, 150–675 km from where Curiosity was operating, there was a conflict between relaying information from Curiosity and imaging so close in time on the same orbital pass. The difficulties of rolling the MRO spacecraft off nadir for targeting images of landing sites immediately after communicating with Curiosity required detailed study by the MRO project and the impact to MSL had to be evaluated. It took about 6 months to work through these issues, which resulted in a set of guidelines that allowed targeting images immediately after communicating with Curiosity on the same pass. A Memorandum of Agreement between the JPL Mars Exploration Program and the InSight project describing the support for landing site imaging, atmosphere characterization and communications during EDL and surface operations was completed in the spring of 2013. Since then, targeted HiRISE images of InSight landing sites have been acquired at a rate of one per week until landing site selection in December 2015. By the First Landing Site Workshop, about 90 % of the western Elysium area with ellipses was covered with CTX images and about 13 selected HiRISE images had been acquired. The early acquisition of CTX images at 6 m/pixel covering so much area had an enormous impact on site selection. CTX images were high enough resolution to allow the identification of terrains with different surface characteristics and to map them across the ellipses (Fig. 5). Early HiRISE images were targeted to test the identification of these terrains in CTX images and to determine their relative roughness and rockiness. It was discovered that terrains could be confidently identified in CTX images, which coupled with

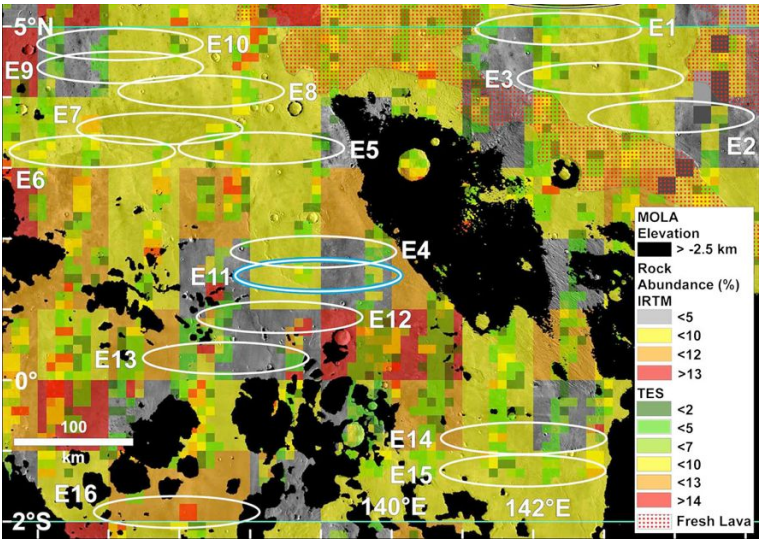

Fig. 4 Sixteen ellipses in western Elysium Planitia that meet engineering constraints sited during phase A. *Areas in black* are higher than −2.5 km elevation. *Colors* are rock abundance from thermal differencing. Ellipses (130 km by 26 km) are sited on Hesperian smooth, flat plains materials just north of the dichotomy boundary. Noachian highlands are to the south and west, a ridge of Medusae Fossae Formation is to the southeast (*mostly black*), and very young lavas (*stippled red*) from Athabasca Valles are to the east (Tanaka et al. 2014). The ellipse E11 (*blue outline*) was selected as a reference ellipse for engineering studies. Ellipse E9 was eventually selected for landing InSight. Remote sensing data for the ellipses are in Table 5. Topography from MOLA (Smith et al. 2001b); rock abundance from Infrared Thermal Mapper (IRTM) with 1 pixel per degree (Christensen 1986), and from Thermal Emission Spectrometer (TES) with 8 pixels per degree (Nowicki and Christensen 2007)

the targeted HiRISE, allowed the rapid identification of the smoothest and most rock-free terrain and the initial measurement of slopes and rocks in them.

All available data of the landing sites were discussed at the workshop. Presentations included mapping of terrains in CTX images, analysis of slopes and roughness in MOLA data, preliminary work on DEMs from HRSC and HiRISE stereo images, rock counts from shadows in HiRISE images, rock size and regolith thickness from fragmentation theory, thermal imaging and rock abundance, secondary craters, and a general discussion about the downselection. Six additional potential landing site ellipses were defined using the CTX images and terrain maps (Fig. 5).

6.4 First Landing Site Downselection

By the time of the first downselection (July 2013), mapping of terrains in CTX images along with 20 HiRISE images allowed the definition of a number of terrains (Fig. 5) based on morphology, thermal signature and likely slope and rock hazards (Wigton et al. 2014). The five main terrains are smooth, rougher smooth, gradational and patchy etched, and etched (Sect. 7.2). Slope hazards (crater rim and highland scarp) and dense crater rays/swarms were also defined. Initial characterization of slopes at the 2–5 m length scale in two HiRISE stereo DEMs provided by Antoine Lucas and measurement of rocks from their shadows (e.g., Golombek et al. 2008b, 2012b), indicated that the smooth terrain was exceptionally safe with low slopes and very low rock abundance (0–3 %). Etched terrain appeared the least safe

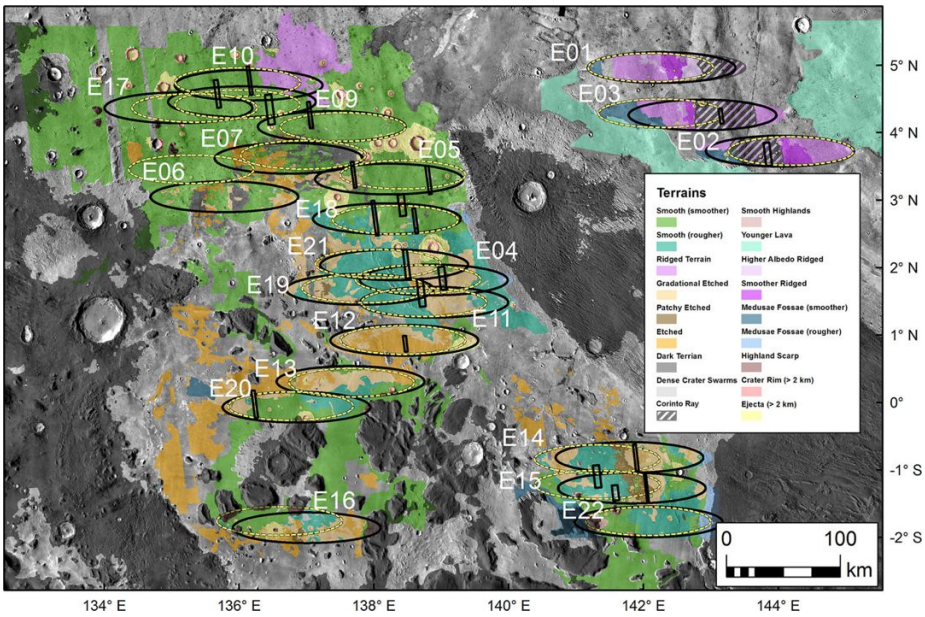

Fig. 5 Terrain map of InSight landing region in western Elysium Planitia with outline of HiRISE images (20) at the first downselection. Images were targeted to sample different terrains in different ellipses mapped in CTX. Note mapping was completed in areas in which ellipses could be placed relatively safely, and is thus incomplete in areas in which ellipses could not be safely placed. Terrains in the northwest are defined in Sect. 7.2. *Black ellipses* are 130 km by 27 km; *yellow dashed ellipses* are 110 km by 25 km, both oriented east-west. *Dark gray areas* are higher than −2.5 km elevation. Hatched area in ellipses E1, E2, and E3 is a dense Corinto secondary ray. Background mosaic is from the THEMIS daytime thermal global mosaic. The safest terrain is the smooth terrain (*green*), which led to the downselection to four ellipses (E5, E8, E9, and E17) that are dominantly in this terrain. Note ridged terrain (*pink*) is younger, Amazonian lava (with primary flow features) that was judged to have a less well developed regolith and less conducive to full mole penetration, which led to the elimination of ellipse E10. Note the orientation of the HiRISE images is the ground track of the MRO orbiter, which when extended south from the western ellipses directly crosses Gale crater where MRO must downlink data from the Curiosity rover

with higher slopes and rock abundance (∼20 %) with the other terrains in between. Analysis of along-track MOLA data (Fig. 6) show that large crater interior walls and highland scarps exceeded the 15° slope constraint at ∼300 m length scale (Golombek et al. 2014a).

Two other hazards in the ellipses were recognized: rocky ejecta craters and fresh secondary craters. THEMIS thermal images showed craters between ∼40–2,000 m diameter have high thermal inertia ejecta blankets (Fig. 7). CTX images show many of these ejecta blankets are light-toned. HiRISE images show the ejecta has large rocks and bright eolian bedforms. The limited diameter range for these craters indicates a strong coherent layer of rock at ∼4–200 m depth and fragmented regolith above (Golombek et al. 2013b; Warner et al. 2014, 2016, this issue), conducive to penetration by the heat flow probe, and weaker sediments below. Rock counts were used to estimate the rock abundance in these ejecta blankets, CTX images were used to measure the area covered by the ejecta blankets, and thermal images were used to extrapolate across an entire ellipse.

HiRISE images also showed virtually all of the ellipses had a population of small secondary craters (Golombek et al. 2014b). Dense secondary swarms covered 20–45 % of the surface of three ellipses (E1, E2, and E3). Tracing the azimuth of these dense secondary rays showed they originated from a fresh, impact crater called Corinto (16.95°N, 141.7°E)

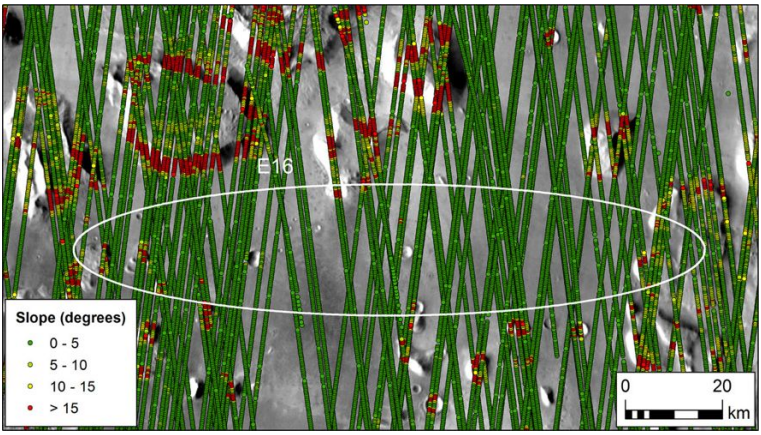

Fig. 6 Bidirectional slope data derived from MOLA shot points spaced at ∼300 m apart over Ellipse E16. Slopes that exceed the 15° landing requirement are highlighted in *red*. Several of the southern ellipses, including E16, contain remnant knobs of highland terrain that pose a hazard for landing. These slopes are shown as the highland scarp terrain unit in Fig. 5

about 800 km to the north (Golombek et al. 2014b). Dense crater rays show up as dark elongate forms in nighttime THEMIS images, similar to other fresh-rayed craters, and radiate ∼1400 km to the south. Targeted HiRISE images in the InSight ellipses indicate all dark rays (in nighttime THEMIS) ellipses are composed of dense secondary craters. The density and SFD of secondaries in these dense rays were measured (Bloom et al. 2014) and their geometry assumed from morphometric measurements of other secondary craters (Pike and Wilhelms 1978) that indicate the depth and width of each steep interior wall is ∼10 % and ∼25 % of their diameter, respectively.

The relative safety of all 22 candidate ellipses was estimated by measuring the areal extent of different terrains in the ellipses, by ascribing failure probabilities due to slope and rock hazards, and then summing the proportion of terrains and their risk for each ellipse (Golombek et al. 2014a). The main contributors to failure in this analysis are 300 m slope hazards and rock hazards. Slopes >15° were considered as 100 % failure because the seismometer cannot level itself on steeper slopes. Slopes that exceeded 15° at 300 m length scale were assumed to be at least that steep at 2 m length scale.

Measurement of rock SFD in HiRISE images, their validation by comparing with landed rock measurements, and their probabilities of failure were documented for the PHX landing in the northern plains (Golombek et al. 2008b). We used the same technique for measuring the rock diameter and height by automated segmentation of shadows and all rocks larger than 1.5 m diameter were counted in 150 m square bins for several HiRISE images with different terrains. We then used the relationship between number of rocks in each bin and the derived cumulative fractional area covered by rocks (or rock abundance which varied from 0–20 % for the different terrains) to calculate the risk to landing on a rock higher than the base of the lander or that would impede the opening of the solar panels (Golombek et al. 2008b, 2012b). We took average rock density for each terrain and ascribed respective failure rates for each rock abundance based on PHX and then summed the risk based on the fractional coverage of each terrain. The risk of landing on rocky ejecta was estimated in a similar way based on rock counts, measurement of ejecta blankets in CTX images, and estimates of the total area covered by ejecta from thermal images.

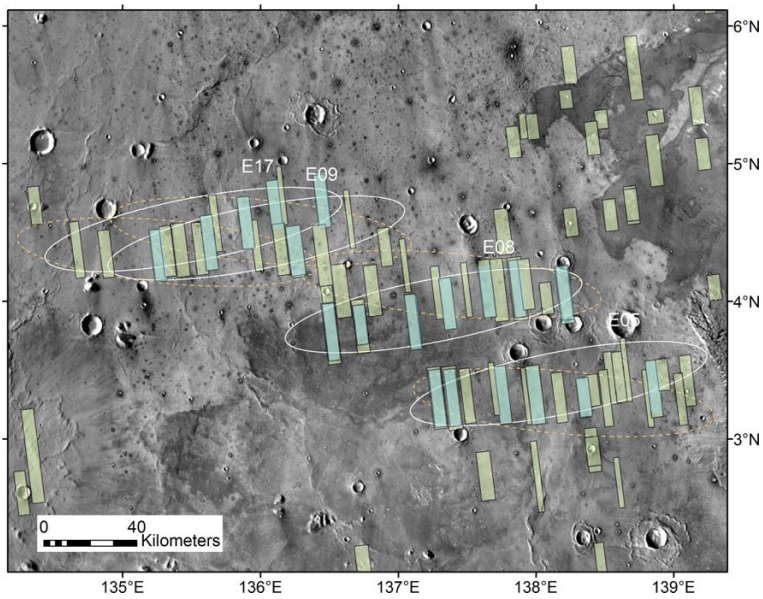

Fig. 7 Mosaic showing HiRISE image coverage of the final four InSight landing sites at the time of the Second Landing Site Downselection. Stereo image pairs are shown in *blue*. Ellipses are 130 km by 27 km for the open (*white*) and close (*orange dashed*) ellipses in the 2016 launch period. Background image mosaic is from the daytime THEMIS global mosaic at 100 m/pixel. Note thermally dark young lavas from Cerberus to the northeast, the Medusae Fossae formation just to the southeast, and the relatively smooth Hesperian plains with monadnocks of highlands. Note generally north trending wrinkle ridges that deform the plains (suggesting subsurface basalt flows) and the large rampart ejecta craters. Craters larger than around 40 m but smaller than around 2 km are *dark* (indicating colder daytime temperatures and higher thermal inertia) rocky ejecta craters. These craters are excavating strong coherent rock (likely basalt) from depths of 4–200 m depth, with a fractured regolith on top and weaker sediments beneath. Note fairly uniform light tone of the smooth plains and the darker tone of the etched and gradational etched terrain covering western portions of ellipses E8 and E5, likely due to the greater rock abundance in these terrains. Compare these thermal signatures with terrains mapped in Figs. 5 and 8

The area of dark Corinto rays was measured in THEMIS images and sample density measurements in HiRISE images along with the assumed geometry were used to estimate the probability the lander would be on a slope greater than 15° or that the solar panels would be blocked from opening fully.

The cumulative risk from all sources determined using this method varied from 1 % to 7.5 % for the 22 ellipses (130 km by 27 km). Not surprisingly, ellipses that were mostly in smooth terrain without highland scarps, large fresh crater walls or dense secondary crater rays were the safest (Golombek et al. 2014a). These ellipses are all located between 3°N–5°N and were estimated to have ∼1–2 % probabilities of failure. Although extrapolation of winds to the surface from a Mars mesoscale wind model suggested that other ellipses might have lower surface winds (thereby reducing SEIS noise), these ellipses were substantially less safe and there were questions about the veracity of the model results.

The First Landing Site Downselection meeting was held on July 29, 2013 at JPL and included participation by science team members, the engineering team, project management, and members of the standing review board. Engineering analysis of power and thermal management showed ellipses between 3°N to 5°N were preferred. The project downselected to the four safest ellipses (E5, E8, E9, E17) in the preferred latitude range for further imaging and analysis (Figs. 7 and 8; Table 6).

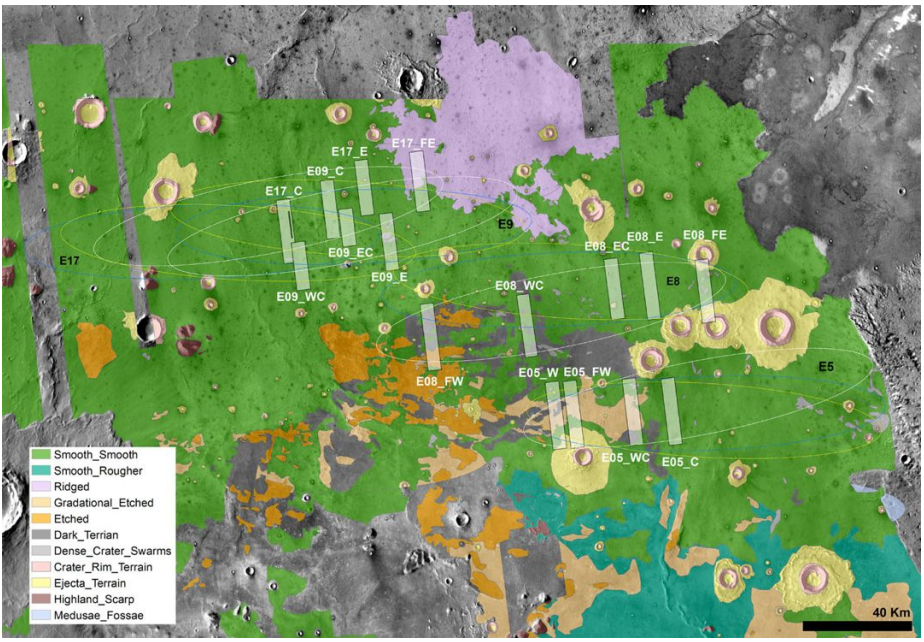

Fig. 8 Terrain map of the final four Insight landing site ellipses, and the HiRISE DEMs used to characterize them. Note that the DEMs sample all of the terrains that the ellipses cover and that mapping of the terrains has been completed within and around the ellipses. Ellipses are 130 km by 27 km for the open (*white*), middle (*blue*) and close (*yellow*) of the 2016 launch period. Daytime THEMIS mosaic is in the background. The ten DEMs used at second landing site downselection (Sect. 6.6) are E17_E, E17_FE, E09_E, E08_FW, E08_WC, E08_EC, E05_FW, E05_W, E05_WC, and E05_C

Table 6 Final four ellipse center (130 km by 27 km, 90° azimuth) coordinates

Ellipse	Lat., °N	Long., °E
E05	3.31	138.23
E08	4.09	137.37
E09	4.46	136.04
E17	4.37	135.10

6.5 Second Landing Site Workshop

In February 2014, the InSight project established two groups, the Council of Atmospheres and the Council of Terrains, to produce data products needed for atmospheric and surface characterization for EDL. In 2013, the InSight project sponsored a Request for Proposals (similar to the Critical Data Products program sponsored by the Mars Exploration Program) to develop HRSC, CTX and HiRISE DEMs of the landing sites. Slope maps from HiRISE photoclinometry that were tuned to the DEMs were also requested. Maps of rocks and rock SFD were solicited, as were maps or estimates of radar reflectivity and the physical properties and structure of the upper 5–10 m of the crust to assess the mole penetrability. Atmospheric data products that were used for EDL simulations included density, temperature profiles, surface pressure, winds and dust events (Sect. 5). Investigators were selected to ad-

dress all of these topics and they were organized into the two councils along with interested members of the InSight science and engineering teams (Table 2).

By the time of the Second Landing Site Workshop, held September 23, 2014 at JPL, roughly 50 HiRISE images of the final four landing sites had been acquired and 10 HiRISE DEMs had been produced (Howington-Kraus et al. 2015). A preliminary HRSC DEM across the entire area had been produced and CTX DEMs were under construction. HiRISE photoclinometry slope maps had been produced for about 30 images (Beyer, 2016, this issue). Terrain maps from CTX images were further validated using new HiRISE images. Automated rock counts and SFD were extracted for rocks 1.5–2.25 m diameter and fit to exponential model distributions and results were validated in pilot studies with human observers. Rocky ejecta craters were mapped and a gradational sequence of fresh to degraded craters was identified and initial estimates of the regolith thickness were obtained from their onset diameter (Warner et al. 2014). Fragmentation theory was applied to the Hesperian cratered surface at the InSight landing region and rock distributions and regolith thickness estimates were in general agreement with observations (e.g., Sect. 7.10). Arecibo radar backscatter maps of western Elysium Planitia were evaluated along with SHARAD roughness at 10–100 m length scale and subsurface returns. MOLA slope and roughness were derived and compared favorably to the SHARAD roughness. Secondaries from Corinto crater were mapped across the ellipses and their SFD measured (Bloom et al. 2014). THEMIS thermal inertia data was used to characterize the physical properties of surface materials and the rocks around craters. Finally, the creation of hazard maps for use in landing simulations from the DEMs and rock counts was reviewed.

The Second Landing Site Workshop also included a peer review of the surface data products produced and their use in assessing the safety of InSight landing sites. This is a step carried out in all landing site selection activities and serves as a validation of the derived data products to address their production, their use for landing simulations, and any omissions. A formal review board evaluated the data products, as did a subset of the standing review board. The review board was unanimous that the suite of data products being produced was sufficient for evaluating the landing sites and that each product was being produced, validated and leveraged appropriately towards this end. They did not identify anything missing and found that the selection activity was on schedule.

6.6 Second Landing Site Downselection

The Second InSight Landing Site Downselection meeting was held January 16, 2015 at JPL, and was attended by the Council of Terrains, project management and a subset of the standing review board. The objective was to downselect to a smaller number of ellipses ($\sim$2) to concentrate analysis and fill in the selected ellipse with HiRISE images. At the time of the meeting, about 75 HiRISE images had been acquired of the final four landing sites (Fig. 7). Ten of the stereo pairs that sampled all of the terrains that the ellipses covered had been processed into DEMs (Fig. 8). Characteristics of the terrains were summarized and their rock abundance, slopes, and thermal inertia were compared to the engineering requirements as were the ellipse sizes, latitude and elevation. Average terrain slopes and rocks from the ten DEM samples were extended throughout the ellipses, and hazard maps were made based on the modeled failure of the spacecraft on touchdown. Finally, the landing points in the ellipse were convolved with the hazard map to determine the probability of success when landing at an ellipse center point that was varied systematically across the map. This yielded contour maps of the probability of success and the demarcation of the safest ellipses.

Comparison of the landing site surfaces with engineering requirements showed that the smooth terrain was the most benign. Rock abundance in the smooth terrain averaged $\sim$2.5 %

(below the 10 % requirement) and increased in other terrains to about 35 % in the crater rim ejecta. At length scales of around 100 m, extrapolated RMS slopes, relief, and pulse spread in MOLA data, as well as SHARAD roughness and HiRISE RMS data all indicate very smooth and flat surfaces that would not violate the 15° engineering constraint. Slope statistics at 1–5 m length scale from HiRISE DEMs and photoclinometry show that the smooth terrain has less than 0.5 % area that exceeds the 15° engineering constraint, and that InSight ellipse surfaces are smoother at this scale than all other landing sites with the possible exception of Opportunity and PHX. Sampling of Corinto secondaries in DEMs and photoclinometry slope maps show much shallower depth/diameter ratios (~0.04–0.06) than expected (0.1) and interior shapes with slopes that do not approach the 15° limit, indicating that they are not a hazard, even though the density of secondaries appeared higher in E9 than in the other ellipses. Analysis of TES and THEMIS thermal inertia data shows an average thermal inertia of around 200 $J\,m^{-2}\,K^{-1}\,s^{-1/2}$ that is consistent with surface grain sizes of fine sand with very weak cohesion, no dust layers >1–2 mm thick, no outcrop, and from seasonal variations, the same properties to a depth of 0.5–1 m beneath the surface. Arecibo backscatter maps show a radar reflective surface that together with the thermal inertia, indicate a load-bearing surface without thick deposits of fine-grained dust. Analysis of the onset diameter of rocky ejecta craters indicated that the majority of the plains surface was underlain by fragmented regolith at least 5 m thick and therefore conducive to HP^3 mole penetration (Pivarunas et al. 2015), a conclusion also supported by fragmentation theory for the Hesperian cratered plains. The lowest rock abundance and smoothest smooth terrain were found in ellipse E9.

The landing safety analysis involved touchdown failure analysis via slope and rock abundance sensitivity studies, the generation of hazard maps from the data products, and estimation of the probability of failure on the different terrains. Monte Carlo touchdown simulations on rock-free planar surfaces show no failures on slopes below 15°, with failures increasing with higher slopes and 100 % failure assumed for >20°. Analysis on rock fields that follow exponential SFD show failures slowly increase to about 2 % at 10 % rock abundance, increasing along a quadratic to around 25 % at 40 % rock abundance, and 100 % failures assumed at higher rock abundances. Failure rates for combined slope and rock statistics for each terrain unit rise from around 1.6 % for the smooth terrain to around 2.5 % for gradational etched and etched terrains. Ascribing the failure probability of each terrain in the map yields a hazard map. Running the ballistic landing points for a landing ellipse of a given size and orientation yields the probability of success for any ellipse center location in the map, which is then contoured. Results for the opening of the launch period show all four ellipses have a ≥97.5 % probability of success, and E9 having a >98.3 % probability of success. Results are similar for the middle and close of the launch period and for ellipse sizes of 130 km by 27 km and 110 km by 25 km. A broad region around the E9 ellipse center exceeds 98 % success probability for all ellipse sizes and azimuths possible for the entire launch period.

Two other factors affected the downselection. First, a more refined solar energy and spacecraft power analysis showed that sites close to 5°N had more energy, enabling longer continuous operations and greater science data return than sites at 3°N. Second, extrapolation of winds to the surface from a Mars mesoscale wind model suggested that ellipses E5 and E8 have the lowest winds, which would reduce SEIS noise. The project provisionally selected the E9 ellipse for InSight at the Second Downselection meeting. The site selection team concentrated all analysis efforts on ellipse E9 to fill in most of the ellipse with HiRISE images and to confirm that secondaries are not hazardous. Because of the close proximity of ellipses E9 and E17 and their substantial overlap at the open, middle and close orientations (Fig. 7), they were merged and the E17 ellipse name was dropped. The Council of Atmosphere evaluated surface winds at the remaining ellipses.

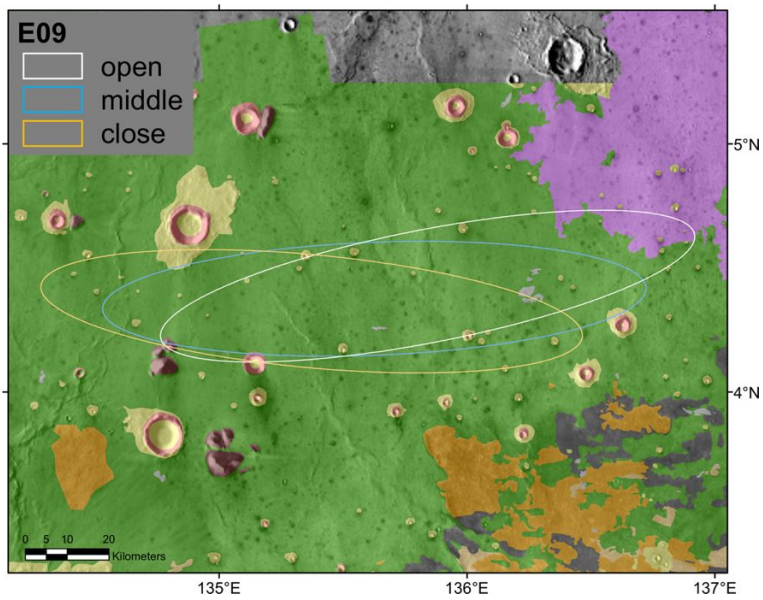

Fig. 9 E9 ellipses for the open (*white*), middle (*blue*) and close (*orange*) of the 2016 launch period on the terrain map at the time of selection and elimination of ellipses E5 and E8 (May 2015). Ellipses are 130 km by 27 km and are placed to avoid large craters and to maintain the smooth terrain in the central half of the ellipse where the probability of landing safely is greatest. Terrains are defined in Fig. 8. Background is the THEMIS thermal daytime image mosaic

6.7 Ellipse E9 Selected

On May 6, 2015 the InSight project selected the landing ellipse E9 (Fig. 9) to work towards certification in the Fall of 2015. The landing site team presented updated results on rock abundance, slopes and secondaries in ellipse E9 and comparisons to the other ellipses at the Project System Engineering Team meeting. By the time of the meeting, over 65 % of the nominal ellipses for open and middle of the launch period had been imaged by HiRISE. Rock maps of E9 had increased from 5 to 14 and results showed no change in the average of 1.5 % rock abundance, which is about half of that in E5 or E8. Three new HiRISE DEMs (Fig. 10) showed no significant difference in the RMS 1 m slope for E9 ($\sim$3.9°), which is smoother than the other ellipses and has the least area (0.3 %) that exceeds 15°; tuned photoclinometry slopes from 21 HiRISE images yield similar results. Analysis of secondaries showed that although their density is higher in E9 than E5 or E8, the difference in area covered is only 0.1–0.3 % and totals only 1.5 % in E9. Analysis of their depth/diameter at 1 m elevation postings in the DEMs and at 25 cm scale in the photoclinometry confirmed very shallow floors ($\sim$0.05) with maximum slopes well below 15° (Daubar et al. 2016). Slope distributions of the secondaries show 0–0.4 % area with slopes $>$15° and confirm that they do not contribute significantly to the average slope distributions of the ellipses. The Council of Atmospheres evaluated near-surface wind speeds (related to SEIS noise) for the three different ellipses and their uncertainty with three mesoscale models. Model results indicated low wind speeds, but none of them agree with each other (suggesting they are all wrong). The Council of Atmospheres concluded that it was not possible to distinguish expected surface winds between the ellipses and thus should not be considered a discriminating factor

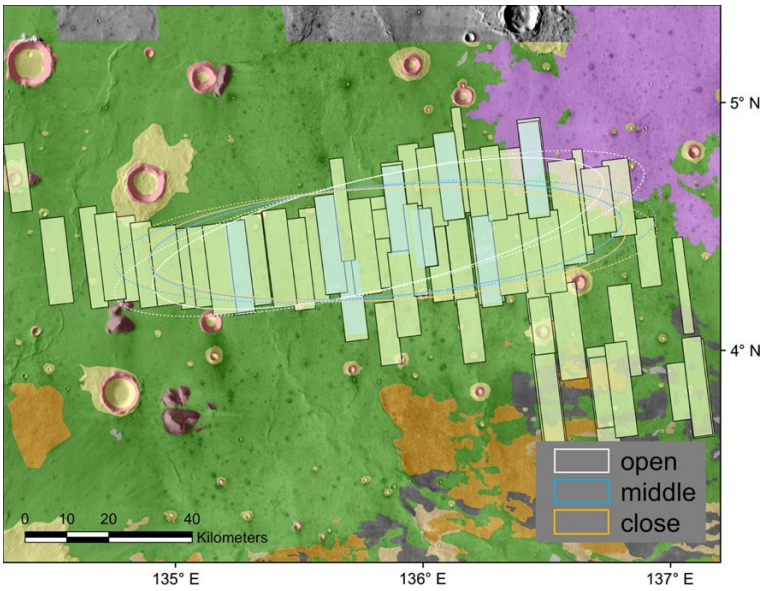

Fig. 10 HiRISE image coverage in early 2016 on the terrain map of ellipse E9 for the 2018 launch opportunity. HiRISE mono images shown in *green*; those in *blue* are stereo. *Dashed ellipses* are 130 km by 27 km and *solid ellipses* are 100 km by 27 km for the open (*white*), middle (*blue*) and close (*orange*) of the launch period. Existing HiRISE images cover >90 % of the open, middle and close of the launch period ellipses. Simulations show these ellipses have a 99 % probability of success for landing. Background is the terrain map (defined in Fig. 8) over the THEMIS thermal daytime mosaic

in site selection. Ellipses E5 and E8 were thus eliminated from consideration and all work concentrated on ellipse E9.

6.8 Third Landing Site Workshop

The Third InSight Landing Site Workshop was held September 30, 2015 at JPL and included a thorough review of all information about the landing site, a careful assessment of all data products produced and their conversion into hazard maps, and an evaluation of simulation results (Golombek et al. 2016). By the time of the workshop, five CTX and six HiRISE DEMs (Fig. 10) had been completed and a merged HRSC, CTX, HiRISE topographic map of E9 had been completed for radar interaction studies. Over 30 rock and photoclinometry derived slope maps covering the ellipse were also completed. These data products were georeferenced onto hierarchically controlled basemaps and then converted into separate hazard maps. These maps were convolved with the landing points within the ellipse to determine the probability of success for an ellipse at any center location in the map. Results continued to show a broad region with greater than 98 % success for a variety of ellipse sizes and orientations centered around E9.

Continued study of thermal inertia refined the fine component as fine-sand and observations of seasonal variations showed no indication of stronger materials in the subsurface and, thus that the same sandy soils existed throughout the upper 0.5–1 m. Most SHARAD observations found no subsurface reflectors or water or ice, except for an isolated return south of ellipse E9 that could be related to ejecta, basement, or basalt interfaces (Putzig et al. 2016, this issue). Study of rocky ejecta craters separated the effects of their degradation

due to eolian activity and subsequent cratering (Sweeney et al. 2016) from the influence of the thickness of the regolith overlying the stronger rocks. Results indicated that the regolith varied from 3 m to 6 m thickness across the area, but that it might be slightly thinner near the center of ellipse E9 (Warner et al. 2016, 2016, this issue).

6.9 Independent Landing Site Selection Review and InSight Project Certification

The Independent Landing Site Selection Review, chartered by NASA, and the InSight Project Landing Site Certification were jointly held October 14, 2015 at JPL. The peer review board consisted of three engineers and two scientists and included a thorough review of the processes that the project used to determine its recommended landing site as well as the most important analyses that support that recommendation. The review board members unanimously agreed that there were no significant oversights or shortcomings in the InSight landing site selection effort, and agreed with the selected landing site. The board noted that the location of the landing site would produce relay conflicts with the Curiosity rover, but that was unavoidable. It also noted that regolith thickness maps could be used for final landing site targeting. Following the review, the InSight Project certified the E9 ellipse as the landing site.

6.10 Planetary Protection Landing Site Review and NASA Headquarters Briefing

The Planetary Protection Landing Site Review was held on October 19, 2015 to demonstrate that the landing site was compliant with planetary protection requirements (Sect. 3). These requirements included no water or ice within 5 m of the surface, no subsurface discontinuities, no high concentrations of water bearing materials, and that operation of the mole would not generate enough water or brine that could mobilize a 50 nm particle. One presentation addressed the first three requirements, which are discussed below, and another addressed the last requirement.

The geologic setting of the InSight landing site region suggests a fragmented regolith overlying basalt flows (see Sect. 7.1). Analysis of terrains in the region indicate that the dominant processes shaping the region are impact and eolian (Sect. 7.2). A recent review of special regions on Mars does not include western Elysium as one (Rummel et al. 2014), because near-surface liquid or frozen water is not expected to be stable in the equatorial regions of Mars. There is no evidence for recurring slope lineae, gullies, polygonal terrain, ground ice, glaciers, ice rich mantles, lobate debris aprons, or pasted-on terrain (Rummel et al. 2014; Squyres et al. 1992). An inspection of high-resolution images of steep slopes in the region only shows evidence for eolian modification of the surface, with no evidence for water or ice related features. Rampart and/or fluidized ejecta craters larger than 10 km diameter are found in the region (similar to most of the equatorial regions of Mars), but none are close to the landing ellipse (all $>$50 km away) and any water or ice that would have been excavated came from much deeper than 1 km. Although impacts that formed in the past 10–20 years from before and after images (Daubar et al. 2013) have unearthed shallow ice in the high northern latitudes (Byrne et al. 2009), none of the four new impacts in the InSight landing site area show any evidence for ice in HiRISE images. Inspection of Corinto secondaries and ejecta, which formed 0.1–2.8 $\pm$ 0.5 Ma (Golombek et al. 2014b), show no evidence of ice or water related activity. Recent reviews of clays and hydrated minerals on Mars show no detections in the plains of western Elysium (Ehlmann et al. 2011; Ehlmann and Edwards 2014). Neutron spectrometer and Gamma Ray Spectrometer data show western Elysium Planitia to have low water equivalent hydrogen (4–5 %), consistent

with minor amounts of bound water or OH in the martian soil (Feldman et al. 2004a, 2004b; Mitrofanov et al. 2004; Boynton et al. 2008). Mapping of strandlines (Parker et al. 1993; Clifford and Parker 2001) and unconfined deltas (Di Achille and Hynek 2010) of a putative global northern ocean indicates the InSight landing site would have been underwater in the Noachian, but any water-rich deposits would be buried beneath 200 m of basalt. Younger strandlines and putative ocean deposits (e.g., Mouginot et al. 2012) were confined to lower elevations, far from the dichotomy boundary and the InSight landing site region. No catastrophic outflow channels or deposits have been identified in this area. Roughly 44 SHARAD observations in the InSight landing site area have been analyzed and no evidence for subsurface water or ice from dielectric properties or subsurface reflectors has been found. Finally, analysis of the rate of degradation of rocky ejecta craters indicate erosion rates (Sweeney et al. 2016) consistent with slow eolian erosion rates at other landing sites and far too slow for erosion associated with liquid water (Golombek et al. 2014c).

The NASA Planetary Protection Officer concluded that the landing site was compliant and met all of the planetary protection requirements. NASA Headquarter officials were briefed on the selected landing site on December 14, 2015.

6.11 Launch Delayed to 2018

The 2016 InSight launch was suspended in late December 2015 due to a leak in the SEIS vacuum sphere that would have significantly degraded its performance. Because the SEIS is the core instrument on the lander, it was decided that InSight could not launch without it. In January 2016, the project began exploring subsequent launch options. Optimal (minimum energy) launch opportunities from Earth to Mars occur once every 26 months, just before opposition, when the distance between the two planets is near a minimum. However, because the atmospheric pressure on Mars varies seasonally by 25 % due to the tilt of the spin axis and the ellipticity of the orbit (Kieffer et al. 1992), the elevation at which a spacecraft can land is determined (all other factors being equal) by the season and density of the atmosphere at arrival, which varies considerably between opportunities. For the 2016 launch period and a Type 1 trajectory ($<180°$ around the sun), InSight would have arrived at Mars at $L_s = 231°$, which is in southern spring just before the atmospheric pressure maximum near solstice ($L_s = 270°$). For 2018, the Type 1 trajectory that provides direct to Earth and MRO communications during EDL, launches in May 2018 and arrives at Mars in late November 2018 during southern summer at $L_s = 295°$, just after the pressure maximum. Fortunately, the atmospheric pressure on Mars is almost identical for these two arrivals (Sect. 5). As a result, the landing site elevation requirement is unchanged (<-2.5 km), which is incredibly fortuitous given that there are no lower elevation options that meet the ellipse size and latitude constraints (see Sect. 6.2).

The other two factors (besides elevation) that drove the landing site selection to western Elysium Planitia are latitude and ellipse size (Sect. 6.1). The latitude is determined by solar insolation and thermal management of the lander over a full Mars year. As a result, regardless of when landing occurs, the latitude constraint is unchanged. The ellipse size is controlled by the entry velocity, which is slower for 2018, which results in a slightly smaller ellipse for the same entry flight path angle. However to gain timeline margin during EDL, the entry flight path angle was shallowed slightly so the ellipse size is almost the same size as the 2016 ellipses (and is within the 130 km by 27 km requirement). The azimuth of the ellipse is controlled by the geometry of the transfer trajectory and the landing latitude (which is unchanged). The azimuthal variation in the ellipse is 11.5° during the 2018 opportunity, which is slightly less than for 2016 and is centered at a better azimuth (~93° clockwise

from north) with respect to fitting the ellipse within the large craters around the edge of the preferred landing site area (Fig. 10). As a result, the selected landing ellipse E9 can be accessed in 2018 as well as or better than in 2016 (>99 % probability of success). This enormously simplified project activities for 2018. The same landing site could be targeted in 2018, which had already been imaged, selected and certified (Fig. 10). This is fortuitous because the two-year delay in launch, is too short to identify, image, characterize, and select a new landing site from a number of possibilities given the normal (i.e., non emergency) HiRISE imaging cadence used for Mars landing sites. Even if there were time to start landing site selection over again, the same factors that drove the selection of western Elysium Planitia (Sects. 6.1 and 6.2) in 2016, drive the selection of the ellipse in 2018 to the same location and ultimately the same ellipse (resulting in the same communications conflict with the Curiosity rover).

The Type 1 trajectory for InSight launching in 2018 was selected by the InSight project in early 2016 and the landing site (E9) was unchanged. Current plans are to acquire ~15 more HiRISE images to cover the edge of the ellipse between April 2016 and February 2017. Slope and rock maps will be made of all unprocessed HiRISE images and an updated hazard map will enable new landing site probability maps and targeting of the safest ellipses for different launch dates in late 2017, prior to launch in May 2018.

7 Surface Characteristics of Landing Sites

7.1 Introduction and Geologic Setting

Western Elysium Planitia lies just north of the global dichotomy boundary between elevated heavily cratered southern highlands and lower standing, less cratered, northern plains. The formation of the northern lowlands is the oldest geological event recognized on Mars occurring in the pre-Noachian (Frey 2006), although younger tectonic and erosional processes have affected the dichotomy boundary since (McGill and Dimitriou 1990). The plains of western Elysium Planitia near the InSight ellipses are wedged between highlands to the south and west, a ridge of Medusae Fossae Formation to the east and southeast, Amazonian lavas from Elysium Mons to the north (Tanaka et al. 2014), and very young lavas from Cerberus Fossae and Athabasca Valles to the east (Vaucher et al. 2009).

The plains surface on which the InSight ellipses are located is mapped as an Early Hesperian transition unit (eHt) by Tanaka et al. (2014), which could be sedimentary or volcanic. A volcanic interpretation of the plains is supported by: 1) the presence of rocks in the ejecta of fresh craters ~0.4–20 km diameter arguing for a strong competent layer ~4–200 m deep and weaker material above and beneath (e.g., Golombek et al. 2013b; Catling et al. 2011, 2012), 2) exposures of strong, jointed bedrock overlain by ~10 m of relatively fine-grained regolith in nearby Hephaestus Fossae in southern Utopia Planitia at 21.9°N, 122.0°E (Golombek et al. 2013b), 3) platy and smooth Late Hesperian to Early Amazonian lava flows up to 200 m thick mapped in 6 m/pixel CTX images south of the landing site (Ansan et al. 2015), and 4) the presence of wrinkle ridges, which have been interpreted to be fault-propagation folds, in which slip on thrust faults at depth are accommodated by asymmetric folding in strong, but weakly bonded layered material (such as basalt flows) near the surface (e.g., Mueller and Golombek 2004; Golombek and Phillips 2010).

7.2 Terrains

Terrain mapping for InSight began early in 2013 and proceeded through three phases up to the final downselection to E9 in late 2015. These phases included: 1) inter-ellipse mapping of the initial 16 sites based on existing CTX and some HiRISE data, 2) inter- and intra-ellipse mapping following targeted CTX and HiRISE acquisition for 22 ellipses, and 3) HiRISE validation of the CTX terrain map as HiRISE image acquisition focused on four final landing ellipses. Phase 1 and 2 mapping was accomplished by the time of the First Landing Site Workshop. Phase 3 mapping followed the first landing site downselection (July 2013). Here we report on the major terrain units that were identified and verified during all three mapping phases with the primary mapping effort occurring during the analysis of the 22 ellipses during phase 2.

Mapping was carried out on CTX images and terrains were characterized based on their albedo and surface texture and by their inferred physical properties in THEMIS. In HiRISE, the different units identified in CTX showed variable rock abundance, presence or absence of bedforms, and variable textures that were largely related to meter to 100 m length-scale topography and roughness. THEMIS daytime and nighttime images were used to qualitatively draw correlations between the visual characteristics of the terrains and their thermal signatures. Throughout this process, the available HiRISE images were used to establish that CTX was capable of confidently identifying subtle differences between terrain types.

The entire mapping area was originally divided into four sub-regions during phase 1. Each region is distinguished by the different terrains present. These include the northeastern (E1–E3), northern (E5–E10, E17), central (E4, E11–E13, E18–E21), and southern ellipses (E14–E16, E22) (Figs. 4 and 5). The majority of the northeastern ellipses exhibit distinct lobate ridged terrain (Fig. 11a). We interpret the ridged terrain as lava flows that exhibit compressional surface folds that form in the crust of cooling lava flows (Gregg et al. 1998; Warner and Gregg 2003; Ansan et al. 2015). The preserved lava flow fronts and ridged morphology (most obvious at CTX resolution) speak to the terrain's relatively youthful age and likely thin regolith. Tanaka et al. (2014) mapped the E1–E3 region as the Hesperian-age transition undivided unit (Htu), which is stratigraphically younger than eHt. HiRISE images confirmed that E1–E3 are covered by large swaths of north-northeast trending secondary crater rays from Corinto as well as east-west trending Zunil secondaries (Fig. 12a). These secondary clusters appear bright in THEMIS daytime images and dark in nighttime THEMIS images, suggesting that the ejecta is fine-grained. The western margin of the E1–E3 ellipses is flanked by, and in some cases includes, the Medusae Fossae Formation.

The northern ellipses (Fig. 5) are characterized by the extensive coverage of smooth terrain. Ellipse E8, E9, and E10 exhibit greater than 90 % coverage (by area) of this unit. Smooth terrain is noted for its muted surface texture, constant moderate albedo, and slightly higher daytime THEMIS signature relative to all other terrain types (Figs. 7 and 11b). The uniform appearance of the smooth terrain is interrupted by fresh impact craters that exhibit bright halos in the CTX images. These same halos correspond with a dark daytime thermal signature (Fig. 7) and a bright nighttime signature, indicating that the ejecta has a higher thermal inertia than the surrounding terrain (see Sect. 7.4). At the initial stage of mapping, HiRISE images were not available over the smooth terrain. However, HiRISE images acquired during specific targeting phases of the northern ellipses (phase 2 and 3 mapping) confirmed that the smooth terrain was topographically uniform and lacked rocks that could be observed above the resolution limit of HiRISE (Fig. 12).

Within ellipses E5–E7, three additional terrain types were identified that exhibit a variety of albedo and textural characteristics (Fig. 5). The etched terrain is characterized in CTX by

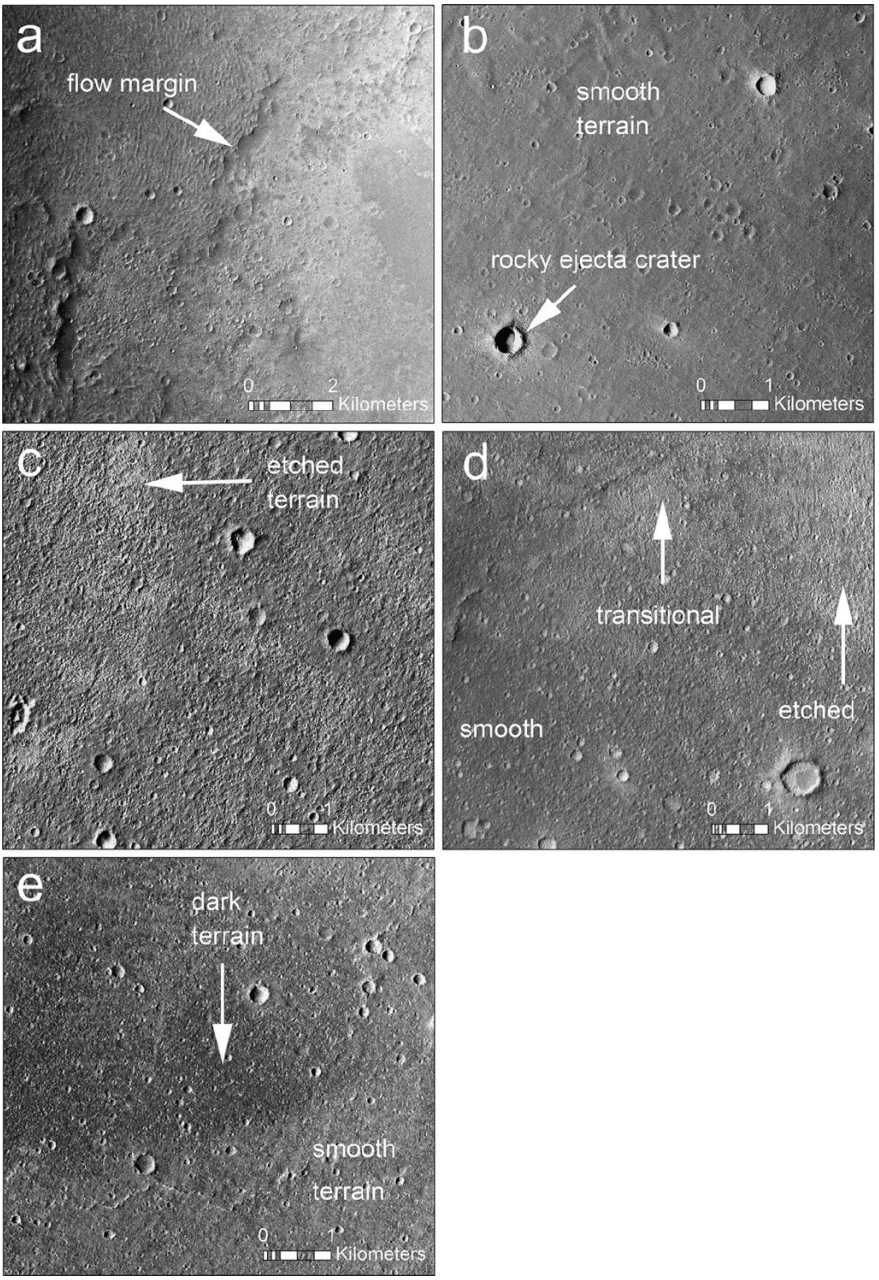

Fig. 11 CTX montage of the five most common terrain types in the 22 InSight ellipses. (**a**) Image P16_007448_1822 of ridged terrain in the northeastern ellipses. A lava flow lobe extends from the left of the image. (**b**) Image D04_028757_1855 of characteristic smooth terrain in the northern ellipses, including a fresh rocky ejecta crater. (**c**) Image D01_027702_1815 showing a patch of higher albedo etched terrain amongst smoother transitional terrain types. (**d**) Image P15_007000_1786 showing the transition from smooth terrain to etched terrain. Here the transitional terrain type forms a gradational contact between etched and smooth. (**e**) Image D04_028757_1855 of the dark, low albedo terrain type in the northern ellipses. Smooth terrain that is adjacent to the dark unit shows a relatively higher albedo

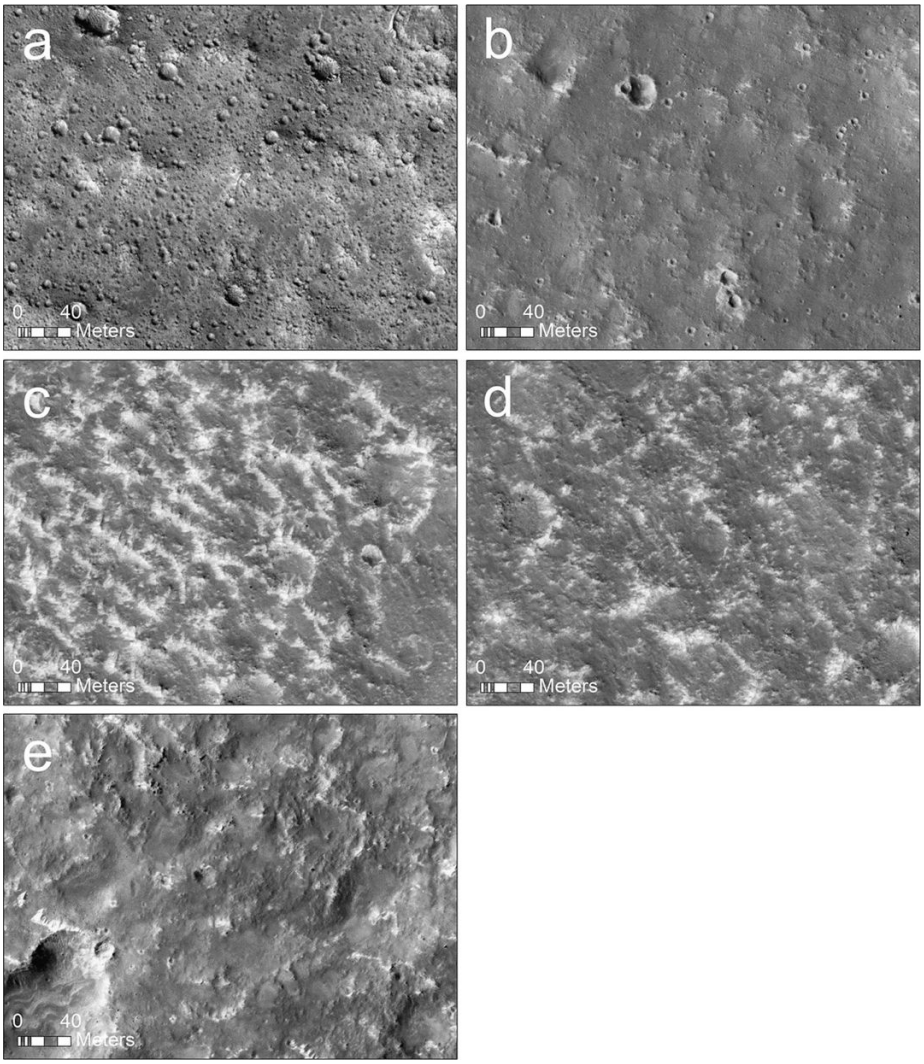

Fig. 12 HiRISE montage of the five most common terrain types in the 22 ellipses. (**a**) Image ESP_030872_1835 of the ridged terrain. A ridge crosses the center of the image from east to west. Ridges here are superposed by a dense field of Corinto and likely Zunil secondary craters. (**b**) Image ESP_037961_1845 showing the type smooth terrain in the northern ellipses. Only a handful of meter-size rocks are visible and slopes are minimal. Note characteristic bright ejecta around Corinto secondary craters. (**c**) Image ESP_032027_1820 displaying etched terrain. Lighter-toned eolian bedforms preferentially collect within the depressions of the etched terrain. Meter-size rocks occur in a higher abundance between the bedforms. (**d**) Image ESP_032027_1820 showing gradational terrain that occurs adjacent to the etched terrain in (**c**). (**e**) Image ESP_035073_1840 displaying the moderately rough and low albedo dark terrain

a relatively high albedo (Fig. 11c). In THEMIS images (Fig. 7), the etched terrain shows a variable, but generally higher thermal inertia. The etched surface texture is represented by remnants of smooth terrain, interspersed with topographically lower (1–5 m) regions that are commonly (but not always) infilled with higher albedo bedforms. Rocky ejecta craters

that are brighter in CTX and HiRISE images on the smooth terrain still appear in the etched and other terrain types, yet lack the same albedo contrast. Furthermore, HiRISE revealed not only eolian ripples within the etched unit, but a high abundance of meter-size rocks, raising concern for landing safety. Elevated remnants of the smooth terrain, including 5- to 10 m-high pedestal craters (Warner et al. 2016, this issue), occur within the etched terrain. These observations suggest that the etched terrain formed as a result of the incomplete erosion and stripping of the smooth terrain, likely by eolian deflation of loosely consolidated regolith.

The regolith across this Hesperian-age region is likely a product of both impact gardening and re-working of finer, sand-sized particles by the wind (Sect. 7.8; Warner et al. 2016, this issue). On the smooth terrain, bedforms of sand-sized materials occur only in the continuous ejecta blankets of the rocky ejecta craters. This suggests that either the rockier surfaces and crater rims act as a trap for mobile sediment and/or the impacts themselves produce a sand-sized fraction that is mobilized into bedforms. The continuity of the bedforms in a one crater diameter annulus around all fresh rocky craters indicates that at least some component of sand is derived locally from impact events. The degradational sequence of craters suggests that the sand migrates across the ejecta blanket, often becoming trapped within the crater itself (Sweeney et al. 2016; Warner et al. 2016, this issue). Burial of craters by bedload-transported sand, degradation of crater rims by eolian erosion, and constant impact gardening are therefore the primary geologic processes that shaped and likely formed the smooth terrain, generally similar to the Gusev cratered plains (e.g., Golombek et al. 2006). Stripping of that smooth terrain would therefore not only create a topographic depression that could facilitate further sand trapping, but possibly reveal a deeper boulder-rich regolith unit at depth. Alternatively, if boulders occur within the uppermost column of regolith (within the smooth terrain), deflation of the smooth terrain could produce a rocky lag and a concentration of boulders (Warner et al. 2016, this issue). The observed rock abundance on the surface and in the etched depressions is consistent with concentrating boulders as a lag after removal of fines.

The interpretation of the etched material as a modified form of the smooth terrain is strengthened by the observation of transitional terrain types between the two units. Figure 11d highlights a gradational contact between smooth terrain and the higher albedo etched terrain in CTX imagery. This unit, known as gradational terrain, has an intermediate rock abundance, albedo (some brighter bedforms present), thermal inertia, and surface roughness relative to smooth and etched terrains (Figs. 7 and 12d). The gradational unit covers a relatively large percentage of the northern ellipses E5–E7 (up to 20 % by area), making those landing sites less ideal with respect to ellipses E8–E10, which completely lack the rougher/rockier surfaces (Fig. 5). Less gradational contacts between smooth and etched units occur where 100 m to km-size patches of etched material occur amongst a broader unit of smooth terrain. This unit, which is locally present in the northern, central and southern ellipses is mapped as patchy etched terrain.

Dark terrain (Figs. 11e, 12e) also occurs as a transitional unit between the smooth and etched surfaces, yet it lacks the bright eolian bedforms of the etched and gradational surface types. It also has lower rock abundance than the etched terrain and a similar abundance to gradational terrain. We interpret the dark terrain as a similarly modified version of the smooth terrain where aeolian deflation of overlying higher albedo material has exposed a lower albedo, more indurated surface that lacks superposing bedforms. The higher thermal inertia is consistent with its generally cool daytime thermal signature (Fig. 7). Dark terrain is more abundant in the northernmost ellipses than elsewhere in the mapped region.

The central ellipse terrains represent a shift from the north in terms of surface roughness, albedo, and thermal characteristics (Fig. 5). E4 and E11 were mapped as containing 50 %

to 56 % by area (respectively) of the transitional (gradational & patchy etched) and etched terrain types. In addition, these rougher and rockier terrains dominate the central portion of the ellipse, making both ellipses less ideal for landing. Further south, E12 and E13 are similarly dominated by the etched and transitional terrains. Acquisition of HiRISE images over the central ellipses revealed that the smooth terrain, as it was initially mapped in CTX, has a rougher surface texture in comparison to the smooth terrain in the northern ellipses. HiRISE images revealed the presence of arcuate ridge-like landforms that we interpreted to represent partially degraded remnants of impact crater rims. This smooth terrain has a similar albedo and thermal inertia to the smooth terrain to the north.

The southern-most ellipses are dominated by transitional terrain units (Fig. 5). Although they lack a high abundance of the etched terrain, these rougher and rockier transitional surfaces make them less ideal when compared to the northernmost ellipses. Furthermore, the southern ellipses exhibit some overlap with steep highland escarpments. Analysis of MOLA shot points across the highland scarps revealed slopes in excess of the 15° landing requirement (Fig. 6). The Medusae Fossae Formation is also included within the eastern-most ellipse margin of both E14 and E15.

The CTX and HiRISE mapping phases concluded with the recommendation that four of the northern ellipses are mostly covered with the smooth terrain, which is the most benign terrain in terms of rocks and slopes and thus safest for landing. Geologic and geomorphic observations of the smooth terrain at these sites also suggest the presence of a meters-thick regolith that is better for HP^3 penetration. Ultimately, E9 was deemed the most suitable because of its near complete coverage by smooth terrain.

7.3 Global Thermal Inertia and Albedo

Thermal inertia is defined as $I = (k\rho c)^{1/2}$, where k is the thermal conductivity, ρ is the bulk density of the surface material, and c is the specific heat, and represents the resistance to change in temperature of the upper 2–30 cm of the surface. Fine particles change temperature quickly and so have a lower thermal inertia, whereas higher thermal inertia surfaces are composed of sand, duricrust, rock fragments, or a combination of these materials. Many equally plausible scenarios, such as mixtures of particles or the presence of duricrust, can result in surfaces with moderate thermal inertias. The albedo, or surface reflectivity or brightness of surfaces on Mars is generally related to the amount of bright, red dust covering the surface (Christensen and Moore 1992; Moore and Jakosky 1989; Mellon et al. 2008; Putzig et al. 2005; Golombek et al. 2008a).

A general relationship has been found between kilometer scale global thermal inertia and albedo data and specific materials found in the surface layer at the seven prior landing sites (e.g., see reviews by Christensen and Moore 1992; Golombek et al. 2008a). Five landing sites sample two (B and C) of the three dominant global thermal inertia and albedo units that cover ~80 % of the surface of Mars (Putzig et al. 2005). The VL, Spirit, PHX and MSL landing sites sample the moderate thermal inertia and intermediate to high albedo unit C (Fig. 13, Table 7) that is dominated by crusty, cloddy, blocky or frozen soils (duricrust) with various abundances of rocks and bright dust (Golombek et al. 2008a; Jakosky and Christensen 1986; Christensen and Moore 1992; Moore and Jakosky 1989; Mellon et al. 2000, 2008; Putzig et al. 2005; Jones et al. 2014). The Opportunity landing site is in the moderate thermal inertia and low albedo surface unit B that is relatively dust free and composed of dark eolian sand and/or increased abundance of rocks. MPF has an albedo between units A and B, but has higher thermal inertia and resembles unit C sites with less dust (similar to dust devil tracks swept free of dust traversed by Spirit) and stronger duricrust. Other parts of the Curiosity traverse have higher thermal inertia, consistent with the moderately dusty cemented

Table 7 Landing site ellipse remote sensing data

Site	InSight E9	MSL	Phoenix	Opportunity	Spirit	MPF	VL 2	VL 1
Latitude of Ellipse, deg	4.323	−4.4868	68.15	−2.06	−14.64	19.13	47.67	22.27
Longitude of Ellipse, +E, deg	135.663	137.4239	233.97	353.77	175.06	326.78	134.26	312.03
Latitude of Lander, deg		−4.589467	68.22	−1.95	−14.57	19.09	47.62	22.27
Longitude of Lander, +E, deg		137.441633	234.25	354.47	175.47	326.74	134.23	312.05
MOLA Elev., km, Ellipse center	−2.664	−4.4	−4.143	−1.440	−1.920	−3.700	−4.500	−3.600
Range	−3.101 to −2.530	−4.5 to −4.1	−2.6 to −2.0	−1.4 to −1.6	−1.8 to −1.9			
Lander elevation		−4.501	−4.126	−1.384	−1.941	−3.68	−4.5	−3.6
Geoid, km, COM	3395.700	3395.641	3380.724	3395.526	3394.227	3393.482	3386.349	3339.299
1.2 km bi-dir slope, deg, mean ± SD,	0.23 ± 1.12	1.23 ± 1.05	0.37 ± 0.31	0.15 ± 0.18	0.20 ± 0.44	0.25 ± 0.66	0.29 ± 0.29	0.26 ± 0.96
RMS, deg	1.1	1.617	0.48	0.26	0.49	0.706	0.410	0.995
n	7433	841	2356	680	679			
900 m bi-dir relief (m), mean ± SD,	21.7 ± 21.3	18.5 ± 15.5						
RMS	30.4	24.1						
n	7427	770						
MOLA Pulse Width, m, mean ± SD,	1.24 ± 2.02	1.99 ± 1.54	1.33 ± 1.27	0.84 ± 0.46	1.34 ± 1.11	1.52 ± 1.81	1.22 ± 0.55	1.54 ± 2.4
RMS	2.37	2.52	1.84	0.96	1.74	2.36	1.34	2.85
n	2414	233	47371	2357	757	25853	10560	19848

Table 7 (*Continued*)

Site	InSight E9	MSL	Phoenix	Opportunity	Spirit	MPF	VL 2	VL 1
Self affine 100 m Allan dev, m	4.1	4.0		3.4	5.8	5.0		1.8
100 m RMS slope, deg	2.1	2.3		1.9	3.3	2.9		1
5 m RMS slope, deg, a-dir	2–3	5.1	1.8	1.7–3.3	3.7 Cr Plns ~10 ColHills	4.9–5.1	1.6	5.1
3.5 cm radar RMS slope, deg				0.9 ± 0.2	4.7 ± 1.6	4.7 ± 1.6	2.0 ± 0.3	4.7 ± 1.8
3.5 cm radar reflectivity				0.05 ± 0.02	0.04 ± 0.02	0.05 ± 0.01	0.06 ± 0.01	0.04 ± 0.03
IRTM I, SI, mean ± SD	77 ± 1.4	335		319 ± 5	284 ± 0	434	338 ± 14	355
Range	76–79			314–326	284–284	396–533	321, 355	330–360
n	4	1		4	4		16	
Lander value	NA	80		315	284	434	338	355
TES I, SI, mean ± SD (Mellon)	257.8 ± 5.4	407 ± 69		230 ± 18	286 ± 35	418 ± 36	242 ± 16	320 ± 15
Range	249–268	276–511		194–256	216–325		192–292	
n	48	7		32	27	512	450	570
Lander value				256	256	400	203	302
TES I, SI, mean ± SD (Christensen)	221.2 ± 4.4	323 ± 31		215 ± 13	239 ± 20	387 ± 29	246 ± 14	288 ± 9
Range	212–232	295–388		187–252	200–275	338–460	176–291	264–333
n	45	8		32	27	288	287	287
Lander value		335–425		223	248	376	250	284
TES I, SI, mean ± SD (Putzig)	217.6 ± 21.8	374 ± 32	164 ± 40	189 ± 29	271 ± 56	393 ± 49	242 ± 22	292 ± 29
Range	138–284	313–457	81–251	112–248	117–388	278–681	131–314	181–576
n	314	44	176	183	164	1774	1790	1784
Lander value		287	200	222	300	386	234	283

Table 7 (*Continued*)

Site	InSight E9	MSL	Phoenix	Opportunity	Spirit	MPF	VL 2	VL 1
THEMIS I, mean ± SD	100–220	365 ± 50						
Range	80–240	370–402						
IRTM FC I, SI, mean ± SD	69.5 ± 4.95	268		307 ± 9	248 ± 22	338 ± 16	260 ± 12	284 ± 21
Range	66–73			297–318	230–276	317–363	238–280	260–326
n	2	1		4	4		16	
Lander value		64		307	248	338	260	284
IRTM albedo, mean ± SD	0.2535 ± 0.001	0.239		0.138 ± 0.055	0.150 ± 0.069	0.215	0.243 ± 0.06	0.25
Range	0.253–0.254			0.090–0.190	0.090–0.211	0.19–0.23		0.23–0.25
n	2	1						
Lander value		0.239		0.194	0.236	0.215	0.254	0.25
TES albedo, mean ± SD	0.2395 ± 0.001	0.242 ± 0.007	0.204 ± 0.002	0.171 ± 0.026	0.222 ± 0.023	0.218 ± 0.012	0.304 ± 0.012	0.255 ± 0.006
Range	0.237–0.243	0.231–0.251	0.200–0.208	0.124–0.235	0.173–0.265			
n	45	8	22					
Lander value		0.22	0.2	0.12	0.19, 0.26	0.19	0.24	0.22
DCI, mean ± SD	0.94	0.954 ± 0.006		0.969 ± 0.005	0.950 ± 0.010	0.959 ± 0.008	0.947 ± 0.012	0.952 ± 0.007
Range		0.943–0.966		0.956–0.978	0.930–0.970	0.929–0.990	0.906–0.991	0.913–0.988
n		29		123	107	1147	1146	1146
Lander value		0.96189		0.973	0.964	0.967	0.924	0.945
Rock abun, %, mean±SD (IRTM)	4, 9	10		5 ± 3	7.5 ± 1	18	17	16
Range				1–7	7–8 (bit of 3)	18–25		8–19
n				4	2			
Lander value		8.5		∼3	7	19	16	16

Table 7 (*Continued*)

Site	InSight E9	MSL	Phoenix	Opportunity	Spirit	MPF	VL 2	VL 1
Rock abun, %, mean ± SD (TES)	4.0	19[a]		very low	11 ± 4	12 ± 4	13 ± 4	8 ± 5
Range	1–7							
Rock abun, (HiR)								
%, mean ± SD	1.2 ± 3.2	3.9 ± 3.0	2–3		5	10–20	30	8
Range		0–15						
n		1904						
% Area >1 m Dia.	0.0001		0.0004	0.04	0.15	1	1	0.8
Rocks, mean/range				0.001–0.15	0.15–0.2	1–2		0.15–1.1

Notes: Latitude, Longitude in planetocentric MOLA IAU/IAG 2000 cartographic frame, positive east. MOLA elevations with respect to the MOLA geoid (Smith et al. 2001b), both measured from the center of mass (COM). 1.2 km bi-directional (bi-dir) slopes calculated as in Anderson et al. (2003). 900 m bi-directional relief (bi-dir) calculated as in Golombek et al. (2012a). MOLA pulse width is slope corrected data from Neumann et al. (2003). Self-affine 100 m Allan deviation and RMS slope are calculated as described in Anderson et al. (2003). RMS slope at 5 m baseline from Kirk et al. (2003, 2008), Beyer et al. (2003) and Golombek et al. (2012a) from MOC and HiRISE stereogrammetry and photoclinometry. Radar data are 3.5 cm X-band measures of RMS slope and reflectivity as reported in Golombek et al. (2003a, 2008a). IRTM data set from P. Christensen includes bulk thermal inertia from Kieffer et al. (1977), Palluconi and Kieffer (1981), and Christensen and Malin (1988); rock abundance from Christensen (1986); fine-component thermal inertia from Christensen (1982, 1986); and albedo from Pleskot and Miner (1981) at 1 or 2 pixels per degree. TES data from Mellon et al. (2000) (Mellon) and Christensen et al. (1992) (Christ.) at 8 pixels per degree and nighttime thermal inertia from Putzig and Mellon (2007a) (Putzig) at 20 pixels per degree. THEMIS thermal inertia data from Fergason et al. (2012) for MSL and Sect. 7.4 for InSight. All thermal inertia values in SI units or $J\,m^{-2}\,s^{-1/2}\,K^{-1}$. TES albedo from Christensen et al. (2001) at 8 pixels per degree. Dust Cover Index (DCI) from Ruff and Christensen (2002) at 16 pixels per degree. TES rock abundance from Nowicki and Christensen (2007) at 8 pixels per degree. HiRISE rock abundance and number of rocks for MSL sites as reported in Golombek et al. (2012b) for 150 m cells to the nearest one-tenth rock abundance with no minimum. HiRISE rock abundance for PHX from Golombek et al. (2012b) and VL1, VL2, and MPF from Golombek et al. (2008a). Percent (%) area covered by rocks >1 m diameter (0.5 m high) from model size-frequency distribution curves pinned to total rock abundance as described in Golombek and Rapp (1997) and Golombek et al. (2003b). Lander data for IRTM and TES thermal inertia (Putzig), TES albedo, and IRTM rock abundance as reported in Golombek et al. (2008b)

[a]Data point partially in the ellipse

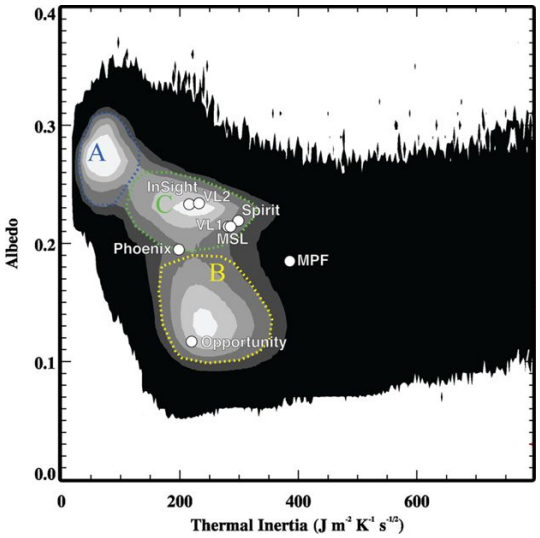

Fig. 13 Global TES thermal inertia versus albedo showing the three major thermal inertia-albedo units (*A*, *B*, and *C*) that make up ~80 % of the surface of Mars along with the seven previous landing sites and the final InSight landing site. Unit *A* has high albedo and very low thermal inertia and is dominated by potentially thick bright red dust with very low rock abundance. Unit *B*, in which Opportunity landed, has low albedo and is relatively dust free. Unit *C*, in which VL1, VL2, Spirit, Phoenix and MSL landed has moderate thermal inertia and intermediate to high albedo that is dominated by crusty, cloddy, blocky or frozen soils (duricrust) with various abundances of rocks and bright dust. MPF has an albedo between units *B* and *C*, but has higher thermal inertia. The InSight landing site falls in unit *C* and should be as dusty as VL2 and the dusty parts of the Gusev cratered plains traversed by Spirit, but is dominated by unconsolidated sand or very weakly consolidated soil. Plot adapted from Putzig et al. (2005). Thermal inertia and albedo data are from TES (Putzig and Mellon 2007a, 2007b)

sedimentary rocks (Williams et al. 2013; Grotzinger et al. 2014). The third main thermal inertia and albedo unit of Mars has high albedo and very low thermal inertia (unit A) and is dominated by potentially thick bright red dust with very low rock abundance. Such dusty areas have been eliminated as possible landing sites for solar-powered or rover missions due to concerns about dust coating the solar panels (reducing power) and sinkage, as this material does not appear to be load bearing nor trafficable (Golombek et al. 2008a). Comparisons of soils and rocks covering the landing sites indicate that the main contributor to the bulk thermal inertia is the degree of induration or cementation (and grain size) of the soils or fine component, rather than rocks, which generally cover less than one third of the surface (Jakosky and Christensen 1986; Mellon et al. 2000, 2008; Putzig et al. 2005; Fergason et al. 2006a).

The InSight landing site region falls in a restricted portion of unit C with slightly higher albedo and slightly lower thermal inertia than VL1, Spirit, and MSL, but similar to VL2, the existing landing site with the most similar thermophysical properties (Fig. 13, Table 7). The selected landing site E9 has albedo and thermal inertia similar to VL2, which derives it low thermal inertia and high albedo from a preponderance of drift deposits (Golombek et al. 2008b). The relatively low thermal inertia of the InSight landing site (~200 $J\,m^{-2}\,K^{-1}\,s^{-1/2}$) is consistent with a surface composed of cohesionless sand size particles or a mixture of slightly cohesive soils (cohesions of less than a few kPa), some rocks and thermally thin coatings of dust (e.g., Golombek et al. 2008a and Sect. 7.4). The relatively high albedo of the InSight landing sites (0.24) argues for a thin coating

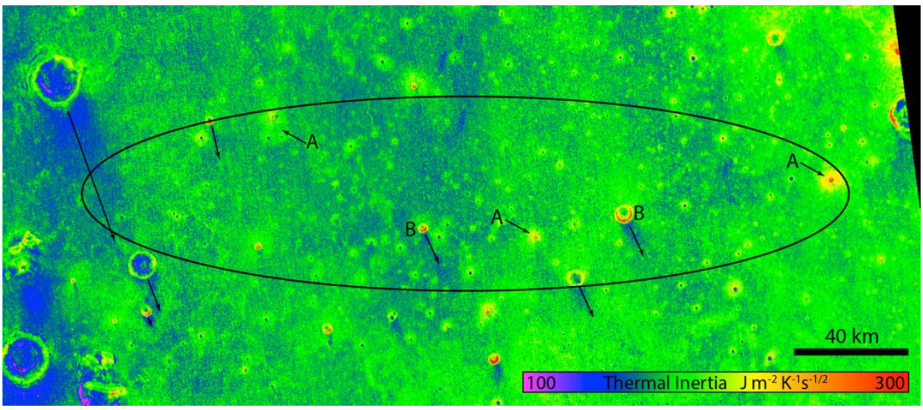

Fig. 14 THEMIS thermal inertia map of the InSight landing region produced using a numerical model predicting Mars surface temperatures (Kieffer 2013) and mosaicking tools described by Edwards et al. (2011a, 2011b) made available by these authors. Linear stretch excludes extreme values for clarity. The *black ellipse* is the approximate location of the E9 landing ellipse oriented east-west. *Black arrows* indicate examples of low thermal inertia material downwind of topographic highs. Examples marked *A* show relative high thermal inertia terrains associated with rocky ejecta craters. Examples marked *B* show crater rims with a relatively high thermal inertia value, likely due to the presence of rocks. Standard thermal inertia mapping procedures are described by Fergason et al. (2006a) and references therein. To improve spatial coherence and limit the expression of surface heterogeneity (Putzig and Mellon 2007b), potential subsurface layering (Putzig and Mellon 2007a), or atmospheric variability (Montabone et al. 2015), we have only selected data acquired in the $060 < L_S < 120$ range, i.e., during the predicted annual atmospheric dust minimum. At mid/low latitudes during this period, nighttime water ice clouds may be present, and if present prevents efficient radiative cooling of the surface, and results in warmer surfaces, i.e. higher apparent thermal inertia values. However, we note that the effect of water ice clouds is not predicted to be significant outside low thermal inertia surface units (Steele et al. 2014; Wilson and Guzewich 2014), and is ignored in this analysis. Additional parameters required for thermal inertia derivation are the albedo, taken from TES Lambertian albedo map (Christensen et al. 2001) and column dust opacity using L_S-dependent climatological values by Smith et al. (2001a). Ultimately, thermal inertia values are derived with errors estimated at ± 15 % (Fergason et al. 2006a)

of dust similar to the dusty portions of the Gusev cratered plains, which have an albedo of 0.26 (Golombek et al. 2005). The bulk thermal inertia is too high for significant deposits of underdense or non-load-bearing materials and clearly exceeds the minimum thermal inertia constraint of $<$100–140 J m^{-2} K^{-1} s$^{-1/2}$. Furthermore, because the thermal differencing estimates of rock abundance are relatively low for this area (Christensen 1986; Nowicki and Christensen 2007), the fine component thermal inertia is only slightly lower than the bulk thermal inertia and well above the minimum constraint, further limiting the amount of dust. The TES dust cover index (Table 7), which includes a more explicit measure of the presence of a thin dust layer (Ruff and Christensen 2002), of the InSight landing site (0.94) is similar to the VL2 landing site and only slightly dustier than VL1 and Spirit and consistent with a thin coating of dust.

7.4 THEMIS Thermophysical Properties

We have generated a regional thermal inertia map (100 m spatial scales) from predawn temperature data acquired by THEMIS band 9 (12.57 μm) (Christensen et al. 2004) between MY 30 and 32 during low-dust seasons to minimize the atmospheric impact on the derived values. The resulting thermal inertia map (Fig. 14) displays values ranging from $\sim$70 J m^{-2} K^{-1} s$^{-1/2}$ to 390 J m^{-2} K^{-1} s$^{-1/2}$, but 99 % of the area has a thermal inertia of

130 to 220 J m^{-2} K^{-1} s$^{-1/2}$. Within the E9 ellipse, this range is even smaller, demonstrating high thermophysical homogeneity at the 100 m scale over the entire landing region. The median regional thermal inertia is ~180 J m^{-2} K^{-1} s$^{-1/2}$, corresponding to cohesionless ~170 μm material (fine sand) based on laboratory work and theoretical relationships (Presley and Christensen 1997a; Piqueux and Christensen 2011). Higher thermal inertia values are expected to be associated with medium to coarse sand, and will likely include mixtures of grain sizes, including larger clasts such as those surfaces observed at Gusev crater (Golombek et al. 2005, 2008a; Fergason et al. 2006b). The corresponding diurnal skin depth values (i.e., typical penetration depth of a diurnal temperature wave) is a maximum of ≤6 cm indicating that the upper few cm of the surface layer are characterized by these thermal inertia values (Fig. 14).

The lowest thermal inertia values in the landing region (e.g., ~70 J m^{-2} K^{-1} s$^{-1/2}$) are rare, and typically are observed within depressions probably trapping atmospheric dust and very fine sand, or on the lee side of positive topographic features. Bedforms in association with these low inertia values are observed in high-resolution visible images. While these low thermal inertia values are associated with very fine material (i.e., a few tens of microns in diameter, Presley and Christensen 1997a, 1997b), they are still significantly coarser and denser than the widespread non-load-bearing mid/low latitude dust units found elsewhere on Mars. It is also possible that these low inertia values result from fine sand (100–200 μm) with a very thin coating (<1–2 mm) of dust (several μm diameter particles).

The highest thermal inertia values (i.e., 350–390 J m^{-2} K^{-1} s$^{-1/2}$) are also uncommon, associated with crater rims and ejecta blankets, as expected for rocky ejecta craters. However, while these inertia values correspond to the regional highs, they remain relatively low in the range of observed Martian values (~20–2,100 J m^{-2} K^{-1} s$^{-1/2}$, Mellon et al. 2000), indicating that at the 100 m spatial resolution, widespread exposures of bedrock are not detected in the landing region. Similarly, high rock accumulations at the surface or partially buried, are not consistent with such low thermal inertia values. We note that rocks are defined here as rocky material with typical sizes similar to or larger than a diurnal skin depth in bedrock, e.g., ~15 cm (Christensen 1986).

Regolith induration is not inconsistent with the derived thermal inertia values, however thermal modeling of cemented regolith shows that the volume of the cementing phase would need to be minimal (e.g., typically <0.1 % in volume) with little impact on the mechanical properties (Piqueux and Christensen 2009). Comparison of the cohesion of surface soils at landing sites with their thermal inertia would limit the cohesion to less than a few kPa, consistent with very weakly bonded soils on Earth (Golombek et al. 1997, 2008a). If a cementing phase is present and increases the regolith thermal conductivity/inertia, the derived grain sizes are overestimated by unknown factors. While the spectral signature of atmospherically deposited dust is ubiquitous in the InSight landing region (i.e., relatively high dust index, Ruff and Christensen 2002), thermal inertia values are nowhere dominated by very fine material (at the 100 m scale), suggesting that dust may form an optically thick but thermally thin coating (hundreds of μm) on most surface materials in this region of Mars. This interpretation is supported by the similarity of the dust cover index in the InSight landing site region (0.94) with dusty locations of the Gusev cratered plains explored by Spirit (e.g., Golombek et al. 2005, 2006).

A surface expression of the predominant regional wind direction is lower thermal inertia values to the south-southeast of positive topographic features (typically crater rims) compared to the regional values (~30 % lower, Fig. 14). The width and length of these features is a function of the size of the obstacle that creates them, and we interpret these low thermal inertia values as wind tail features corresponding to fine eolian material, protected from the

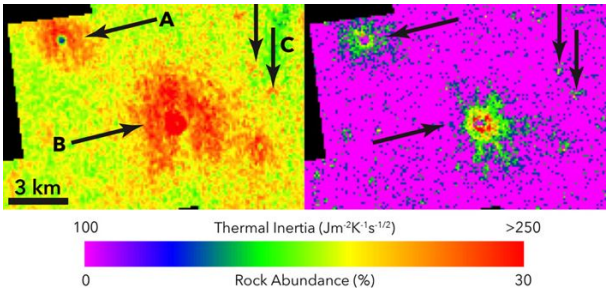

Fig. 15 Comparison of THEMIS thermal inertia map (*left*) and HiRISE derived rock abundance derived in Sect. 7.5 (*right*) illustrating the excellent correlation between both mapping products. *A*: example of a rocky ejecta blanket showing similar extent in the visible and infrared data; *B*: example of a rocky ejecta blanket that is smaller in images than in the infrared (see text for discussion); *C*: example of smaller and more degraded rocky ejecta blankets with faint but noticeable signatures in the thermal inertia and rock abundance maps

regional wind by the associated topographic features (Greeley et al. 1974, 2003; Sullivan et al. 2005). These lower thermal inertia streaks are typically consistent with very fine sand or coarser sand covered with a thin coating of dust, but not consistent with thick deposits of dust.

For completeness, we have also generated a thermal inertia map (not shown here) using nighttime data acquired one half Mars year later (i.e., $230° < L_s < 320°$) in order to identify seasonal variations (Piqueux et al. 2014), indicative of surface or subsurface heterogeneity (Putzig and Mellon 2007a). This approach highlights subsurface physical properties of the regolith at depths significantly larger than accessible with diurnal temperature variations (e.g., several 10's of cm to m depending on the material properties). Generally, we find no clear indication of widespread thermal inertia variation rising above the expected error bars (e.g., several tens of percent when comparing quantitative maps), indicative of no detectable subsurface heterogeneity within a few tens of cm of the surface. We have only found nine cases of crater interiors displaying a behavior consistent with a low thermal inertia material on top of a higher thermal inertia material, interpreted as dust on top of coarser sandy or rocky material.

A comparison between the rock abundance derived from HiRISE shadows (Sect. 7.5) and the THEMIS thermal inertia map (Fig. 14) shows an excellent correlation (Fig. 15). This correlation is anticipated because fines have a lower thermal inertia than rocks (Christensen 1986; Nowicki and Christensen 2007), and therefore the rocky ejecta blankets where they are preferentially concentrated stand out with higher inertia values than the surrounding background material. However, while the spatial correlation between the high rock abundance and the thermal inertia is often very close (Fig. 15A), the lateral extent of ejecta blankets can be larger in thermal maps than from the rock count (Fig. 15B). This difference is likely because rocks >1 m can be detected in HiRISE, whereas thermal data is sensitive to a continuum of materials larger than pebbles (∼3 cm, Jakosky 1986), with rocks being defined as ∼15 cm size clasts in thermal differencing maps (Christensen 1986). As a result, rocks too small to be detected in HiRISE images are large enough to control the local thermal inertia values. In addition, smaller craters resolved on the rock abundance maps display a slightly enhanced thermal inertia (Fig. 15C). Based on the excellent correlation between rock abundance measured in HiRISE images and thermal inertia, we expect no unusual rock concentrations in areas without HiRISE coverage.

Using the HiRISE-derived rock abundance (Fig. 16c) in conjunction with a model for deriving the effective thermal inertia of the rock population based on size (Golombek et al.

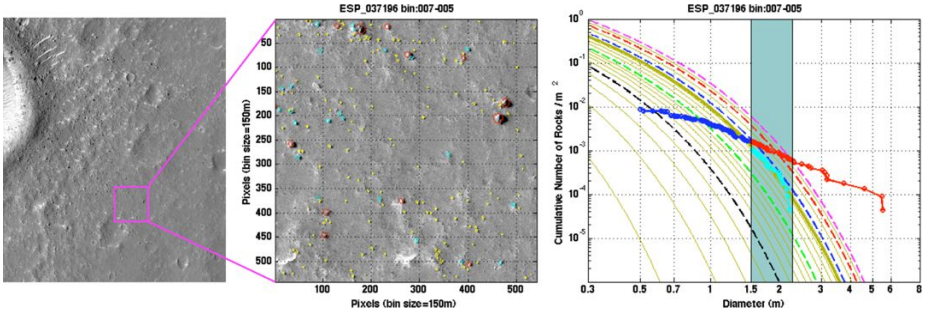

Fig. 16 HiRISE image, rock detections, and size-frequency distributions for a portion of the image. Fresh rocky ejecta crater (*left*) and the location of the 150 m square tile in which rock detections in center are shown in HiRISE image ESP_037196_1840. Rock detections in *red* are >2.25 m diameter and are mostly steep hills or scarps with shadows. Rock detections <1.5 m are shown in *yellow* and rock detections in *light blue* are in between. The size-frequency distribution plot (*right*) of cumulative number of rocks per m^2 versus diameter shows all the detections including rocks >1.5 m diameter in *red*, those smaller than 1.5 m in *dark blue*. The rocks shown in *light blue* are between these two diameters only (highlighted in *light blue*) and fit the model distribution for 18 % rock abundance shown in *mustard*. A family of exponential model rock distributions (Golombek et al. 2003b, 2008b, 2012b) are shown for total rock abundance of 1 % to 40 %, with 5 % in *black*, 10 % in *green*, 20 % in *blue*, 30 % in *red*, and 40 % in *pink*. These distributions are derived by numerically integrating exponential functions in cumulative fractional area covered by rocks versus diameter and so have flatter shapes in log-log plots. Detections greater than 2.25 m diameter are captured as extra strikes in the hazard analysis. Note the relatively flat slope of entire SFD, resembling power law distributions for single fragmentation (e.g., Turcotte 1997; Melosh 1989), and steeper slopes for just the rocks in *light blue* that resemble power law distributions for multiply fragmented distributions

2003b), and an algorithm predicting martian temperatures as a function of the surface material properties (Kieffer 2013), we have deconvolved the radiance contributed by rocks of all sizes from the measured radiance by THEMIS, and we assigned the difference to the fine component contribution of the regolith. This synthetic signal was then converted to equivalent thermal inertia values. Generally, the fine component thermal inertia values are close to the regional bulk thermal inertia in areas with few rocks, indicating a reasonable fit using the model for the vast majority of the mapped area and surfaces without rocks are low cohesion sandy soils. The deconvolution leads to unrealistically low fine component inertia values in locations of the highest rock concentrations, suggesting that the rock distribution model over-predicts the fraction of small rocks. We note that a deficit of small rocks was observed in dusty and low-inertia areas along the Spirit rover traverse in the Gusev cratered plains (Golombek et al. 2006), suggesting that dusty areas with low thermal inertia around the rocky ejecta craters could be an explanation for the model over-predicting the concentration of small rocks.

7.5 Rocks

Measurement of rocks in HiRISE images for the InSight landing ellipses utilized the rock shadow segmentation, analysis, and modeling method that was successfully developed for the PHX landing site selection (Golombek et al. 2008b) and improved upon for the MSL landing site selection (Golombek et al. 2012b). As was done for previous rock measurement campaigns, a series of pilot studies were conducted to make sure that the automated algorithm for detecting and measuring the rocks was accurately reflecting what a human observer sees and that they could be fit by a model distribution that could be used to extrapolate the rock distribution to smaller diameters than could be measured but which could be

hazardous for a lander. The first pilot study for InSight used image samples surrounding six rocky ejecta craters selected from three HiRISE frames in the smooth terrain. Forty-eight, 150-meter square tiles were chosen within three crater diameters to represent high, intermediate, and low rock abundances. The study compared automated SFDs for rocks $\geq$1 m with those from human observers for the same tiles. Ambiguous rock candidates and obvious false detections (e.g., shadows adjacent to steep scarps) were deleted manually from the automated detections. Initial SFDs (cumulative number of rocks per m^2 versus diameter) measured resembled power laws (straight lines on log-log plots) with fairly flat slopes for fresh craters (e.g., Fig. 16) and steeper slopes for more degraded craters. The flat slopes for the fresh craters have far fewer small rocks than typical SFDs and many very large rocks (>3 m diameter). This distribution resembled theoretical power law distributions derived by Turcotte (1997) in which single fragmentation events have negative power law slopes <2 and multiply fragmented distributions (older craters) have negative slopes >2 (see also Melosh 1989). Further processing and work showed that these initial images had relatively high sun angle (with smaller shadows) and image noise, which hampered the detection of smaller rocks.

A follow-up pilot study was conducted using HiRISE frames with improved image quality (less noise) and higher solar incidence angles (larger rock shadows). These images also underwent noise reduction processing by the HiRISE team at the University of Arizona (Sutton et al. 2015; McEwen et al. 2016), which also helped DEM production (Howington-Kraus et al. 2015). The second pilot study encompassed fifty-nine, 150 m square tiles in seven sample areas surrounding a variety of rocky ejecta craters in the smooth terrain. The results indicate a significantly improved correlation between human and automated rock counts (>90 % are within 2 % of the derived rock abundance) and the measurement of far more small rocks, which steepened the distributions. Further examination of power law rock distributions showed difficulties in limiting the maximum and minimum rock sizes and theoretical fragmentation distributions based on negative binomial statistics (see Sect. 7.10) showed that the expected distribution has fewer rocks at large diameter (and small diameter) than a power law and more closely resembled the Rosin Rammler, Weibull, and exponential distributions that have been used previously to describe rock populations (Rosin and Rammler 1933; Gilvarry 1961; Gilvarry and Bergstrom 1961; Wohletz et al. 1989; Brown and Wohletz 1995; Golombek and Rapp 1997; Golombek et al. 2003b, 2008b, 2012b; Craddock and Golombek 2016). Further, the exponential models developed by Golombek and Rapp (1997) are based on the area covered by rocks (or diameter squared), which results in a less curved distribution when translated into cumulative number distributions on a log-log plot than a true exponential (e.g., Golombek et al. 2003b, 2008b, 2012b; Craddock and Golombek 2016) that can be fit more readily to power law distributions over a limited diameter range (e.g., Grant et al. 2006; Russell et al. 2013). In addition, human observers in the pilot studies filtered out many large detections that are not rocks (mostly shadows from steep sided hills and scarps), such that automated fits of the model exponential distributions to just the rocks in the 1.5–2.25 m size range using the same process used for MSL (Golombek et al. 2012b), accurately fit the observed rock distributions (Fig. 16). The derived model exponential distributions and all detections >2.25 m (extra strikes) were then used to create maps of the landing sites using the same method as MSL (Golombek et al. 2012b).

Rock maps and data products produced include the diameter, height and location of every detection, maps of the total number of rocks in 150 m by 150 m tiles, summary SFDs of rocks within each tile, best fit CFA model distribution maps from rocks 1.5–2.25 m diameter in each tile, and the number, size and location of extra strikes ($D > 2.25$ m) in each tile. Maps of the total number of rocks in 150 m tiles (Fig. 17) show that rocks in the smooth

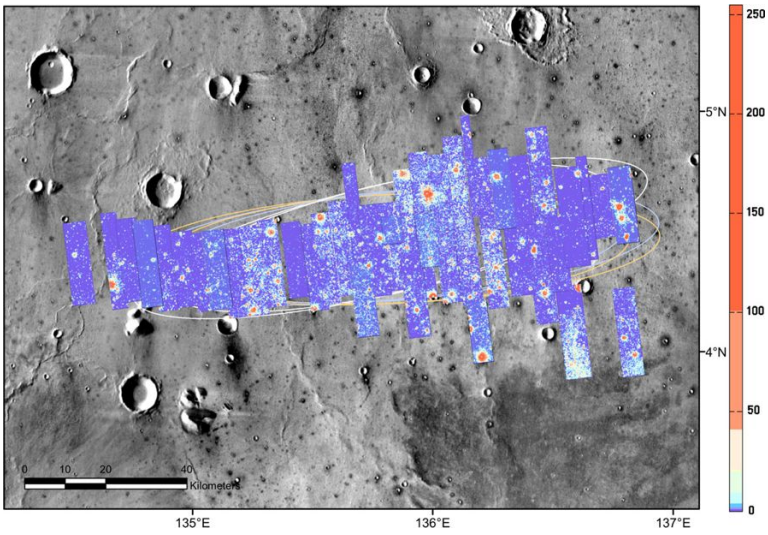

Fig. 17 Total number of rocks in 150 m tiles for the E9 landing ellipses (scale bar at *right*). The total number of rocks varies from zero in background smooth terrain to >250 rocks per 150 m tile in rocky ejecta around impact craters. Note scale color stretch is not linear. Ellipses are as described in Fig. 10 for the 2018 launch opportunity. Coverage shown is as of September 2016. Background is the THEMIS daytime mosaic in which dark halo craters have higher thermal inertia from rocky ejecta

terrain are concentrated around rocky ejecta craters (Sect. 7.9). The smooth terrain away from rocky ejecta craters are effectively devoid of detected rocks with zero to only a few detections in 150 m tiles. Adjacent to fresh rocky ejecta craters the total number of rocks in 150 m tiles spikes to >250; more degraded rocky ejecta craters have lower concentrations of rocks.

Rock abundance in 150 m tiles, which is the CFA covered by all rocks from the fit to the exponential model (Fig. 18), varied in different terrain types from an average of 2.5 % in smooth terrain to 36 % in rocky crater rims from a sample of 10 images from DEMs that sample the final four ellipses. Average rock abundance in the etched terrain (5.6 %) is about twice as high as that in the smooth terrain, with gradational etched (3.8 %) and dark terrain (3.2 %) in between. Rock density and rock abundance maps of the smooth terrain showed a large fraction of the surface away from rocky ejecta craters is essentially rock free. Rock abundance in smooth terrain in ellipses E5 (4 HiRISE), E8 (7 HiRISE) and E9 (14 HiRISE) at the time that the E9 ellipse was selected by the project (May 2015) showed that ellipse E9 has an average rock abundance of 1.5 % (Fig. 18), about half of the average rock abundance in the other two ellipses. As for the total number of rocks in 150 m tiles, rock abundance in ellipse E9 is strongly concentrated around rocky ejecta craters (up to 36 %) with most smooth terrain having zero rock abundance. The average rock abundance of the 150 m tiles in the E9 ellipse is 1.2 % ± 3.2 % and the area that exceeds 10 % rock abundance is about 0.8 %. The extra strikes in 150 m tiles are also strongly concentrated around rocky ejecta craters and covers 0.015 % area in ellipse E9. The measured height-diameter ratio of the rocks averages ~0.5, which is assumed in the simulations. The average rock abundance used for the simulations is 6.3 % ± 1.3 %, in which one rock 1.5–2.25 m diameter is assumed in all 150 m tiles (Sect. 8.1.3), which yields a 6 % rock abundance for all tiles with no rocks detected in this size range (Golombek et al. 2012b).

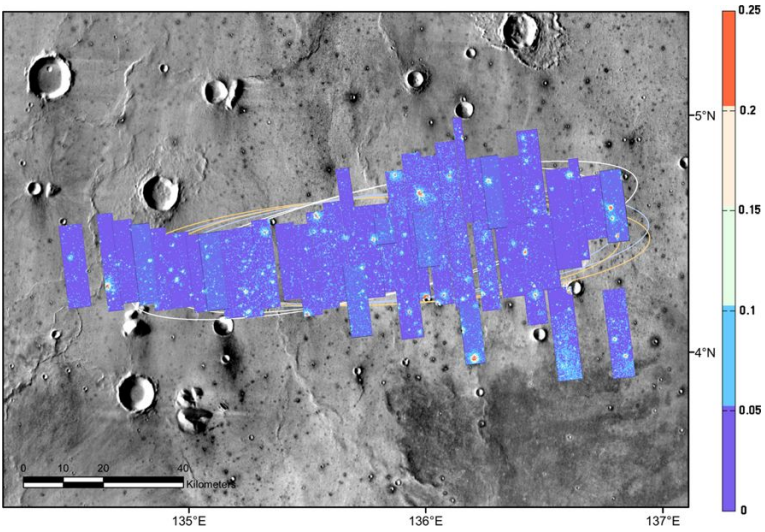

Fig. 18 Rock abundance, or the cumulative fractional area covered by all rocks (*scale bar at right*) from the fit of rocks between 1.5 m and 2.25 m diameter to the exponential model in 150 m tiles for the E9 ellipses. Rock abundance is strongly concentrated around rocky ejecta craters (up to 36 %) with most smooth terrain having zero rock abundance. Ellipses are as described in Fig. 10 for the 2018 launch opportunity. Coverage shown is as of September 2016. Background is the THEMIS daytime mosaic in which dark halo craters have higher thermal inertia from rocky ejecta

The overlapping image areas in which the rock abundance was measured and fit to a model cumulative fractional area provide an estimate of the repeatability of the method. Because HiRISE images were independently processed (with no consideration of adjacent images) using the method described in Golombek et al. (2012b) (including: blind deconvolution, sectioning the images for shadow enhancement, shadow segmentation, fitting ellipses to shadows and cylinders to rocks to derive rock height and diameter, elimination of non-rocks and fitting to model size-frequency distributions for rocks 1.5–2.25 m in diameter), the comparison of overlapping area can be considered as a blind test of the reproducibility. For 49 HiRISE images covering 4,800 km^2 in which rock maps were created of the E9 landing site, there are 73 unique overlapping areas of 0.2–38 km^2 for a total of 800 km^2. For these overlapping areas, the average rock abundances of the 150 m tiles were nearly identical between the images with 91 % and 99 % of the areas differing by less than 0.2 % and 0.3 %, respectively. Comparison of the difference in the best fit model CFA for individual overlapping 150 m tiles shows that over 82 % of the estimates are within 1 % and over 94 % are within 2 % of the derived rock abundance. Because the difference in the probability of failure from landing on a potentially hazardous rock is only 0.4–0.8 % for a difference of 1 % rock abundance for these sites (see Sect. 8.1.3), the 18 % of bins with different rock abundances will have no appreciable impact on the simulation results and the reproducibility of the estimated rock abundance is excellent.

Rock abundance at the InSight landing site is lower than previous landing sites (Table 7), with the possible exception of Phoenix and Meridiani Planum. The InSight ellipse E9 has 1.2 % rock abundance averaged in 150 m tiles and is similar to the PHX landing site (Heet et al. 2009; Golombek et al. 2012b). If all rocks in the landing site are plotted on a single SFD plot, rocks 1.5–2.25 m diameter derive an average rock abundance of 5.7 % (see Sect. 7.10), which is closest to the rock abundance at the Spirit landing site (Golombek et al.

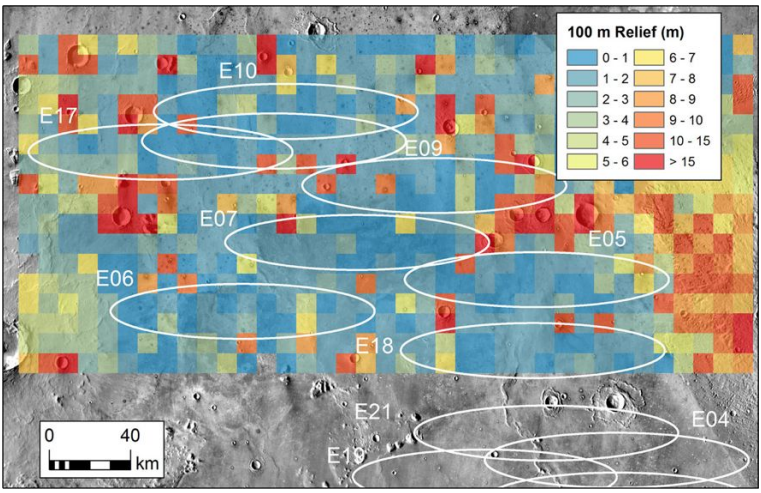

Fig. 19 Map of the Allen deviation or relief at 100 m scale extrapolated using the Hurst exponent from 1.2 km to 300 m scale relief along MOLA altimetry shots in 12 km bins (e.g., Anderson et al. 2003). Note low relief of the plains. Background is THEMIS daytime mosaic

2005, 2006). Average rock abundance determined in these ways for ellipse E9 also compare favorably to low rock abundance estimates from thermal differencing of IRTM and TES data. IRTM rock abundance is 4 % and 9 % for pixels of ~60 km (Christensen 1986) and TES rock abundance average 4 % (1 %–7 %) for pixels of ~7.5 km (Nowicki and Christensen 2007) in ellipse E9.

7.6 Slopes and Relief

7.6.1 Slopes at ~100 m Length Scale

Slopes at approximately 100 m length scale are important for radar tracking of the surface during descent with the requirement that <1 % of the surface exceeds 15° at 84 m length scale. Initially (before DEMs were produced) MOLA data were used to estimate the slope at this length scale. However, because individual MOLA elevation shot points are spaced ~300 m along track (Smith et al. 2001b), no direct measure of 100 m slopes could be made with MOLA data. To estimate relief and slopes at this scale, the MOLA data were extrapolated from 0.3 to 1.2 km length scale to 100 m using the Allen deviation and Hurst exponent, assuming self-affine statistics, as has been done for other landing sites (Anderson et al. 2003). Root Mean Square (RMS) slopes and relief (Allen deviation) extrapolated to 100 m length scale are ≤2° and ≤4 m, respectively, for the final four ellipses. This is smoother than all the other landing sites except VL2, which is comparable (Table 7). Some of the other ellipses that were eliminated had higher RMS slope (>4°) and relief (>8 m). Maps of RMS slope and relief in 12 km bins show the smooth plains to be exceptionally smooth and flat at this scale with higher values over large craters and highland monadnocks poking through the plains (Fig. 19). The highest values correspond to areas with slopes greater than 15° in MOLA along-track elevations spaced at ~300 m (e.g., Fig. 6).

MOLA pulse spread is a measure of the RMS relief within the ~75 m diameter laser spot after removal of regional slopes (Neumann et al. 2003; Zuber et al. 1992; Smith et al. 2001b).

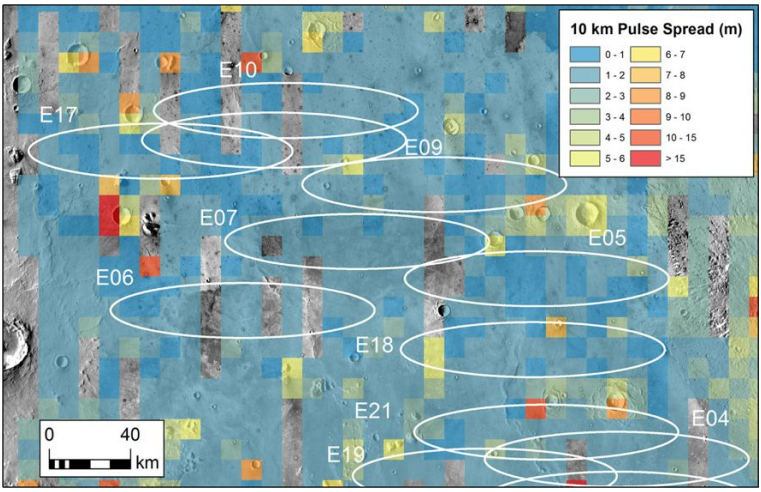

Fig. 20 Map of MOLA pulse spread (slope corrected from Neumann et al. 2003), which is a measure of the RMS relief within the ∼75 m diameter laser spot, of the InSight landing sites. Note exceptionally low pulse spread of the smooth plains without large craters and the higher relief over large craters and monadnocks. Notice the similarity with the map of Allen deviation at roughly the same length scale in Fig. 19. Background is THEMIS daytime mosaic

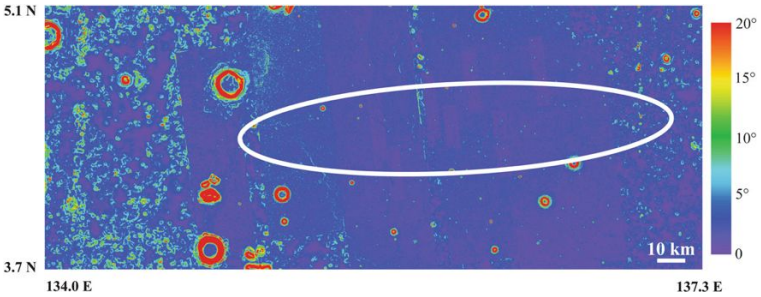

Fig. 21 Hierarchically co-registered slope mosaic of the HRSC DEM overlain by five CTX DEMs and 7 HiRISE DEMs generated for ellipse E9 for EDL simulations. Mosaic of the 20 m length scale slope is in an equirectangular projection with a center latitude of 0°, a longitude domain of 180° at a scale of 20 m/pixel. Note the noise in the HRSC topography in the smooth areas to the west, where CTX DEMs do not exist. HiRISE DEMs can be distinguished by their narrow width and finer scale topographic variations

Garvin et al. (1999) suggest RMS pulse spreads of <2 m have relief of <10 m over the shot point. Relief of 10 m over 75 m length corresponds to slopes of $<8°$, which are less than the slope constraint at this scale. The slope-corrected pulse spread data of Neumann et al. (2003) maps are generally similar to the extrapolated 100 m slope and relief maps, with most smooth terrain having pulse spreads of less than 2 m with higher values over large craters and monadnocks (Fig. 20). Average MOLA pulse spread of the final four ellipses are all ≤ 1.2 m, which are less than all other landing sites except Meridiani Planum and VL2, which are comparable (Table 7).

We also investigated slopes on an 84 m baseline in the E9 ellipse region with available higher-resolution DEM elevation data (Fig. 21). Unfortunately, the HRSC mosaic was found to have noise at this scale in bland, flat areas, which created artificially high slope values.

Table 8 Adirectional 1 m slope statistics of terrains from HiRISE DEMs

Terrain type	RMS slope°	% Area >15°
Smooth Terrain	3.9	0.4
Ridged Terrain	3.2	0.3
Dense Crater Swarms	4.3	0.5
Gradational Etched Terrain	4.2	0.5
Dark Terrain	4.7	0.7
Etched Terrain	5.2	0.8
Crater Ejecta Terrain	7.0	4.2
Crater Rim Terrain	24.5	59.5

The CTX DEMs were free of such noise, so we considered the resulting slopes to be more reliable, although those DEMs do not cover the entire bounding box for which hazard maps were created (Fig. 21). The percentage area in the bounding box with slopes greater than 15° is 1.52 % in the HRSC data, and 0.66 % in the CTX data, with the difference between the two data sets likely being due to noise in the HRSC DEMs.

In summary, all four final landing sites considered met the requirement for <15° slopes at ~100 m length scales, except for isolated small areas of steep crater walls and highland scarps. Finally, although InSight has no slope or relief constraints at around the 1 km length scale, the average 900 m bidirectional MOLA relief (a criterion important for MSL) is a factor of 2–4 lower at the InSight final four landing sites compared to final MSL sites, and the average 1.2 km bidirectional MOLA slope (important for MPF) is among the lowest of all of the other landing sites (Table 7).

7.6.2 Slopes at 1–5 m length scale

DEMs Ten HiRISE DEMs were generated for the final four ellipses (E17, E9, E8, and E5) to sample the major terrain types (Fig. 8). Slopes were determined for all major terrains (Table 8), with a significant sampling of the smooth terrain, which is the most abundant unit in the landing site region. For the certification of ellipse E9, four additional HiRISE DEMs were prepared (Fig. 10). The pre-processing steps (calibration, dejittering) and DEM generation process used are similar to that used for MSL (Golombek et al. 2012a), and are described in detail in Fergason et al. (2016, this issue). Visual inspection of the DEMs and slope images, and the evaluation of height contours derived from the DEM and superimposed onto image data, indicate that there are minimal artifacts in these DEMs and the elevation values correspond well with the observed terrain. In addition, the expected vertical precision (EP) was calculated for HiRISE DEMs following Kirk et al. (2003; 2008; 2011; 2016). All HiRISE DEMs have an expected vertical precision of 0.1 to 0.2 meters, similar to those derived for the Phoenix landing site (Kirk et al. 2008) and for MSL (Golombek et al. 2012a).

Ellipse E9 is primarily composed of smooth terrain with smaller amounts of ridged terrain, ejecta terrain, highland scarps and dense crater swarms. The smooth terrain has RMS slopes at 1 m baselines ranging from 3.2° to 4.6°, which is consistent with slopes for this unit in other areas. The crater ejecta terrain in this region has a higher RMS slope at 1 m baselines of 7.0°. This unit covers a small portion of the ellipse and is associated with a single, large crater that falls outside of the landing site ellipse. The dense crater swarms and the ridged terrain units have RMS slopes at 1 m baselines of 4.3° and 3.2°, respectively. Ellipse E17 considerably overlaps ellipse E9 and it has similar slopes at the 1 m scale.

Ellipse E8, located southeast of ellipse E9 and northwest of ellipse E5, has five HiRISE DEMs within the ellipse. This ellipse contains the most terrain types, including smooth terrain, crater ejecta terrain, dark terrain, etched terrain, dense crater swarms, and crater rim terrain. Not surprisingly, the crater rim terrain has the highest RMS slopes at 1 m baselines of 9.0° to 9.8°. The crater ejecta terrain has the next highest RMS slopes at 1 m baselines of 6.7° to 7.8°. This RMS slope is higher than that for the entire unit sampled and is attributed to some of the largest craters in the ellipses. The final three terrains all have similar slopes at 1 m baselines: the etched terrain has RMS slopes of 4.6° to 5.0°, the dark terrain has an RMS slope of 4.7°, the dense crater swarms has an RMS slope of 4.5°, and smooth terrain has RMS slopes of 4.0° to 4.6°.

Four HiRISE DEMs were generated within ellipse E5 (Fig. 8). These DEMs primarily fell within the western portion of the ellipse in order to sample the diverse terrains located within that region, including smooth terrain, crater ejecta terrain, dark terrain, dense crater swarms, and gradational etched. At 1 m baselines, the crater ejecta terrain has the highest slopes in this ellipse, with RMS slopes of 5.4° to 5.7°. All other terrain types had comparable 1 m baseline RMS slopes ranging from 4° to 4.5°. The smooth terrain consistently had a smoother surface and the majority of slopes in the ellipse are generally low. There were occasional slopes that approached 20° at 1 and 5 m baselines, but those were isolated to the edges of crater rims and represented a very small percentage of the ellipse.

Photoclinometry Photoclinometry, or shape-from-shading, is the general technique of obtaining slopes or topography from the brightness values in an image. Beyer (2016, this issue) used the same technique and algorithm used by Beyer et al. (2003) and Beyer and Kirk (2012) for previous landers for the InSight landing site to provide bidirectional slope measurements. The technique only provides slopes measured along a single direction (bidirectional slopes), which are less steep than the true adirectional slopes (the maximum slope in any direction) by a factor of $\sqrt{2}$. Because the InSight ellipse is in a moderately dusty region with a thin layer of bright dust (DCI of 0.94; Ruff and Christensen 2002), albedo variations are minimal, thereby reducing a major source of uncertainty in deriving slope from shading. To constrain the other main source of uncertainty in photoclinometry, the atmospheric haze estimate was tuned in individual images to match the slopes derived in the DEMs at the same location (e.g., Beyer and Kirk 2012). Images between the DEMs had their haze parameter tuned to an interpolated value from adjacent images so that the resulting RMS slopes were consistent across the ellipse and with those of the DEMs (Beyer, 2016, this issue). This method forced the bulk statistics of the photoclinometry derived slopes to be identical to bidirectional slopes measured from the DEM. In this way, Beyer (2016, this issue) determined that 97 % of all slopes measured in ellipse E9 were less than 5°, and 99.4 % of all slopes measured were less than 10°, indicating that the landing site is remarkably smooth at the two meter scale.

Discussion Early photoclinometry and DEM derived slopes at 1–5 m length scale indicated that the smooth terrain had the lowest slope and the least area that exceeds 15° (Table 8). These results contributed to the first landing site downselection to the four northern ellipses (E5, E8, E9, and E17) that are dominated by the smooth terrain. By the time of the second landing downselection and subsequent selection of ellipse E9, 14 DEMs and over 40 photoclinometry slope maps yielded consistent bulk slope statistics for the final three ellipses (E17 was combined into E9 because of their overlap). RMS 1 m adirectional DEM slopes are 4.3°, 5.7° and 3.9° and 1 m photoclinometry bidirectional RMS slopes are 2.8°, 3.5° and 2.7° for ellipses E5, E8, and E9, respectively. Adjusting the bidirectional RMS

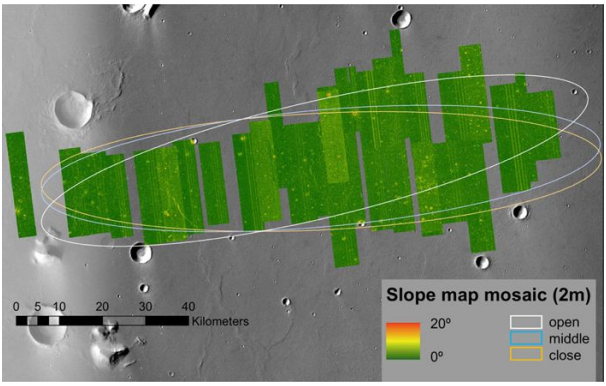

Fig. 22 Two-meter length scale slope mosaic of ellipse E9 prepared from combined HiRISE DEMs and photoclinometry. About 0.1 % of the surface exceeds 15° slope, thereby satisfying the engineering constraint of <1 % of the area exceeding 15°. This map was binned into individual quantized slope increments of 5° for entry, descent and landing simulations. Background is the HRSC orthoimage

slopes to adirectional RMS slopes yields 4.0°, 4.9° and 3.8°, respectively, which agrees with the DEM slopes, and suggests that the haze tuning did not introduce any large errors and that the larger photoclinometry sample is similar to the smaller DEM sample. The fractional area that exceeds 15° at 1 m scale is 0.5 %, 0.7 % and 0.3 % in the DEMs and 0.8 %, 1.6 % and 0.9 % in the photoclinometry for ellipses E5, E8, and E9, respectively. The smooth terrain also has the lowest RMS slope in ellipse E9 compared with the smooth terrain in the other ellipses. These results confirm that ellipse E9 is the smoothest of the three and has the least area that exceeds 15 %. By the time of final site certification, the six DEMs and 42 photoclinometry maps were made into a single 2 m slope mosaic for simulations (Fig. 22), which showed ∼0.1 % of the surface is greater than 15°, which meets the slope constraint of <1 % area over 15°.

The photoclinometry data from ellipse E9 were also used to create a plot of the bidirectional RMS slope versus baseline length from 25 cm (the native resolution of HiRISE) to 100 m (Fig. 23). The bidirectional RMS slopes at 25 cm average just under 3° and decrease logarithmically to <1° at 100 m. The bidirectional RMS slope at 100 m of <1° compares favorably with that derived by extrapolating MOLA data (also bidirectional) to 100 m (see Sect. 7.6.1), indicating the surface meets the slope constraint at 84 m. Furthermore the RMS slope at 25 cm is only 20–25 % greater than that at 2 m. This suggests that the area that exceeds 15° at 25 cm is only modestly greater than the 0.1 % fraction at 2 m, which indicates that only a fraction of 1 % of the surface exceeds the 15° limit to successfully deploy the instruments.

The InSight landing site is among the smoothest surfaces investigated for landing spacecraft on Mars. Figure 24 plots the RMS slope at 5 m length scale versus the percent area that exceeds 15° for the landing sites that have quantitative slope information from MOC and HiRISE stereogrammetry and photoclinometry (Kirk et al. 2003, 2008; Golombek et al. 2012a; Beyer and Kirk 2012). At this scale, the InSight landing site has an RMS slope of 2°–3° and <0.2 % of the surface with a slope >15°, and is smoother than all other landing sites with the possible exception of the Opportunity landing site at Meridiani Planum or the PHX landing site in the northern plains. For comparison, the PHX and Opportunity sites have 5 m RMS slopes of ∼2° and comparable area >15°, with VL2 and Spirit landing sites having 5 m RMS slopes of ∼4° and ∼1 % of the surface >15°, and VL1 and Pathfinder having 5 m RMS slopes ∼5° and ∼2 % of the surface >15°.

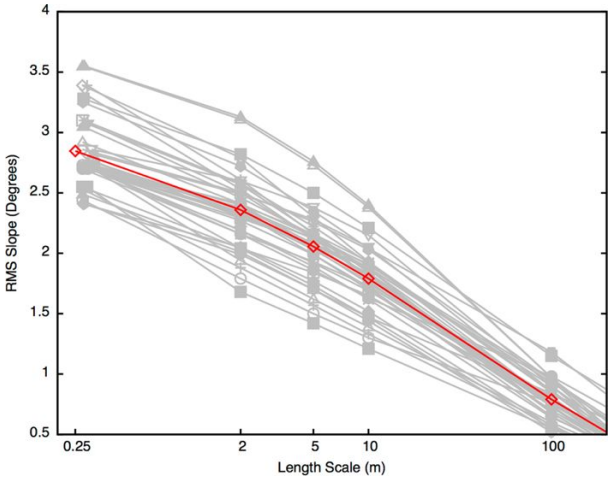

Fig. 23 Bidirectional RMS slope versus baseline length of HiRISE images in ellipse E9 from photoclinometry (*red* is the average). RMS slope varies with baseline length from $<1°$ at 100 m to 2.5–3.5° at 25 cm. The photoclinometry derived RMS slope at 100 m length scale compares favorably with MOLA extrapolated RMS slopes at the same scale (see Sect. 7.6.1). In addition, RMS slopes at 25 cm are only 20–25 % greater than that at 2 m, suggesting that only a fraction of 1 % of the surface exceeds the 15° limit to successfully deploy the instruments. Bidirectional slopes are produced by averaging the brightness values over each length scale and then running the photoclinometry algorithm on the downsampled image (Beyer et al. 2016). Bidirectional slopes are $\sqrt{2}$ lower than adirectional slopes

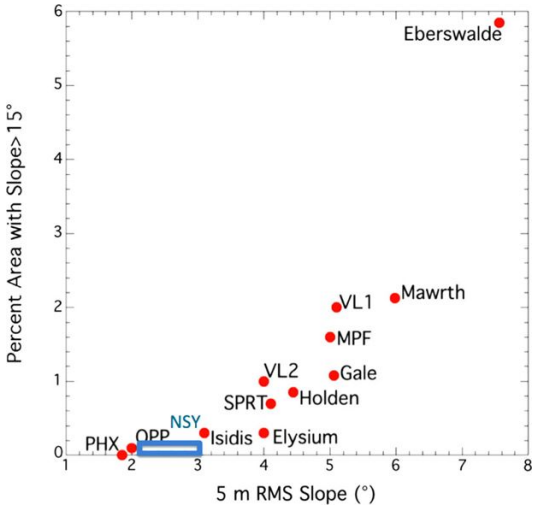

Fig. 24 Plot of the 5 m length scale RMS slope versus the percent area with slopes $>15°$ for the landing sites that have quantitative slope information from MOC and HiRISE stereogrammetry and photoclinometry (Kirk et al. 2003, 2008; Golombek et al. 2012a; Beyer and Kirk 2012). At this scale the InSight landing site has an RMS slope of 2°–3° and <0.2 % of the surface with a slope $>15°$ and is smoother than all other landing sites with the possible exception of the Opportunity landing site at Meridiani Planum or the Phoenix landing site in the northern plains

7.7 Corinto Secondaries

During the acquisition of HiRISE images of the original 16 ellipses after InSight was selected as the next Discovery Program mission (August 2012), it was noticed that virtually all of the ellipses had a population of small craters. These were interpreted to be secondaries based on their small size, occasional herringbone pattern, and clustering in rays. The first HiRISE image of ellipse E2 (shown in Fig. 5) (ESP_030972_1835) showed a surface

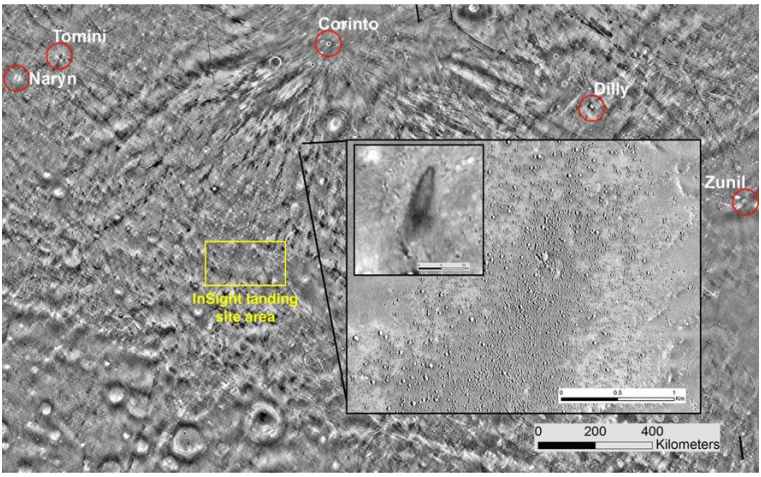

Fig. 25 THEMIS nighttime thermal image mosaic showing dark rays with low thermal inertia emanating from Corinto crater about 800 km to the north-northeast of the landing sites. Several other young rayed craters identified by Tornabene et al. (2006) and Hartmann et al. (2010) are marked with *red circles*. High-resolution imaging in the InSight landing site area (*yellow rectangle*) led to the discovery and mapping of this extensive system of secondary rays, which dominates over other rayed craters in this part of Mars. The *inset* shows an individual THEMIS nighttime dark ray, with the HiRISE image PSP_006512_1910 showing the dark ray is composed of dense secondary craters

saturated with craters 1–20 m diameter that covered almost half of the surface with distinctive bright ejecta. Mapping some of the larger craters in CTX images and their herringbone pattern indicated the craters should extend to the north into ellipse E3. The acquisition of HiRISE image (ESP_031183_1845) two weeks later confirmed that a similarly dense swarm of craters extended through the center of ellipse E3. Examination of nighttime THEMIS images showed that dark (very low thermal inertia) streaks trending northeast (Fig. 25) extended through many of the ellipses. These dark streaks were traced back to a fresh rayed crater called Corinto located at 141.72°E, 16.95°N approximately 700 km northeast of the landing site region. Although this 13.9 km crater had been identified earlier (McEwen et al. 2010), the full extent of the rays emanating from it had not been recognized. The low thermal inertia rays in THEMIS nighttime images and existing HiRISE images were mapped outside the landing site region and showed they were all composed of dense swarms of secondary craters (Golombek et al. 2014b) (Figs. 25 and 26). In the nighttime thermal images, dark rays from Corinto (and the other four young rayed craters in the region) dominate this portion of Mars (Fig. 25). They extend 1500–2000 km to the south, covering a nearly 180° crescent. Corinto may have produced more secondaries than any other fresh rayed crater (Bloom et al. 2014), including Zunil (McEwen et al. 2005; Tornabene et al. 2006; Preblich et al. 2007). Finally, mapping of secondaries from Corinto constrains its age (Golombek et al. 2014b) to be younger than Cerberus lavas in the Western Lava Basin dated 2.8 ± 0.5 Ma (Vaucher et al. 2009), but older than Zunil estimated to be 0.1–1 Ma (Hartmann 2005).

Mapping in the nighttime THEMIS mosaic showed that over half of the 22 ellipses identified by the first downselection had northeast-trending dark streaks. Existing HiRISE images of these streaks showed that every dark streak was composed of dense secondary craters. Because of their occurrence over so many ellipses and their high density within the streaks, the question of whether or not they would be hazardous to InSight was investigated. Fur-

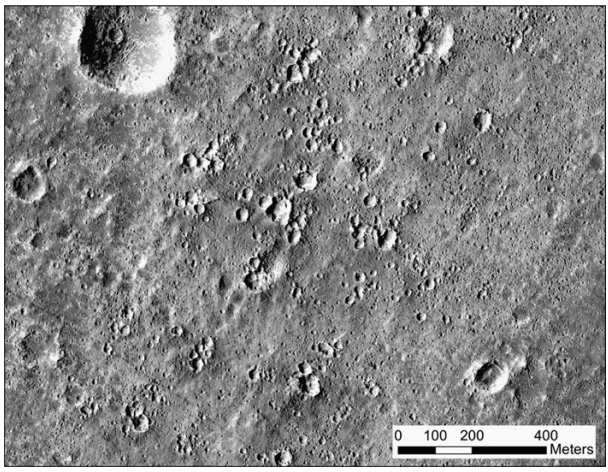

Fig. 26 Portion of dense ray of secondary craters from Corinto crater in the InSight landing site region. This is part of a low thermal inertia ray in ellipse E5 that points towards Corinto to the north-northeast. Corinto secondary craters in this region have a distinctive light toned ejecta and overlie eolian bedforms (*upper left*). Note thin, dark dust devil tracks trending to the northwest, which are common on the smooth plains. This is a portion of HiRISE image ESP_033583_1835 located at 3.39°N, 138.16°E

thermore, because significant portions of ellipses E1–E3 are covered by one of these rays, the viability of these ellipses depended on the hazards associated with them. Prior to the formation of the Council of Terrains and the production of DEMs and slope maps, an idealized crater morphometry was assumed. Previous work on secondary craters showed that their initial depth/diameter ratios (d/D) are ~0.1 (e.g., Pike and Wilhelms 1978; Schultz and Singer 1980; McEwen et al. 2005), about half as deep as primary craters (Pike 1980; Wood and Andersson 1978). Because many small, fresh lunar craters have flat floors and constant wall slopes (Wood and Andersson 1978) that then appear to degrade into bowl shaped craters (Ravine and Grieve 1986), we assumed a flat-floored geometry with $d/D = 0.1$. Additionally, this geometry produces the steepest wall slopes for a given d/D that are consistent with the morphometric measurements and thus are the most hazardous for a lander, so this model represents a conservative estimate of the hazard associated with these secondaries. In this idealized geometry, we assumed the wall slope is $D/4$ wide, and the diameter of the flat floor is $D/2$. For this model, craters smaller than 4 m diameter will not have slopes $\geq 15°$ over the diameter of the lander (2.73 m) and so should not be hazardous. In addition, a crater must be >11 m diameter to have a scarp wider than the diameter of the lander. An engineering model of the lander was tested for tilts of >15° and solar array clearance for craters of this geometry with diameters of 1–40 m. Results showed that failure increased steeply by area of the crater, from 0 % for craters 4 m diameter to around 50 % for craters of 7 m diameter and then more slowly to 75 % for craters ≥20 m diameter.

The overall risk to the spacecraft was thus estimated by measuring the areal coverage of secondary craters in five different secondary density classifications: 1) low density (0.5 % area covered by Corinto secondary craters); 2) medium-low secondary density (~0.6 % area covered by secondaries); 3) medium density (~1.6 % area covered by secondaries); 4) medium-high secondary density (~5.1 % area covered by secondaries); and 5) high secondary density (~18.7 % area covered by secondaries). The average area covered by craters in each secondary density category was measured in several HiRISE image samples and those averages were applied to the remaining areas of the images with the same estimated densities in 2.5 km by 2.5 km samples (Fig. 27). The total area covered by secondaries in each ellipse was then calculated using the categorizations. The resulting average area covered by secondaries for each ellipse are: E5, 1.4 %; E8, 1.2 %; and E9, 1.5 %. These are extremely small areas covered by secondaries, with very small differences between them

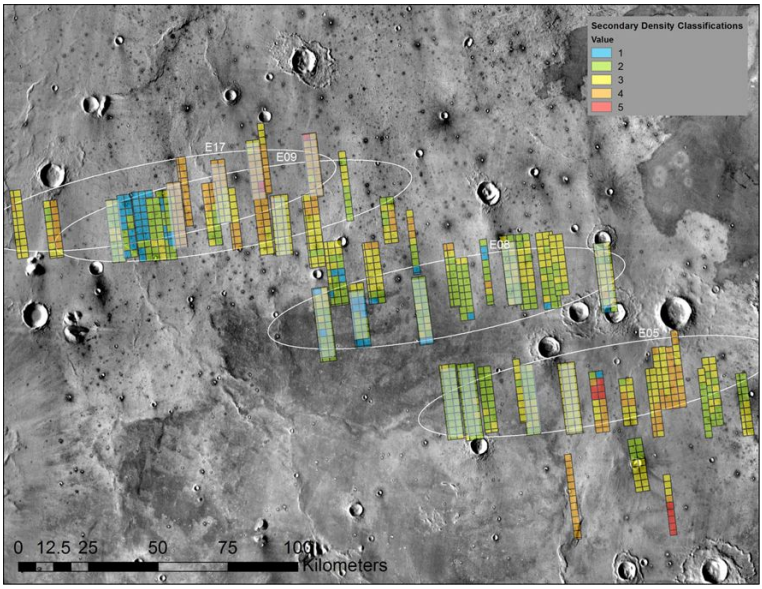

Fig. 27 Map of the classification of 2.5 km by 2.5 km samples of HiRISE images in the InSight landing site area according to the density of Corinto secondary craters. *Blue*: (1) low density (∼0.5 % of the area covered by secondary craters); *Green*: (2) medium-low density (∼0.6 % area covered by secondaries); *Yellow*: (3) medium density (∼1.6 % area covered by secondaries); *Orange*: (4) medium-high density (∼5.1 % area covered by secondaries); and *Red*: (5) high density (∼18.7 % area covered by secondaries). Background is THEMIS daytime thermal image mosaic

(0.2–0.3 %). These areal coverage fractions were used to estimate the probability of failure due to secondaries in each ellipse, and the results were reported at the second landing site workshop. Results indicated failure rates that varied from 0.5 % to 1.2 %.

The secondary density classifications were also used to examine the cumulative fractional slope distributions using photoclinometry and stereogrammetry within higher secondary density categorizations (high, medium-high, and medium). The DEMs did show small differences for slopes less than 5°. The photoclinometry showed higher slopes than DEMs, as expected, given that photoclinometry slopes are at 25 cm baseline and DEMs slopes at 1 m. Among the photoclinometry results, the density classification did correlate with the bulk slope statistics for very small slopes <5°. However, above 5° there was very little difference between the secondary density classifications. Additionally, the high-density secondary classification samples show the same slope distribution as the bulk DEM slope statistics over all smooth terrain. The percentages of area with slopes greater than 15° for the different secondary classifications were 0.18 % (high); 0.15 % (medium-high); and 0.22 % (medium) based on 1 m DEMs and 0.82 % (high); 0.62 % (medium-high); and 0.59 % (medium) based on 25 cm photoclinometry.

HiRISE DEMs and photoclinometry maps produced by the Council of Terrains were also subsequently used to evaluate the d/D ratios, the shapes, and the interior wall slopes of secondary craters. To evaluate the d/D ratio of secondary craters, an automated script was developed along with a manual method. The manual method involved taking two DEM transects each over 97 different craters located in different areas across the landing site region. In each profile, the highest points in the elevation profiles were manually identified and used as the location of the rim; their average elevation was taken as the rim height, thus

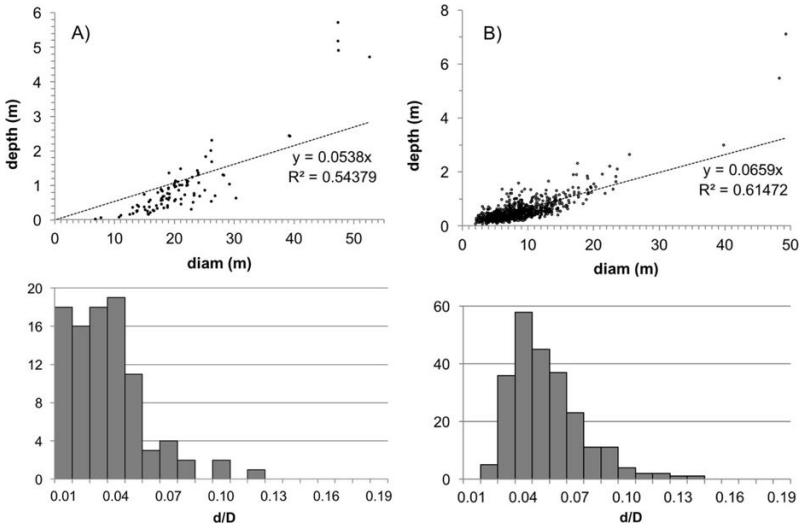

Fig. 28 Depth/diameter measurements of Corinto secondary craters average ∼0.05. Diameter plotted versus depth with least-squares fit (*top*) and histograms of d/D values (*bottom*) of Corinto secondaries as measured using manual DEM profiles (*left*) and automated script as described in the text (*right*)

reducing errors due to regional slopes. The difference between the rim height and the lowest point within the crater was taken as the depth. Measurements were restricted to craters that could be confidently resolved in the DEM (>∼10 m diameter). The results of this method gave an average d/D of 0.04 (Fig. 28).

In order to obtain a larger sample with many more craters, an automated script was created in ArcGIS for measured crater diameters. Crater outlines were buffered outward radially by 3 m. Within that area, the difference between the highest and lowest points was taken to be the depth. There are obvious possible issues with this method that could yield erroneous measurements, including regional slopes and irregular crater shapes. However, it was an efficient way to gather statistics on 835 of these craters, and the results could be calibrated using the manual measurements described above. Because the vertical precision of the DEMs used is ∼0.1–0.2 m (Fergason et al. 2016, this issue), we excluded craters shallower than <0.4–0.6 m, corresponding to craters with diameters <∼10 m, leaving 236. The results contained substantial scatter, but show an average $d/D \sim 0.06$ with a mode ∼0.04 (Fig. 28). This average was slightly higher than that using the manual method, so it was concluded that the script yielded a conservative estimate of the d/D of these craters overall.

Slopes calculated from the 97 manual transects over both 1 m and 2 m baselines had a mode of only ∼1° and the maximum slope within each crater averaged 5°. Furthermore, it was found that these elevation profiles do not show flat floors. Instead, the craters were a mix of parabolic and conical in cross section. These shapes would be expected to have lower slopes than craters with flat floors because the relief is accommodated over longer baselines. Using these as two end-member shape models, the theoretical slopes within a crater of a given d/D for each shape were calculated (Fig. 29). The results show that slopes are below 5° for conical craters and below ∼11° for parabolic craters when $d/D = 0.05$.

The Corinto secondaries were also examined at a higher resolution in the photoclinometry data. Signed (not absolute value) slopes were used to derive relative elevations by integrating the slopes across the crater. Results were compared to DEM elevations (1 m elevation

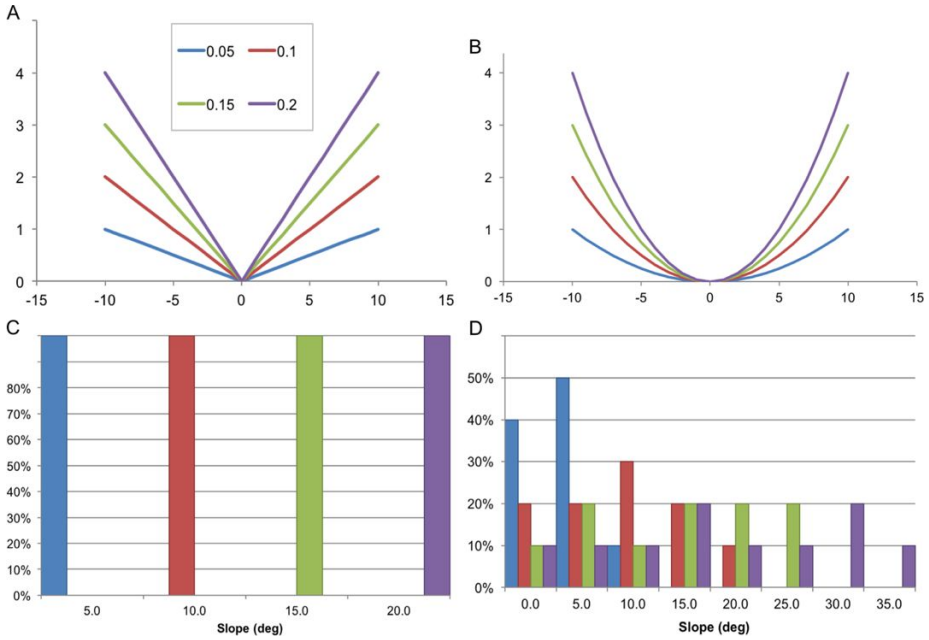

Fig. 29 Theoretical shape models and the resulting slopes for conical and parabolic shaped craters as observed in DEMs. Cross-sections of conical- (**A**) and parabolic-shaped (**B**) craters with $d/D = 0.05$, 0.10, 0.15, and 0.20 with dimensionless axes of height and length. Histograms of the slopes in the theoretical cross-sections, conical (**C**) and parabolic (**D**). Note that slopes for conical and parabolic shape craters with d/D of 0.05 are $<6°$ and $<11°$, respectively, and thus less than the 15° engineering constraint

postings) and 1 m slopes (Fig. 30). A qualitative comparison between the photoclinometry data and DEM-derived slopes showed that photoclinometry can resolve smaller craters than DEMs (<10 m diameter), as expected. The photoclinometry also shows steeper slopes over the same areas, again as expected. To quantify this difference, profiles over selected secondaries were compared. Using methods as described above to take profiles and measure the d/D, the average d/D for five craters was 0.052 ± 0.002 using photoclinometry, compared to 0.030 ± 0.004 using DEMs. Thus the photoclinometry yielded higher d/D than DEMs (as expected due to the higher resolution). However, the d/D values are still all very low (maximum 0.06). The shapes of the profiles were also found to be conical and parabolic, just as with the DEM profiles. The slopes along those profiles showed similar results with a larger percentage with higher slopes in photoclinometry (6.9 % area >10° and 0.4 % area >15°) than DEMs (0.6 % area >10° and 0 % area >15°), as expected. However, the percentage of the profiles with high slopes is very small, even though they sample the steepest slopes of the craters. The bright ejecta produced erroneously steep slopes in the photoclinometry data that artificially inflated the bulk slope statistics, as the DEMs showed the ejecta actually has low relief (Fig. 30).

Altogether, these investigations indicate that secondary craters from Corinto do not pose a significant hazard to the InSight lander. First, their depth/diameter ratios are very low, only ~0.05, which is much lower than is typical for secondary craters. The slopes within these craters are also low: <~11° for theoretical shape models that match the qualitative shapes of elevation profiles, and maximum slopes within DEM profiles average only ~5°. Even using higher-resolution photoclinometry, only 0.4 % of the area over these secondaries has slopes

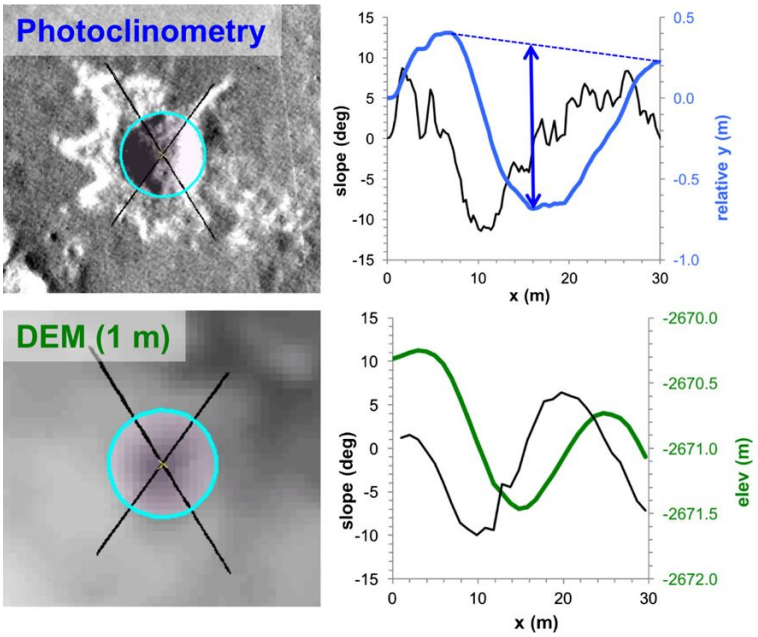

Fig. 30 Example profiles of the same ~22 m diameter secondary crater in 25 cm photoclinometry (*above*) and 1 m DEM (*below*) data. *Left* is image of the data with profiles shown as lines. *Right* are plots of the slope (*black*) and elevation across the craters. Both data show a parabolic crater shape with depth of 0.98 m and d/D of 0.06

>15°, and the secondaries themselves are only 1.5 % of the area of the E9 ellipse region. Finally, bulk slope statistics from both photoclinometry and stereogrammetry did not show any significant increase over areas of high secondary density compared to other areas with few secondaries.

7.8 Regolith Thickness

Early mapping efforts using THEMIS thermal data revealed craters with high thermal inertia halos that correspond with continuous ejecta blankets. CTX images at 6 m/pixel subsequently showed 10 m size boulders and bright ejecta that extend radially ~1 crater diameter (D) from the rims of relatively fresh ~100 m diameter craters. Further detail from HiRISE images at 25 cm/pixel confirmed the observation of 1 m to 10 m boulders in the ejecta of these craters. These Rocky Ejecta Craters (RECs) provide evidence of a competent bedrock unit or a boulder-rich disaggregated unit at a depth beneath the surface (Fig. 31). However, initial observations (Golombek et al. 2013b) also revealed that smaller fresh craters, most at diameters below 50 m, completely lacked rocks in their ejecta (Fig. 31a). This is consistent with the presence of a loosely consolidated, relatively fine-grained surficial layer without many large rocks that buffers smaller impact events, preventing access to the deeper rocky unit (Fig. 31b).

To constrain and quantify the depth to the rocky unit, and thus the thickness of the regolith, we mapped and recorded the diameter of all RECs to determine the onset diameter at which rocks first appear in the ejecta blankets of craters across 17 HiRISE images in ellipse E9. Warner et al. (2016, this issue) present a broader analysis of regolith development,

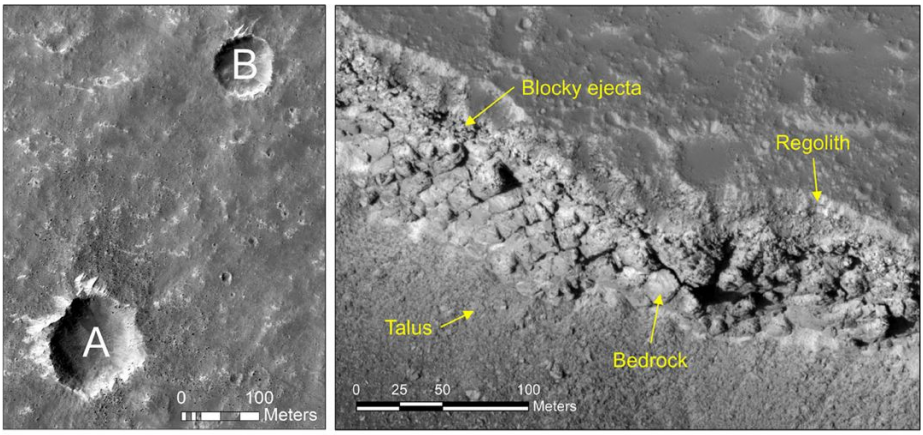

Fig. 31 (**a**) HiRISE image ESP_035640_1845 displaying a relatively fresh rocky ejecta crater (*A*) and a similarly-fresh non-rocky crater (*B*). Both craters exhibit similar infill, show bedforms that have collected against their rims, and share a similar elevated crater rim (morphology Class 3). Crater *A* is 112 m in diameter. Rocks in the continuous ejecta of this crater were excavated from a maximum depth of ∼8 m. Crater *B* is 75 m. Material in this crater's ejecta was excavated from a maximum depth of ∼6 m. The lack of *m*-scale rocks in crater *B*'s ejecta suggests a loose, surficial layer of regolith that is at least 6 m deep. Note small secondary craters from Corinto with characteristic light-toned ejecta. (**b**) HiRISE image PSP_002359_2020 of a portion of the exposed steep scarp of Hephaestus Fossae in southern Utopia Planitia at 21.9°N, 122.0°E showing ∼10 m thick, fine grained regolith overlying blocky ejecta that grades into strong, jointed bedrock

distribution, and thickness across the final 4 landing ellipses. The REC diameters were used to evaluate the depth to the rocky unit using the depth of excavation versus crater diameter relationship (Melosh 1989) in which the continuous ejecta of simple craters is sourced from 0.1 times the transient crater diameter, which is 0.84 times the final crater diameter. Craters that are at the diameter threshold at which rocks first appear in the ejecta provide an upper limit to the regolith thickness. A similar method has been used to determine the near surface stratigraphy of terrains on both the Moon and Mars (e.g., Rennilson et al. 1966; Shoemaker and Morris 1969; Thompson et al. 1979; Bart and Melosh 2010; Catling et al. 2011, 2012). We further quantify the rocky ejecta onset diameter by plotting the SFD of all RECs. In the absence of surface processes that erode or bury craters and rocks, all craters that are large enough to have accessed the rocky layer should have rocks in their ejecta blanket. This is particularly true for fresh craters that are too young to have been obliterated by modern degradational processes that operate at extremely low rates (e.g., Golombek et al. 2006; 2014c). The SFD of these larger, fresh rocky craters should follow a crater production function (Ivanov 2001). If a loose surficial regolith is present however, the slope of a distribution that only includes rocky craters should decline at smaller diameters relative to the production line.

Figure 32 displays cumulative and incremental plots for all RECs within the 17 HiRISE images mapped in E9. The data closely follow a production slope at D > 200 m. This indicates that any impact event that produced a >200 m diameter crater accessed a rocky unit at depth. The largest REC is about 2 km diameter indicating that craters larger than this size were not accessing a rocky unit, which limits the maximum depth of the rocky unit to about 200 m. The slope of the distribution decreases steadily at diameter bins <200 m. This indicates that there are fewer <200 m size RECs than the production model predicts. There are three possible explanations for the decline in the slope of the crater SFD: 1) smaller craters

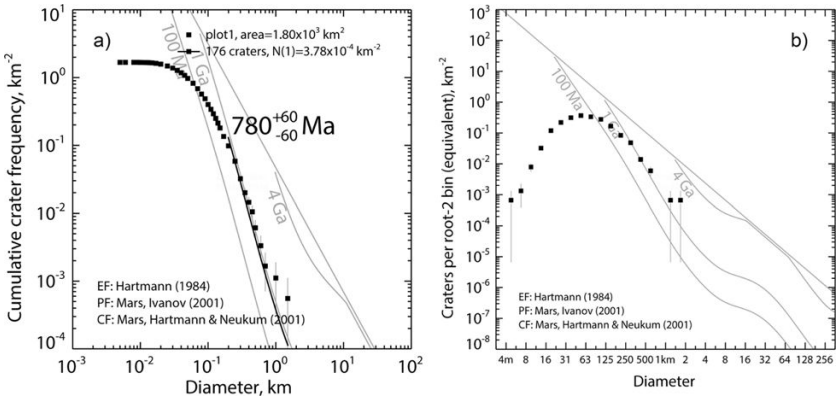

Fig. 32 Size frequency distribution plots for all RECs in 17 HiRISE images across E9; (**a**) cumulative plot with pseudo-log diameter bins and (**b**) incremental plot with root-2 diameter bins. The Ivanov (2001) production function (PF), the Hartmann and Neukum (2001) chronology function (CF), and the Hartmann (2005) equilibrium function (EF) are shown. Note the largest REC is $<\sim$2 km diameter and the deficit of RECs relative to the production function for craters $<$250 m diameter

and their ejected rocks were missed during our count due to a combination of human error, image quality, illumination angle effects, and/or resolution limits of the dataset, 2) smaller craters (and their ejecta rocks) were preferentially obliterated due to surface processes at the landing site, and 3) smaller impact events did not access the rocky unit and thus provide evidence for a regolith.

We discount explanation 1 for three reasons. First, every image and crater counted in the regolith analysis was cross-checked by at least two individuals. Second, subset counts from a single HiRISE image and from multiple images taken at similar solar illumination angles still exhibit a similar SFD roll-over. Third, the slope decrease in the data begins at a large diameter (200 m) relative to the resolution limit for identifying both craters of this size and meter-sized blocks that are ejected from them (see further discussion in Warner et al. 2016, this issue).

To address explanation 2, we evaluated rates of crater degradation to describe the influence of these processes on the slope of the SFD (Sweeney et al. 2016; Warner et al. 2016, this issue). We use the term degradation to encompass all possible processes of crater removal on Mars including gravity diffusion of the interior rims, aeolian scour, infill by aeolian sediments, and gardening by impacts. We classified the RECs into 5 groups; Class 1 represents the idealized pristine crater that has rocks in a continuous annulus around the crater. Class 5 represents the most degraded example that still preserves some rocks in its ejecta. Class 1 craters are rare throughout E9. Therefore, Class 2 craters represent the majority of fresh, rocky craters in our dataset. To further quantify crater morphology we utilized 3 HiRISE digital elevation models (DEMs) from E9 to measure the depth (d) and diameter for a subset of our class 1 to 5 craters.

The timescale of degradation between the most degraded Class 5 RECs and the least degraded Class 2 RECs is approximately 500 to 700 Ma (Sweeney et al. 2016). Using the topographic data coupled with the crater model ages, we estimate a crater degradation rate of 0.02–0.03 m/Myr for 200-m-size craters, similar to other Hesperian to Amazonian erosion rates on Mars (Golombek et al. 2014c). Assuming similar degradation rates for 100 to 200 m size craters and using standard d/D of 0.2 for fresh, simple primary craters of this size (Wood and Andersson 1978; Pike 1980; Garvin et al. 2003;

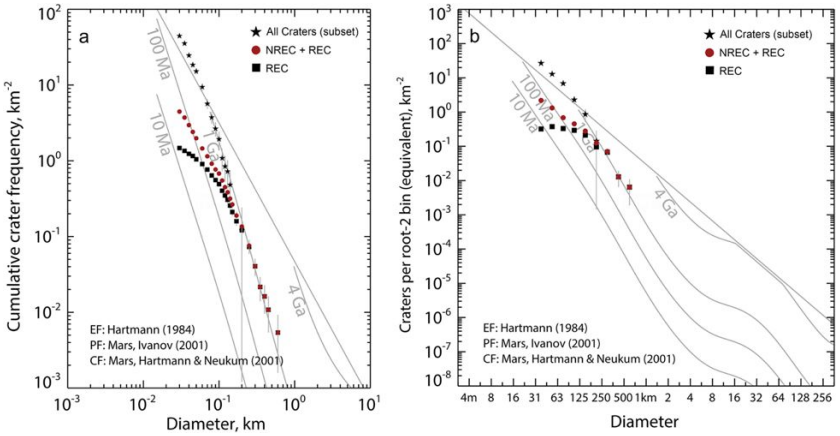

Fig. 33 Crater size frequency distribution plots for RECs (*black squares*), RECs + NRECs (*red dots*), and All Craters (*black stars*) counted from 3 HiRISE images in E9. The count of All Craters is derived from a smaller subset area within one image. (**a**) Cumulative plot with pseudo-log diameter bins. (**b**) Incremental plot with root-2 diameter bins. The percent area covered by regolith was determined by comparing the values for number of craters km^{-2} for RECs to the values for the RECs + NRECs using the incremental plot (**b**)

Tornabene et al. 2013), it is feasible that some <200-m-sized craters were completely planed off or buried over 500 to 700 Myr. However, the rates are not large enough to account for complete obliteration of younger crater classes over the shorter timescales that represent the younger degradational classes. Furthermore, estimates of rim degradation suggest an order of magnitude lower degradation rates of 0.008–0.01 m/Myr for 200-m-sized craters. It therefore takes 2 to 3 times longer to plane off the rocky rims as compared to reducing the overall depth of the crater. We suggest that competent, meter to ten-meter-diameter blocks in the ejecta blanket degrade at rates that are similar to our rim degradation rate. Using the maximum rim degradation rate it would take between 100 Myr and 1 Gyr to remove (bury or erode) 1 to 10 m sized rocks, respectively. We conclude that the degradation rates are too low to account for the complete lack of rocks in most <200-m-sized craters, especially for the younger crater classes (Warner et al. 2016, this issue).

If a regolith is preventing the formation of small RECs, then fresh non-rocky ejecta craters (NRECs) should be abundant across the landing site below the 200 m diameter threshold. Here we include the mapped fresh NRECs on SFD plots with the RECs dataset (Fig. 33). This plot reveals a greater slope in the distribution below the 200 m diameter as compared to the REC-only dataset. This distribution closely follows the −2 equilibrium function (Hartmann 1984), suggesting that obliteration processes are at a steady state with respect to crater production. We conclude that crater obliteration plays a role in the roll off of the distribution of the REC dataset. However, degradation alone cannot account for the magnitude and steady decline of the slope of the REC-only distribution at diameters below 200 m. Given the observational evidence of fresh craters without rocks, we suggest that the slope deviation of the REC-only plot from the production curve at $D < 200$ m is partly due to a regolith that is preventing the formation of smaller diameter rocky ejecta craters.

Using the 200 m diameter cutoff and the excavation depth of 0.084, the regolith within the three HiRISE images is at most 17 m thick and likely everywhere thicker than 2 to 3 m based on the near zero slope of the cumulative SFD below the 30 m diameter bin (Warner et al. 2016, this issue). To evaluate the regolith requirement of the HP^3 we estimated the percent area covered by a regolith that is between 3 to 5 m thick. Impact craters that are

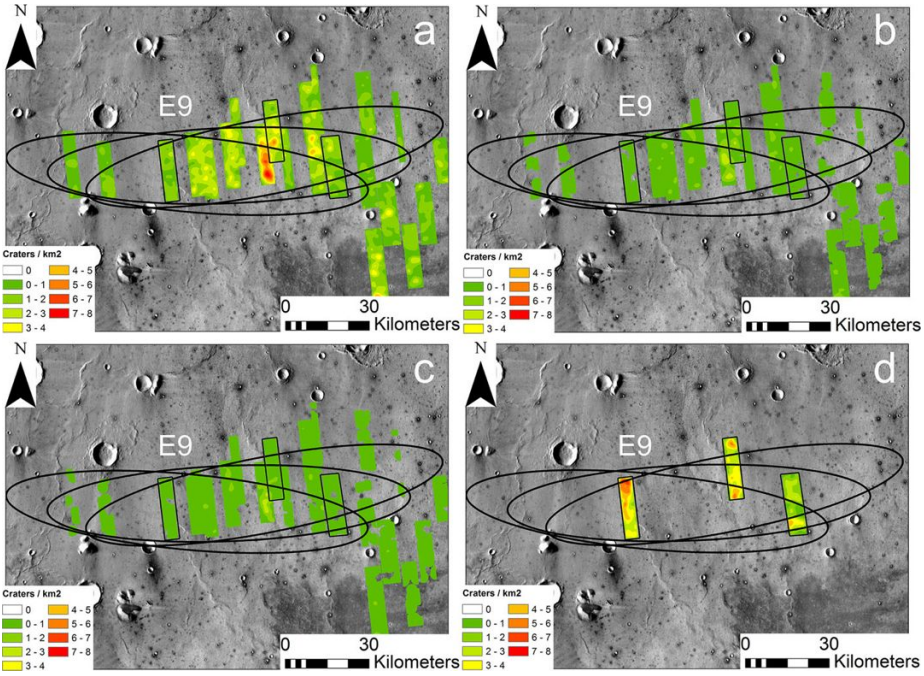

Fig. 34 Maps of the cumulative density of RECs in 1 km bins: (**a**) All RECs excluding Corinto secondary craters, (**b**) RECs between 20 m and 40 m in diameter, (**c**) RECs between 40 m and 60 m in diameter, (**d**) All NRECs counted from the region of the three DEMs. The location of the three DEMs used for the crater morphology analysis are highlighted in *black*. Background is THEMIS daytime thermal image mosaic

approximately 37 m and 62 m in diameter excavate material into their continuous ejecta blanket from a maximum depth of 3 m and 5 m, respectively. Using the incremental plot there are 213 NREC + REC craters in the 63 m bin (root 2 binning, Hartmann 2005). The values from the REC + NREC dataset incorporate the portion of the roll-off in the SFD that is only due to degradation. In that same bin, there are 103 RECs. This indicates that 52 % (error +8 %/ −9 %) of all relatively fresh, Class 1 to 5 impact craters of this size lack rocks in their ejecta blanket, or did not access the rocky unit. In other words, 52 % of this sample set area has a regolith that is at least 5 m thick. The data suggests that the largest disparity between the number of RECs and the NREC + RECs per km^2 occurs within the 31 m diameter bin. For this size range, 85 % (error ±2 %) of all mapped craters lack rocks in their ejecta. This indicates that the 85 % of the region sampled has a regolith that is at least 3 m thick. These results are similar to those derived from impact studies (Hartmann et al. 2001) and fragmentation theory for the observed crater SFDs measured at the site (Sect. 7.10).

To map the spatial distribution of RECs, and thus evaluate possible spatial variations in regolith thickness in E9, we converted each REC to a single point and constructed a density map for the cumulative number of RECs in 1 km pixels (Warner et al. 2016, this issue). The data indicate a higher concentration of RECs (excluding Corinto secondaries) along a 5-km-wide wrinkle ridge located within the west-central portion of the ellipse (Fig. 34a). This higher density region implies a locally thin regolith along the ridge. To determine whether specific diameter craters are responsible for this cluster we also separated the density maps by diameter bins (Figs. 34b,c). The 20 m to 40 m diameter map confirms a cluster of rela-

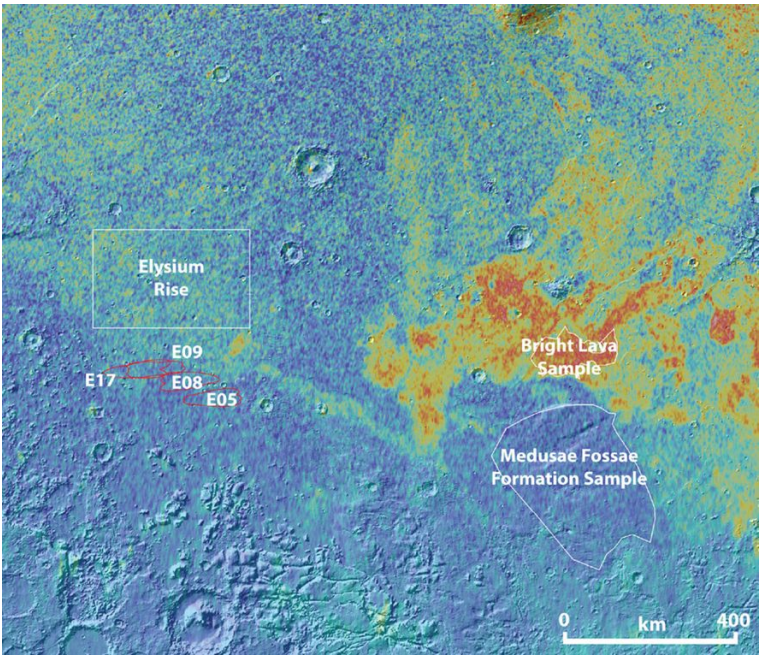

Fig. 35 Arecibo SC-polarization image at 12.6-cm wavelength. Sample regions, including InSight landing ellipses, indicate areas used for values reported in text. The map indicates a radar reflective surface for the C band (7 cm wavelength) InSight radar

tively small RECs along the wrinkle ridge, consistent with a comparatively thin regolith at this location. Finally, we plotted the density of all fresh NRECs in the three HiRISE DEM images (Fig. 34d). These data show a correlation between regions that have a high density of NRECs with regions that have a low density of RECs. This is consistent with local variations in regolith thickness where more NRECs are produced relative to RECs at sites of thicker regolith (and vice versa).

7.9 Radar-derived Properties

7.9.1 Arecibo Roughness Analysis

We use 12.6-cm radar imaging and polarimetric information obtained by Arecibo Observatory on October 3, 2005 (Harmon et al. 2012) to evaluate surface roughness and rock abundance at scales comparable to the radar wavelength. We compare results from the same-sense circular (SC) polarization image to that of past landing sites. Patterns of the radar echoes relative to the geology of the target region enable an assessment of possible changes in surface density with depth or mantling cover (e.g., Campbell et al. 2008).

The SC-polarization image (Fig. 35) shows a radar reflective surface with no indications of anomalous properties in and around the InSight region and thus should be radar reflective for the C-band (7 cm) altimeter on InSight. The backscatter strength from the four final landing ellipses for InSight is moderately low, averaging −17.0 to −16.2 dB, with −16.4 dB in the E9 ellipse. Being in the middle of the typical diffuse reflectivity range, these sites are not solely comprised of rock-poor, porous material at the 12.6-cm scale. The InSight ellipses are

brighter than a large lobe of the Medusae Fossae Formation (−18.9 dB) several hundred km to the southeast. This is consistent with independent radar sounder studies that suggest the Medusae Fossae formation is comprised of low-density sediments (Watters et al. 2007; Carter et al. 2009; Morgan et al. 2015). At the same time, the InSight ellipses are notably darker than returns from the Hesperian/Amazonian volcanic flows just to the north (−14.3 dB) and of the youngest lava flow on Mars from Cerberus Fossae to the east (−8.4 dB).

The radar brightness in the InSight region is similar to that of a field site on Kilauea (Campbell 2001) with a moderately rocky surface, only slightly higher than that of the VL1 site (−17 dB), and considerably higher than that of the VL2 site (−19 dB). Thus, surface rock abundance in the 2–10 cm range at InSight is likely slightly to significantly higher than at the two VL sites. Note that although the HiRISE measurements of rock abundance at the InSight landing sites are considerably lower than either VL site at the meter scale, it is possible that rocks smaller than 10 cm could be more abundant, with a steeper SFD at small diameter similar to the Spirit and PHX landing sites (e.g., Golombek et al. 2012b).

7.9.2 SHARAD Roughness Analysis

With SHARAD data, we compute a roughness parameter from the ratio of echo power integrated over a range of incidence angles to the peak echo power, a measure that is independent of surface reflectivity and is related to the RMS slope of the surface at scales of 10 to 100 m (Campbell et al. 2013). To avoid complicating the results with subsurface returns, we limit the integration to incidence angles $<1.5°$ (i.e., depths $<\sim$60 m). Values for the proposed InSight landing ellipses are compared with those for surrounding terrains and for past landing sites. We also use a complementary model-based statistical approach to assessing surface properties from SHARAD data wherein coherent and incoherent components are separated by fitting the amplitude distribution with a probability density function (Grima et al. 2012, 2014; Putzig et al. 2016, this issue). This method allows constraints to be placed on RMS heights and dielectric permittivity (Putzig et al. 2016).

Our map of SHARAD-derived RMS-slope roughness parameter (Fig. 36) indicates that the four final ellipses are in a part of the study area that is smoothest at 10–100 m scales, except for the lava flows just to the northeast that are somewhat smoother. The four-ellipse region is both smoother and has a narrower distribution of smoothness relative to nearby areas to the east and west. Among the four final ellipses, there are only minor differences in roughness distributions. Note the similarity of the SHARAD derived roughness map (Fig. 36) to the MOLA pulse spread and 100 m extrapolated roughness maps (Figs. 19 and 20) suggesting both instruments are measuring a smooth surface at this length scale.

Because the InSight lander is similar to the successful PHX lander, there is significant value in making comparisons between the PHX landing site and the InSight region. SHARAD data analysis reveals the landing region has a very similar roughness distribution to that of the PHX landing site (Fig. 37). In comparison to other lander missions, E9 distribution peaks at a lower roughness value to that of VL2 in Utopia Planitia. The power of surface returns at InSight is also similar to that of PHX but larger by several dB than that of Meridiani. This is interesting considering returned power is inversely proportional to surface roughness, and that Meridiani is smoother than either E9 or the PHX site (Fig. 37). This suggests the dielectric permittivity and/or density of the near surface of PHX and E9 is comparable and higher than that of Meridiani. The PHX site is known to have a shallow ice table extending between a few centimeters to $\sim$35 m depth (Putzig et al. 2014). In contrast, Meridiani has a stack of sediments up to a few 100 m thick with no evidence in SHARAD

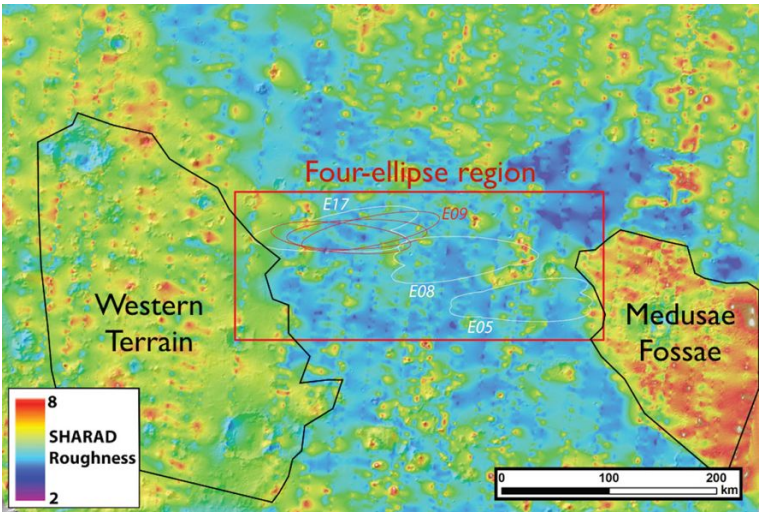

Fig. 36 Map of SHARAD-derived RMS-slope roughness parameter in the InSight region. Areas used to assess roughness distributions indicated by *black*, *red*, and *white* polygons and InSight ellipses

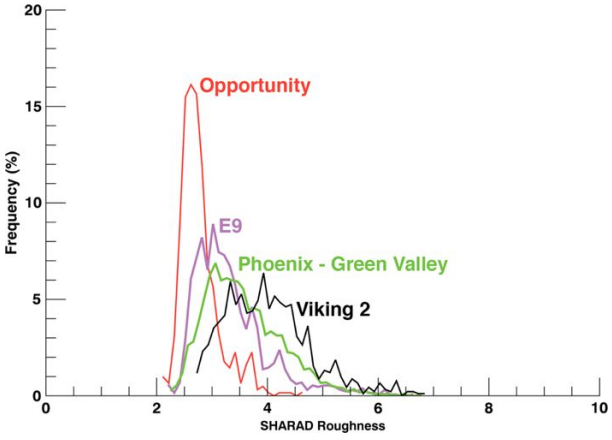

Fig. 37 Frequency distribution of SHARAD roughness values for the E9 ellipse and previous landing sites. The E9 ellipse exhibits a similar roughness distribution to that of Green Valley, where PHX landed

data for large dielectric contrasts (Putzig et al. 2014). Considering the InSight landing site is within volcanic terrain (i.e., dense lava flows consisting of high permittivity) and extremely unlikely to host ground ice due to the low latitude, the similarity in power is likely explained by the presence of a low density material (e.g., regolith) overlying more intact rock within the upper range cell of the surface return (i.e., within 10–20 m depth), an interpretation also supported by RECs (Sect. 7.8) and fragmentation theory (Sect. 7.10).

Using the RMS height method, we find that the open, middle, and close variants of the final landing ellipse all have similar statistics, with a slight decrease in coherent power and its ratio with incoherent power (both indicative of smoothness) as the ellipse rotates clockwise with time of launch. The ellipse at the close of the launch opportunity has a slightly broader distribution of amplitudes, indicating slightly more variable terrain. RMS height within the E9 ellipses can be constrained to ∼1.8–2.3 m in the range of expected dielectric permittivities (∼4–10) for the regolith in the InSight region.

7.9.3 SHARAD Sounding Results

For each orbital pass over the InSight region with SHARAD observations, we produce radargrams, along-track profiles showing the returned power versus delay time in an image format. We search for potential subsurface reflections—returns delayed relative to the surface returns in the radargrams—using clutter simulations and custom processing as needed to identify and suppress off-nadir returns and sidelobes while enhancing subsurface returns (e.g., Holt et al. 2008; Putzig et al. 2009, 2014). Where potential subsurface interfaces were found, we mapped their extent and provided an interpretation of the subsurface material properties.

For the collection of SHARAD radargrams crossing the InSight region, we found that most late returns identified as putative subsurface returns correspond to off-nadir surface returns seen in the clutter simulations. Within the landing ellipses for the four final sites, we interpret all late returns as surface clutter. There is a set of low-power, late returns extending ~50 km southward from the southwestern edge of ellipse E9 on four adjacent radargrams that do not have corresponding features in clutter simulations (Putzig et al. 2016, this issue). These returns are delayed 0.40–0.85 μs relative to the surface return, corresponding to depths of ~20–43 m in regolith with a dielectric permittivity of 9 (typical of basaltic materials). We interpret these late returns as coming from a contact between layers of volcanic rocks or between regolith and bedrock. It is not clear why the returns are limited to this particular region.

7.10 Fragmentation Theory and Models

In this section, we consider the implications of a model based on the underlying statistics of fragmentation for the rock distributions and regolith thickness at the landing site. Under repeated fracture events (in this case, dominantly impacts), fragmentation results in a particle size distribution described as a negative binomial (NB) function (Charalambous 2014). In considering multiple fragmentation events and incorporating time into an ensemble of fractal fragmentation processes (Turcotte 1997), the steady-state solution of the NB can then be found through particle splitting (Kendall 1949). The model's native form appears in a fractional mass abundance for particles of clast size j at maturity index t and a fracture probability, p_f, which is the scale-invariant chance that any rock splits to the next smaller size.

The maturity index t quantifies the number of fragmentation events experienced by the particle population, in this case set by the number of meteorite impacts at the landing site. For a maturity index of $t = 1$, the NB reduces to the well known power-law relationship for the size distribution from a single fragmentation event expected from fractal analysis (Turcotte 1997). The average regolith gradation with depth can then be predicted by taking into account the cratering production functions and the age of the surface (Hartmann 2005). The NB solutions for multiple fragmentation events in either fractional mass abundance or CFA distributions are not power laws (i.e., fractal), but resemble the Rosin Rammler, Weibull, and exponential distributions (curved on a log-log plot) that have been used previously to describe rock populations (Rosin and Rammler 1933; Gilvarry 1961; Gilvarry and Bergstrom 1961; Wohletz et al. 1989; Brown and Wohletz 1995; Golombek and Rapp 1997; Golombek et al. 2003b, 2008b, 2012b; Craddock and Golombek 2016). The breakdown of fractality can be regarded as the outcome of multiple fragmentation events producing a sum of power-law relationships, which itself is not a power law.

To determine an average fracture probability for the martian regolith, datasets from orbital and ground-truth sources have been used. The NB distribution was fitted for the HiRISE

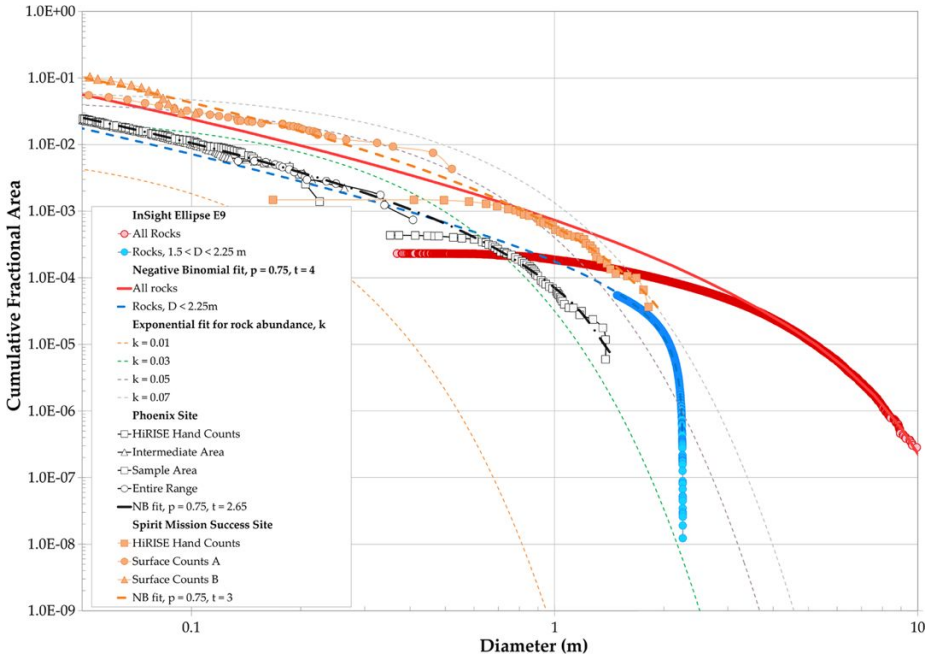

Fig. 38 Plot of the CFA versus diameter of rocks measured in 36 HiRISE images of InSight ellipse E9. The SFD of all rocks measured are in *red* with the NB fit (*solid red line*, $p_f = 0.75$, $t = 4$) for rocks larger than 1.5 m diameter. Rocks larger than 1.5 m and smaller than 2.25 m diameter are shown in *blue*. This SFD distribution is parallel to the exponential model of ~5.7 % rock abundance (the *grey dashed line* is 6 %) at about 2 m diameter used to extrapolate CFA to smaller rock diameters (*colored dashed lines*) (Sect. 7.5). The NB fit to this distribution is shown as the *blue dashed line*. Similarly, the PHX HiRISE counts (Heet et al. 2009) are shown in large open squares, with the NB fit (*black dash-dot line*, $p_f = 0.75$, $t = 2.65$) just for these data. The extrapolation of the fit to the PHX HiRISE data accurately predicts the surface rock counts down to 0.05 m (with data from the Intermediate Area, Sample Area and Entire Range from Heet et al. 2009 and Golombek et al. 2012b). For the Spirit landing site, or CMS, the extrapolation from the HiRISE rock counts (Heet et al. 2009) provides a relatively good estimate of the surface counts (surface counts A from Golombek et al. 2005, 2006; surface counts B from Heet et al. 2009) down to 0.05 m. This NB fit is similar to the exponential model for 5.7 % rock abundance (Sect. 7.5) and supports the use of the exponential model to extrapolate the SFD of rocks below the resolution limit of HiRISE

rock counts at PHX, the Spirit landing site (Columbia Memorial Station, CMS), VL2 and MPF, giving a consistent fracture probability, $p_f = 0.75$. These combined sources also allowed validation for the prediction of the lander surface counts based purely on the NB extrapolation from the HiRISE rock counts. The maximum maturity index of the observed rock population appears to occur at InSight for $t = 4$ (consistent with the site's well developed regolith), although this is an average of the whole ellipse E9, unlike the locally estimated abundances from the other landing sites or the average from the 150 m tiles derived in Sect. 7.5. Data from CMS and PHX (Golombek et al. 2005, 2006, 2012b; Heet et al. 2009), which have the nearest rock size-frequency distributions to InSight (Sect. 7.5), have been used to validate the NB. In Fig. 38, the NB fits to just the HiRISE PHX and CMS rocks yield curves that when extrapolated provide an excellent fit to the lander rock counts as well as the measured CFA of all rocks between 1.5–2.25 m diameter measured at ellipse E9. These extrapolations are also similar to those of the exponential models below the detection limit.

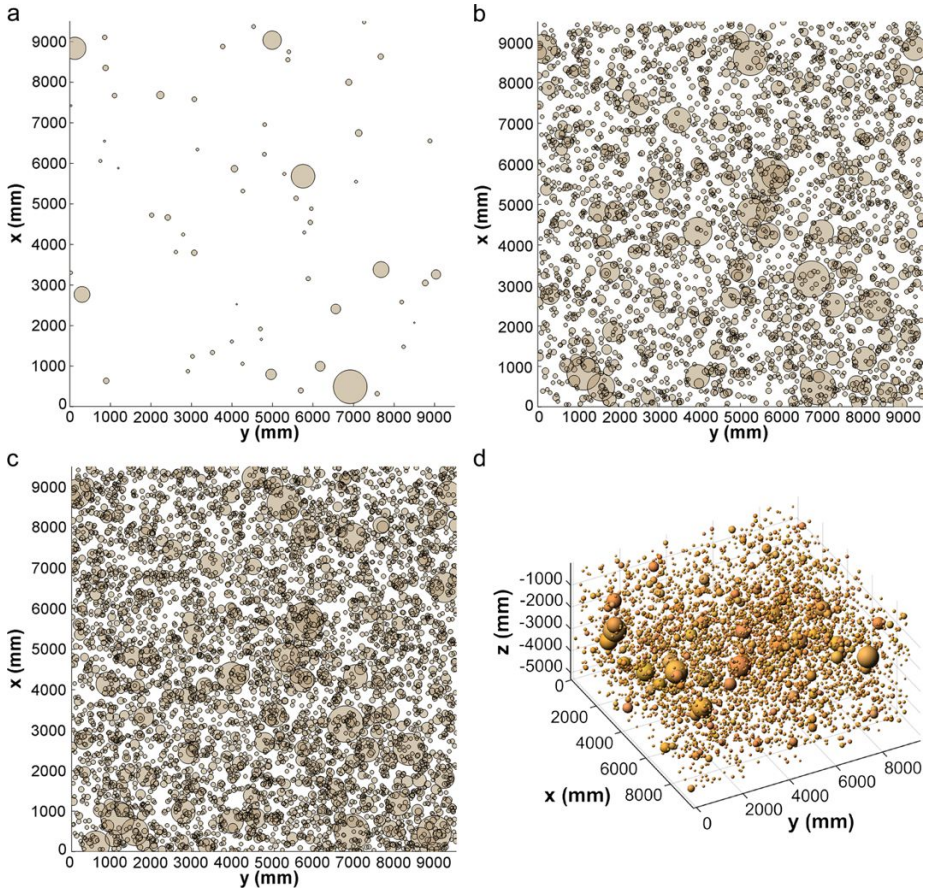

Fig. 39 Digital regolith particle SFD via Monte Carlo simulations of the NB population model, for a maturity index of $t = 4$ and $p_f = 0.75$. (**a**) Map view depicting randomly distributed particles >10 cm occupying 2.5 % of the surface in a 9.5 m × 9.5 m patch. (**b** and **c**) 3 m and 5 m depth views showing 44 % and 59 % of the projected area covered with particles larger than 10 cm, respectively. (**d**) The corresponding population in a three-dimensional view showing particles >10 cm

NB fits to a sum of all 36 processed rock counts from HiRISE images (Sect. 7.5) of the InSight landing ellipse are shown in Fig. 38. The measured CFA SFD for all rocks is shown as well as the NB fit for rocks larger than 1.5 m. Because most detections above 2.25 m diameter are not rocks (Sect. 7.5), we also show the CFA for just rocks between 1.5 m and 2.25 m diameter, which is the method used to derive the CFA in Sect. 7.5. Recalculating the NB fit to this selected data, using the same fragmentation parameters but limiting the largest rock to 2.25 m, gives the blue dashed line that at about 2 m diameter is parallel to the exponential size-frequency distribution model for a rock abundance of 5.7 %, which can be considered a bulk average for the landing site.

To measure the heat flow to within ± 5 mW m^{-2} within one martian year, the HP^3 mole must penetrate at least 3 m below the surface, but testing shows that rocks larger than 10 cm in its path could inhibit its descent. From our model's prediction of the particle size distribution of the regolith, we can estimate the probability of the HP^3 encountering such a rock along its path. Figure 39 shows a progressive series of projections for a NB distributed

synthesized digital soil (Charalambous et al. 2011) at a maturity index of $t = 4$ with all the expected rocks larger than 10 cm randomly distributed in a 9.5 m by 9.5 m by 5 m rectangular cuboid. The probability of reaching a particular depth is then calculated from the mean free path for the mole derived from the fractional projected area of these rocks at that depth. The most pessimistic assumption is that any contact between the mole and a 10 cm diameter rock will halt penetration, which yields a 46 % or 30 % probability of penetrating 3 m or 5 m, respectively. However, tests have shown that the HP3's penetration is not halted if the mole contacts an obstructing rock at a glancing angle, and there are different ways of incorporating this into the model. In the first assumption, we can allow any trajectory of the mole tip outside of the obstructive rock such that any contact at the projected periphery that is smaller than the mole's radius ($r = 0.013$ m) will result in deflection around the rock, but that other contact would stop the mole. Results for the NB synthesized soil in this scenario indicate a 57 % or 41 % probability of penetrating 3 m or 5 m, respectively. Alternatively, tests have shown that if the mole encounters a rock face at $<45°$, it will deflect around it. For spherical rocks, this reduces the obstructive area by half. Such an assumption increases the probability of success of reaching 3 m to 76 % and a 65 % chance of reaching 5 m.

The above estimates have been made using a Monte Carlo synthesis of a NB randomly distributed particle population, or analytically via the NB parameters incorporated into a Poisson process that yields a mean free path solution (Charalambous 2014). For comparison we have also calculated the success of penetration with the exponential models using a rock abundance of 5 % and a chord-length function or mean free path (Lu and Torquato 1993) to estimate the probability of success. For the intermediate case above, the match is identical at 3 m and 5 m with 57 % and 41 % success, respectively. For the case where deflection of the mole occurs at angles $<45°$ and 10 cm rocks stop the mole, the probability of penetrating 3 m and 5 m deep are 75 % and 62 % (with the NB indicating a 76 % and 65 %), increasing to 85 % and 74 % if 15 cm diameter particles can be moved by the mole, respectively. For a rock abundance of 1.2 % (the average of 150 m tiles in E9) or 2.5 % (the average of all smooth terrain in 150 m tiles), the probability of penetrating 3 and 5 m deep with deflection exceeds 98 % or 90 %.

In these estimates, we have assumed that the regolith is formed by a NB process, without subsequent sorting. If such sorting preferentially removes the finer particles there will be an increase of the risk of HP^3 failing to penetrate this far, while deposition of finer particles will reduce it. The InSight landing site may be broadly in equilibrium between fragmentation by impact and redistribution of fines (e.g., Sect. 7.8), and this can be tested after landing.

8 Assessment of Landing Success

8.1 EDL Safety Considerations

Site specific safety considerations for EDL can be divided into three distinct categories based on the manner in which the spacecraft interacts with the local environment: 1) vehicle interactions with the local atmosphere during entry and parachute descent, 2) radar-terrain interactions during parachute descent and powered flight, and 3) lander mechanical interactions with the surface during touchdown. Due to both functional and temporal separation, EDL safety for each of these interactions can be considered in a largely independent fashion.

8.1.1 Atmospheric Interactions

The performance of the InSight EDL system is sensitive to atmospheric variability during the hypersonic entry and supersonic/subsonic parachute descent segments of EDL. After separating from the parachute and igniting the descent engines, the remainder of EDL is largely insensitive to aerodynamic forces and therefore becomes largely insensitive to atmospheric variability. Further, EDL is architected to include sufficient altitude and timeline margin to ensure that the variability in performance during entry and parachute descent does not impact the initial conditions (altitude/velocity) of terminal descent. In other words, the terminal descent segment of EDL is fully decoupled from atmospheric variability by design.

Prior to terminal descent, EDL is most sensitive to bulk density variations and atmospheric winds. Bulk density determines whether there is sufficient atmosphere to aerodynamically decelerate the vehicle to achieve the conditions needed to start terminal descent at the proper altitude and velocity. The landing site elevation constraint (<-2.5 km) was selected to provide positive altitude/timeline margin across all modeled atmospheres. EDL is sensitive to atmospheric winds at altitudes from 2–50 km, which can influence parachute inflation loads, aerothermal heating, vehicle dynamics during parachute descent, and to a lesser extent, EDL altitude and timeline margins.

Multiple dispersed atmosphere models were developed to envelope the set of possible atmosphere states that might exist during the InSight arrival season (see Sect. 5). Dispersed models were generated for scenarios with: no notable storm activity; a localized regional storm; a global dust storm; and a decaying global dust storm. Each of these atmosphere models was incorporated into the end-to-end EDL simulation run using the Program to Optimize Simulated Trajectories (POST). EDL parameters are adjusted to manage critical performance metrics in response to each unique atmosphere model. For example, the parachute deployment trigger parameters can be adapted to manage parachute deployment loads independently for each atmosphere model. A consistent set of dispersed atmosphere models was assumed for all locations in Elysium. End-to-end simulation results prove the ability to land as high as -2.5 km anywhere in Elysium while meeting all driving EDL requirements. No atmospheric discriminator was identified that would favor any site in Elysium over any other.

8.1.2 Radar Terrain Interactions

Safe landing requires direct measurement of surface relative altitude and velocity using the on-board radar. These measurements begin during parachute descent at altitudes as high as 2,500 m above ground level and nominally are taken continuously throughout the remainder of EDL until just before the lander touches down on the surface. At altitudes below 30 m, the radar measurements become less reliable and are no longer used for on-board navigation.

Simulation of radar interaction with the terrain is an important verification step to ensure that the geometry of the surface does not lead to errors in estimating ground relative altitude and velocity. This verification is done in the POST end-to-end simulation by incorporating high-fidelity DEMs and a high-fidelity radar model that simulates the complexities of the radar beam's interaction with the surface as well as the internal function of the radar electronics. Multiple DEMs were selected for simulation to represent the variety of terrains seen at the landing site. The only notable difference identified in the radar performance over different terrains was a known sensitivity to surface slopes at touchdown. DEMs with higher slopes exhibited slightly higher velocity errors at touchdown, as expected. This difference is not significant enough to discriminate any particular landing ellipse from another as the differences between DEMs were small and healthy margins remain for all DEMs examined.

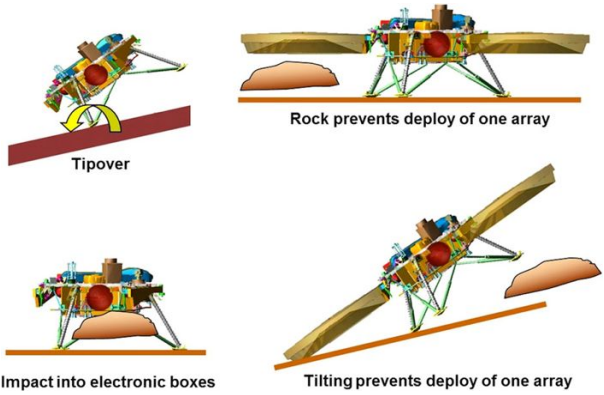

Fig. 40 Examples of possible touchdown failure modes described in the text

8.1.3 Lander Terrain Interaction

Lander interaction with the terrain is the dominant environmental interaction that influences the landing site safety assessment. Risks posed by atmospheric interactions and radar-surface interactions are negligible in comparison. The lander encounters the surface with a vertical velocity of 2.4 ± 1.0 m/s and a horizontal velocity of <1.4 m/s. The vehicle lands on three legs—each of which contains crushable material to absorb impact energy and bring the lander to a complete stop. Each leg is equipped with a touchdown sensor that will signal touchdown once the lander footpad begins to support the weight of the lander on the surface after which all of the descent engines are shut down.

The primary risks to the lander during touchdown are associated with lander stability (e.g., tipping over) and ground clearance (e.g., landing on a rock) (Fig. 40). The lander is stable when landing on planar surfaces with slopes up to 15°. Slopes of this magnitude occur in much less than 1 % of the area of the candidate ellipses and thus the landing slope sensitivity is not a major contributor in the overall hazard assessment for the ellipses considered. Instead, the overwhelming majority of identified hazards are associated with rocks under or near the touchdown location.

The InSight lander is vulnerable to three primary failure modes associated with rocks during EDL: 1) a rock underneath one of the lander's footpads during touchdown causes an effective tilt of the lander that exceeds the allowable limit of 15°; 2) a rock underneath the bottom of the lander deck exceeds the ground clearance of the lander and impacts one of the electronics boxes housed there; and 3) a rock next to the lander after touchdown prevents one of the solar arrays from deploying completely and compromises the amount of solar power that can be produced for surface operations. These failure modes are shown graphically in Fig. 40.

On a planar surface, and in the absence of rocks, the lander is tolerant to a single rock up to 45 cm tall underneath a footpad before the resultant tilting may prevent deployment of one solar array. The total area of the three footpads is approximately 0.2 m^2. Similarly, on a planar surface the lander is designed to have 45 cm of ground clearance to accommodate rocks underneath the lander. Any energy absorbed by the crushable material inside the lander legs will result in shortening of the legs and an associated loss in ground clearance of up to 10 cm depending on the topography of the landing site and the state of the vehicle just prior to touchdown. The total area of the lander bottom enclosure is approximately 2.5 m^2. Lastly, and again on a planar surface, the deployable solar arrays are designed to have a ground clearance of 55 cm to accommodate rocks underneath the deployed arrays. The

combined area covered by the two deployable solar arrays is approximately 7.5 m^2. Despite having higher ground clearance than the lander deck, the significantly larger area of the deployed solar arrays results in the risk of incomplete solar array deployment (e.g., due to a rock) being the most significant risk associated with the touchdown event and subsequent transition to surface configuration.

Assuming the rock SFD is similar to models based on measured distributions at existing landing sites (e.g., Golombek and Rapp 1997; Golombek et al. 2003b, 2008b, 2012b), then the numbers above translate to an overall rock-induced failure rate of ∼0.35 % in regions with a 5 % CFA, a failure rate of ∼2.5 % in regions with a 10 % CFA, and exceeds 13 % for rock abundance of 25 % for hemispheric rocks. These failure rates are predominantly due to the large areas associated with the deployed solar arrays and the requirement that both arrays deploy fully (for surface operations for a full Mars year). For rock maps produced for the simulations, 150 m pixels in which no rocks 1.5–2.25 m diameter were detected (zero CFA), we arbitrarily added 1 rock, which yields a 6 % CFA and thus a minimum ∼0.4 % failure rate. This minimum matches the CFA determined for all rocks 1.5–2.25 m diameter detected in ellipse E9 (Fig. 38).

8.2 Touchdown Success Assessment

Determining the overall probability of a successful landing requires, as a first step, the development of a transfer function to characterize the local probability of a safe landing given a specific slope and rock environment at touchdown. This transfer function was developed by performing multiple Monte Carlo analyses of the touchdown event in the ADAMS multibody dynamics simulation environment. A high-fidelity model of the vehicle was created within ADAMS including: 1) detailed mechanical configuration of the lander legs (including crushable material response), touchdown sensors, lander deck, and deployable solar arrays, 2) vehicle flight software to properly model the delay between touchdown sensor activation, and the subsequent command delays associated with turning off the thrusters, 3) models of the descent engines incorporating pulse rise and thrust decay times associated with each 10 Hz command cycle, and 4) models of the thruster plume reflection off the surface and resultant forces and torques on the lander itself. Conditions of the vehicle's six degree of freedom state just before first contact with the ground are taken as inputs from the end-to-end EDL Monte Carlo simulation. A set of 2001 individual cases, provide the initial condition for the ADAMS touchdown simulations.

Multiple Monte Carlo simulations were performed in this fashion. One set of simulations was performed for rock free surfaces having slopes of varying from 0° to 20°. Another set of simulations was performed for flat surfaces having rock abundances from 0 % CFA to 40 % CFA. For each Monte Carlo run, a unique rock field was generated according to the rock abundance model of Golombek and Rapp (1997) and Golombek et al. (2003b, 2008b, 2012b) assuming hemispheric rocks (Sect. 7.5). The rock field was then used to determine the heights of rocks under each lander footpad for each case. After the simulation for a particular case was completed, the rock field was inspected to identify any negative clearance relative to the lander or the deployed solar arrays. The results of these sensitivity studies, summarized in Table 9, provide the transfer functions needed to determine the probability of successful landing at a location having a given slope and rock abundance. These transfer functions are referred to as the EDL capability matrix.

8.3 Hazard Map Creation

Given the EDL capability matrix, we are able to assess the localized probability of successful touchdown given the measured slope and rock abundance at a particular location or area,

Table 9 EDL capability matrix showing failure rates for rocks and slopes

Rock CFA	EDL and array
	% Failure rate
0–5 %	0.35 %
5–40 %	$1.5323x^2 + 0.1935x - 0.01$
>40 %	100 %

Surface slope (deg)	EDL + arrays	Instrument
	Failure rate	Out of spec.
0–5	0 %	0 %
5–10	0 %	0 %
10–15	0 %	0 %
15–20	9.7 %	100 %
>20	100 %	100 %

provided that the slopes, rocks and landing probability are approximately uniform across that area. Performing this assessment for each location across the entire landing region enables us to build a map that identifies the local probability of landing success or failure for a particular landing ellipse across the entire landing region.

For the purposes of building the hazard map, the landing region was subdivided into 150 m by 150 m cells with the slope and rock abundance determined in each cell. Cells of this size result in a sufficiently statistically meaningful population of observed rocks in HiRISE images (see Sect. 7.5). In similar fashion, 2 m length scale slope statistics (Horn 1981) from photoclinometry and the DEMs were binned across the same 150 m by 150 m cells to identify the probability of landing on a given slope within each cell. Hazard maps are based on mosaics within a bounding box of 198,000 m by 79,500 m (each dimension equally divisible by our final mosaic pixel size of 150 m), surrounding the final landing ellipse with the limits 3.928°N–4.878°N latitude, 134.168°E–137.064°E longitude. All mosaics were georeferenced in an equirectangular projection with center longitude and latitude equal to zero, with a Mars spherical radius of 3,396,190 m.

An example hazard map is shown in Fig. 41. Areas where HiRISE images are available appear as darker blue as the increased image resolution allowed for a better estimation of rocks and slopes. Areas not covered by HiRISE images were assigned hazards based on terrain types identified from analysis of CTX mono images (see Sect. 7.2). Landing hazards for each terrain type were assessed based on samples of HiRISE images over a portion of that terrain type.

8.4 Landing Probability Distribution

The end-to-end EDL Monte Carlo simulation incorporates dispersed initial conditions, dispersed atmosphere models, and dispersed vehicle models to determine the relative probability of touching down in any specific location within the landing ellipse. The spatial distribution of landing probabilities can be approximated by a bivariate Gaussian distribution centered at the landing target. The azimuthal orientation of this distribution varies as a function of launch date. The dimensions of the ellipse vary as a function of the navigated state and knowledge uncertainty at entry as well as with the atmospheric conditions at arrival. A variety of Monte Carlo simulations were run to generate a set of landing point

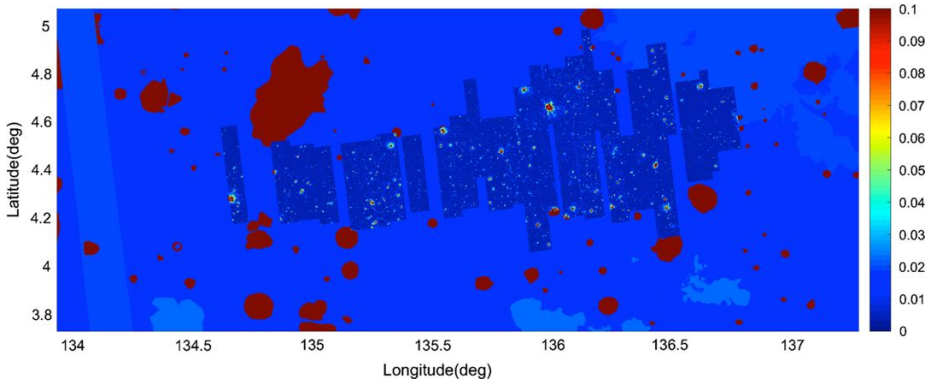

Fig. 41 Hazard map of ellipse E9 showing the probability of failure (*scale at right*) based on terrains mapped in CTX images and average slope and rock CFA for them and slope and rock measurements for HiRISE images shown in *darker blue*

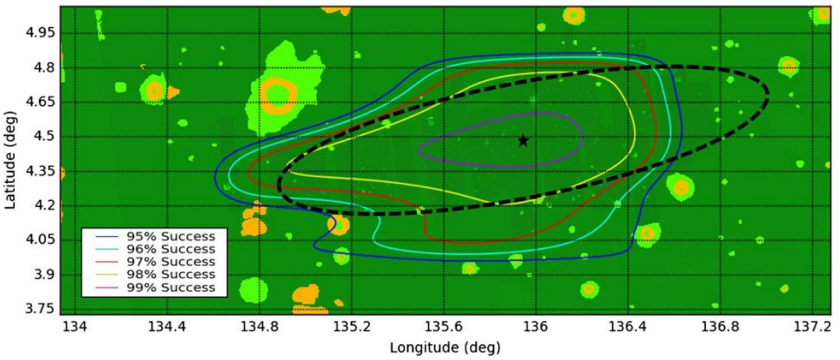

Fig. 42 Contours of the probability of success for different ellipse center points based on the opening of the launch period (3/18/16) for ellipses of 130 km by 30 km with the azimuth shown for the optimal ellipse. The optimal *black dashed ellipse* with center star, E9, has a greater than 99 % probability of success

distributions that encompassed the range of ellipse orientations and ellipse sizes expected on landing.

8.5 Overall Assessment and Ellipse Optimization

Equipped with the regional hazard map and a set of landing point probability distributions, it is straightforward to assess the overall probability of successful touchdown for any given landing target. Examples are shown in Figs. 42 and 43. The background of these figures contain the same hazard map shown in Sect. 8.3 (but with different colors). Colored contours of equal integrated success probability are superposed on the hazard map. These contours indicate the overall probability of success associated with an ellipse centered at that location (e.g., any ellipse of that size and orientation centered on the yellow line would have an associated overall probability of success of exactly 98 %). The optimal target is indicated by a black star and the landing ellipse associated with the optimal target is indicated by a dashed black line. Note that the optimal target changes position minimally between open and close ellipses.

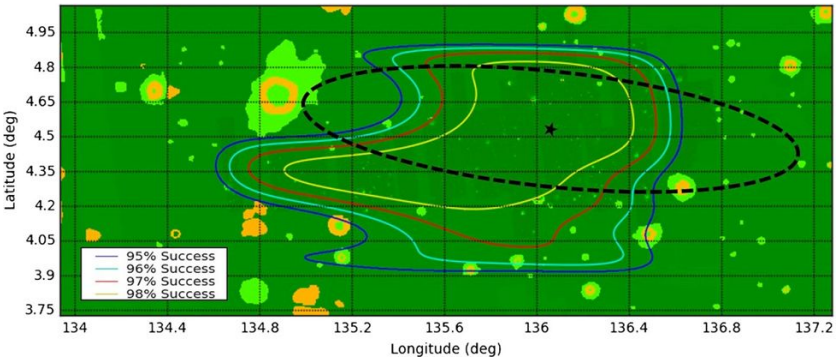

Fig. 43 Contours of the probability of success for different ellipse center points based on the close of the launch period (3/30/16) for ellipses of 130 km by 30 km with the azimuth shown for the optimal ellipse. The optimal *black dashed ellipse* with center star, E9, has a greater than 98 % probability of success and is offset from the optimal center for the open of the launch opportunity by only a few km, indicating a broad region with very high probability of success for all launch azimuths

As described in Sect. 6.11, ellipses for the 2018 opportunity are almost identical to those for 2016 and similar plots of success contours indicate the same area has the highest probability of success (exceeding 99 %) for open, middle and close azimuths (Fig. 10). These ellipses are already almost completely covered with HiRISE images (Fig. 10) and the associated rock and slope hazard maps. Landing site safety probabilities this high are similar to the safest site selections that have been made for other landers on Mars (e.g., Golombek et al. 2003a, 2012a; Spencer et al. 2009).

The success contours are useful for identifying the safest ellipse and making targeting decisions during Mars approach. The selected landing site benefits from a large locus of ellipse centers that jointly exceed 98 % touchdown success for all reasonable combinations of ellipse size and orientation. This will allow for flexibility to consider operational constraints when considering late trajectory correction maneuvers and final targeting decisions. Final target selection will take place after launch (once the arrival azimuth is known). Additional HiRISE images will be processed and incorporated into an updated hazard map before the final assessment is performed.

9 Summary/Conclusions

Selection of the InSight landing site took over four years and included developing and mapping landing site constraints onto Mars to identify prospective areas where ellipses could be placed, mapping terrains where possible landing sites were placed in acquired high-resolution images, characterizing the safety of those terrains, downselection to a smaller number of ellipses to focus image acquisition and study, assessment of landing success via entry, descent and landing simulations through specially constructed atmosphere models and slope and rock hazard maps, and final landing site selection and review. Constraints on latitude, elevation and ellipse size more severely limited prospective landing areas than any previous landing site selection process. These constraints forced the selection of western Elysium Planitia for the placement of roughly 20 ellipses that, unfortunately, are 150–675 km north of MSL, causing communication relay and imaging conflicts (and eventually

data relay conflicts between MSL and InSight). Mapping of terrains in rapidly acquired, extensive CTX images identified large areas of smooth terrain with few rocks or steep slopes between 3° and 5° north latitude and the downselection to four ellipses in this area in July 2013. After acquisition of over 50 HiRISE images of these four ellipses, the development of hazard maps based on rock and slope data products (and their peer review), and engineering landing simulations, ellipse E9 was selected in May 2015. Extensive HiRISE coverage of ellipse E9, almost complete slope and rock based hazard maps and additional simulations led to project certification of the landing site, independent peer review and planetary protection review in October 2015 with a NASA Headquarters briefing in December 2015. The 2016 InSight launch was suspended in late December 2015 due to problems with the SEIS instrument, but the project was reconfigured and authorized by NASA for a launch in March 2018 with no change (somewhat incredibly) to the landing site.

Constraints on the landing site were derived from the EDL scenario and design of the spacecraft, lander and instruments and are similar to the PHX mission. They include: MOLA elevation below −2.5 km for sufficient atmosphere to slow the spacecraft during entry, descent and landing, latitude initially between 15°S and 5°N for solar-power and later 3°N–5°N for thermal management of the lander, ellipse size 130 km by 27 km for ballistic landing trajectory, radar-reflective surface for correct operation of the altimeter, thermal inertia >100–$140\ \mathrm{J\,m^{-2}\,K^{-1}\,s^{-1/2}}$ for a load-bearing surface without substantial fine-grained dust, rock abundance <10 % for low probability of impacting a rock that could damage the base of the lander, impede opening the solar panels, or restrict placement of the instruments on the surface, 1–5 m and 84 m length slopes $<15°$ for touchdown stability, leveling of SEIS and radar tracking of the surface, and a fragmented regolith 3–5 m thick for full penetration of the HP^3 mole. Unlike all other Mars landers, there are no science objectives that influenced landing site selection. Planetary protection requirements are that the landing site be free of water or ice within 5 m of the surface, subsurface discontinuities, high concentrations of water bearing soils or minerals, or liquid water created by the mole that could mobilize a 50 nm particle.

Data and models used to evaluate the InSight landing sites are broadly similar to those used for MSL and include nearly continuous HiRISE, CTX, and HRSC images and selected stereo coverage. Those HiRISE images were used to create nearly continuous rock maps from shadows they cast and fits to exponential models, and 2 m slope maps from DEMs and photoclinometry. Stereo images from HRSC, CTX and HiRISE of the InSight landing site were made into DEMs, and merged during leveling to the MOLA base, creating the first nearly seamless merged topographic map for EDL simulations. Targeted THEMIS thermal images were used to create high-resolution thermal inertia maps, constrain the physical properties of surface materials and variations with depth, map rocky ejecta craters, and compare their thermal response to measured rocks. Finally, Arecibo and SHARAD radar data were used to evaluate reflectivity, surface roughness and shallow subsurface properties and reflectors.

The InSight landing ellipse E9 is located in western Elysium Planitia on volcanic Hesperian plains just north of the dichotomy boundary. Mapping in CTX images in the area defined smooth, etched, dark, gradational etched, ridged, crater rim, highland scarp and ejecta terrains. The E9 ellipse is located dominantly on the smooth terrain, which is the most benign. Rock abundance in the smooth terrain averages ∼2.5 % (well below the 10 % requirement), and is 1.2 % in ellipse E9. At length scales of ∼100 m, MOLA data (extrapolated RMS slopes, relief, and pulse spread), SHARAD roughness, and CTX and HiRISE DEMs indicate very smooth and flat surfaces that would not violate the radar tracking constraint. Slope statistics at 1–5 m length scale from HiRISE DEMs and photoclinometry show that

the smooth terrain has less than 0.5 % area that exceeds the 15° slope (below the engineering constraint of <1 %), and is smoother at this scale than previous landing sites with the possible exception of Opportunity and PHX. The 1 m RMS slope for E9 (~3.9°) makes it the smoothest part of the smooth terrain with the least area (0.1 %) that exceeds 15° slope.

Secondary craters are ubiquitous in the landing site region and are primarily from the fresh, rayed crater Corinto located ~600 km north-northeast of the landing site. These secondaries in DEMs and photoclinometry slope maps show much shallower depth/diameter ratios (~0.05) than expected (0.1) and interior slopes that rarely approach the 15° limit, indicating that they are not a hazard. The area covered by secondaries in E9 is only 1.5 % and slope distributions of the secondaries show 0–0.4 % area with slopes >15°, confirming that they do not contribute significantly to the average slope distributions of the ellipses. Analysis of TES and THEMIS data shows an average thermal inertia of ~200 $J\,m^{-2}\,K^{-1}\,s^{-1/2}$ that is consistent with cohesionless fine sand, no dust layers >2 mm thick, very weak cohesion (<3 kPa), and no outcrops. The low level of seasonal variations in apparent thermal inertia indicates that these properties persist to a depth of 0.5–1 m beneath the surface. Arecibo backscatter maps show a radar reflective surface, and when considered together with the thermal inertia, indicate a radar reflective, load-bearing surface without thick deposits of fine-grained dust. SHARAD observations reveal no subsurface reflectors, water, or ice, except for isolated weak returns south of ellipse E9 that may be related to an interface at 20–43 m depth, perhaps between basalt flows, regolith or bedrock. Study of rocky ejecta craters separate the effects of their degradation due to eolian activity and subsequent cratering from the influence of the regolith. Results indicate that the regolith thickness varies from 3 to 17 m across the area, indicating the HP^3 mole will likely penetrate to 3–5 m, a result supported by the low measured rock abundance and fragmentation theory based on crater counts.

Sophisticated EDL simulations were carried out based on spacecraft—environment interactions with the atmosphere during entry and parachute descent, radar-terrain during descent, and the surface during touchdown. EDL parameters were successfully adjusted to handle four basic atmospheric conditions that could be present during EDL: global dust storm, decaying global dust storm, localized regional storm, and no notable dust storm activity. The probability of failure during atmospheric entry, descent and radar interactions with the surface were negligible in comparison to interactions with the surface at touchdown. Of these touchdown hazards, rocks dominate over slopes. A high-fidelity model of touchdown including a detailed model of the vehicle, its legs, and sensors quantified the probability of failure for different rock and slope conditions. Hazard maps of rock abundance and slope distributions were derived from six HiRISE DEMs, 41 individually tuned photoclinometry slope maps, and 35 rock abundance maps, all derived from nearly complete HiRISE coverage. End-to-end Monte Carlo simulations convolved with the hazard map were used to derive contour maps of the probability of success and the demarcation of the safest ellipses. Ellipse E9, located at ~4.5°N, ~135.9°E, exceeded 99 % probability of success for all likely ellipse sizes and azimuths that rotate clockwise around a roughly east-west azimuth with 2018 launch date.

Acknowledgements Research described in this paper was partially done by the InSight Project, Jet Propulsion Laboratory, California Institute of Technology, under a contract with the National Aeronautics and Space Administration. Production of derived data products and support for the Council of Atmospheres and the Council of Terrains was provided by the InSight Project. The German Aerospace Center (DLR) supported the production of HRSC mosaics. We thank S. Kannan, L. Maki, K. Smyth, D. Hernandez, V. Carranza, E. Bondi, R. Domholdt, A. Davis, M. Wray, S. Melady, W. Painter, C. Hundal, and M. Bouchard for help processing data and maps. We also thank B. Knapmeyer-Endrun, V. Ansan Mangold, K. Herkenhoff and C. Dundas for comments on an earlier draft. M. Grott provided helpful discussions on the interaction of the mole with subsurface rocks. This paper is InSight Contribution Number 17.

References

D.S. Adams, Phoenix Mars Scout landing site risk assessment, in *2008 IEEE Aerospace Conference*, Piscataway, NJ, 2008 (IEEE Press, New York, 2008), pp. 1–8. doi:10.1109/AERO.2008.4526286

F.S. Anderson, A.F.C. Haldemann, N.T. Bridges, M.P. Golombek, T.J. Parker, G. Neumann, Analysis of MOLA data for the Mars Exploration Rover landing sites. J. Geophys. Res. **108**(E12), 8084 (2003). doi:10.1029/2003JE002125

V. Ansan, T. Dezert (the DLR group), Western Elysium Planitia, What is regional geology telling us about sub-surface? in *InSight Science Team Presentation*, Zurich, Switzerland, September 5–9, 2015 (2015), and written communication

R. Arvidson et al., Mars Exploration Program 2007 Phoenix landing site selection and characteristics. J. Geophys. Res. **113**, E00A03 (2008). doi:10.1029/2007JE003021

R.E. Arvidson et al., Results from the Mars Phoenix lander Robotic Arm experiment. J. Geophys. Res. **114**, E00E02 (2009). doi:10.1029/2009JE003408

W.B. Banerdt et al., InSight: a discovery mission to explore the interior of Mars, in *44th Lunar and Planetary Science* (Lunar and Planetary Institute, Houston, 2013). Abstract #1915

G.D. Bart, H.J. Melosh, Distributions of boulders ejected from lunar craters. Icarus **209**, 337–357 (2010). doi:10.1016/j.icarus.2010.05.023

J. Benardini, L. Newlin, InSight PIP 2.4 planetary protection plan. Jet Propulsion Laboratory, California Institute of Technology, Document 75257, Revision A, 74 pp. (2013)

R.A. Beyer, Meter-scale slopes of candidate InSight landings sites from point photoclinometry. Space Sci. Rev. (2016, this issue). doi:10.1007/s11214-016-0287-7

R.A. Beyer, R.L. Kirk, Meter-scale slopes of candidate MSL landings sites from point photoclinometry. Space Sci. Rev. **170**, 775–791 (2012). doi:10.1007/s11214-012-9925-x

R.A. Beyer, A.S. McEwen, R.L. Kirk, Meter-scale slopes of candidate MER landing sites from point photoclinometry. J. Geophys. Res. **108**(E12), 26–31 (2003). doi:10.1029/2003JE002120

R.A. Beyer, O. Alexandrov, S. McMichael, The Ames stereo pipeline: NASA's open source automated stereogrammetry software (Users Guide and Documentation), Version 2.5.2 (2016). http://irg.arc.nasa.gov/ngt/stereo

C. Bloom, M. Golombek, N. Warner, N. Wigton, Size frequency distribution and ejection velocity of Corinto crater secondaries in Elysium Planitia, in *Eighth International Conference on Mars*, Pasadena, CA, July 14–18, 2014 (Lunar and Planetary Institute, Houston, 2014). Abstract #1289

E.P. Bonfiglio, D. Adams, L. Craig, D.A. Spencer, R. Arvidson, T. Heet, Landing site dispersion analysis and statistical assessment for the Mars Phoenix Lander. J. Spacecr. Rockets **48**, 5 (2011, September–October)

J. Bostelmann, C. Heipke, Analysing blocks of HRSC strips for a simultaneous bundle adjustment. ISPRS Ann. Photogramm. Remote Sens. Spat. Inf. Sci. **2**(4), 15–20 (2014)

W.V. Boynton et al., Elemental abundances determined via the Mars Odyssey GRS, in *The Martian Surface: Composition, Mineralogy and Physical Properties*, ed. by J.F. Bell III (Cambridge University Press, Cambridge, 2008), pp. 105–124. Chap. 5

W.K. Brown, K.H. Wohletz, Derivation of the Weibull distribution based on physical principles and its connection to the Rosin–Rammler and lognormal distributions. J. Appl. Phys. **78**, 2758–2763 (1995)

M.J. Broxton, L.J. Edwards, The Ames Stereo Pipeline: Automated 3D surface reconstruction from orbital imagery, in *39th Lunar Planet Sci. Conf.* (Lunar and Planetary Institute, Houston, 2008). Abstract #2419

S. Byrne et al., Distribution of mid-latitude ground ice on Mars from new impact craters. Science **325**, 1674 (2009). doi:10.1126/science.117530

B.A. Campbell, Radar backscatter from Mars: properties of rock-strewn surfaces. Icarus **150**, 38–47 (2001)

B.A. Campbell, Scale-dependent surface roughness behavior and its impact on empirical models for radar backscatter. IEEE Geosci. Remote Sens. **47**, 3480–3488 (2009). doi:10.1109/TGRS.2009.2022752

B.A. Campbell, High circular polarization ratios in radar scattering from geologic targets. J. Geophys. Res. **117**, E06008 (2012). doi:10.1029/2012JE004061

B.A. Campbell, L.M. Carter, B.R. Hawke, D.B. Campbell, R.R. Ghent, Volcanic and impact deposits of the Moon's Aristarchus Plateau: a new view from Earth-based radar images. Geology **36**, 135–138 (2008). doi:10.1130/G24310A.1

B.A. Campbell, N.E. Putzig, L.M. Carter, G.A. Morgan, R.J. Phillips, J.J. Plaut, Roughness and near-surface density of Mars from SHARAD radar echoes. J. Geophys. Res. **118**, 15 (2013). doi:10.1002/jgre.20050

B.A. Cantor, MOC observations of the 2001 Mars planet-encircling dust storm. Icarus **186**, 60–96 (2007). doi:10.1016/j.icarus.2006.08.019

L.M. Carter, B.A. Campbell, T.R. Watters, R.J. Phillips, N.E. Putzig, A. Safaeinili, J. Plaut, C.H. Okubo, A.F. Egan, R. Seu, D. Biccari, R. Orosei, Shallow radar (SHARAD) sounding observations of the Medusae Fossae Formation, Mars. Icarus **199(2)**, 295–302 (2009). http://doi.org/10.1016/j.icarus.2008.10.007

D.C. Catling et al., A lava sea in the northern plains of Mars: circumpolar Hesperian oceans reconsidered, in *42nd Lunar and Planetary Science Conference* (Lunar and Planetary Institute, Houston, 2011). Abstract #2529

D.C. Catling et al., Does the Vastitas Borealis formation contain oceanic or volcanic deposits? in *Third Conference on Early Mars*, Lake Tahoe, NV, May 21–25, 2012 (Lunar and Planetary Institute, Houston, 2012). Abstract #7031

T.E. Chamberlain, H.L. Cole, R.G. Dutton, G.C. Greene, J.E. Tillman, Atmospheric measurements on Mars: the Viking meteorology experiment. Bull. Am. Meteorol. Soc. **57**, 1094–1104 (1976)

C. Charalambous, On the evolution of particle fragmentation with applications to planetary surfaces. PhD Thesis, Imperial College London (2014)

C. Charalambous, W.T. Pike, W. Goetz, M.H. Hecht, U. Staufer, A digital martian soil based on in-situ data. AGU Fall Meeting Abstract (2011). # P43B-1669

P.R. Christensen, Martian dust mantling and surface composition: interpretation of thermophysical properties. J. Geophys. Res. **87**, 9985–9998 (1982)

P.R. Christensen, The spatial distribution of rocks on Mars. Icarus **68**, 217–238 (1986)

P.R. Christensen, M.C. Malin, High resolution thermal imaging of Mars, in *Lunar Planet. Sci. XIX* (Lunar and Planetary Institute, Houston, 1988), pp. 180–181

P.R. Christensen, H.J. Moore, The martian surface layer, in *MARS*, ed. by H.H. Kieffer, B.M. Jakosky, C.W. Snyder, M.S. Matthews (University of Arizona Press, Tucson, 1992), pp. 686–727

P.R. Christensen, D.L. Anderson, S.C. Chase, R.N. Clark, H.H. Kieffer, M.C. Malin, J.C. Pearl, J. Carpenter, N. Bandiera, F.G. Brown, S. Silverman, Thermal Emission Spectrometer experiment: Mars Observer Mission. J. Geophys. Res. **97**(E5), 7719–7734 (1992)

P.R. Christensen, J.L. Bandfield, V.E. Hamilton, S.W. Ruff, H.H. Kieffer, T.N. Titus, M.C. Malin, R.V. Morris, M.D. Lane, R.L. Clark, B.M. Jakosky, M.T. Mellon, J.C. Pearl, B.J. Conrath, M.D. Smith, R.T. Clancy, R.O. Kuzmin, T. Roush, G.L. Mehall, N. Gorelick, K. Bender, S. Dason, E. Greene, S. Silverman, M. Greenfield, Mars Global Surveyor Thermal Emission Spectrometer experiment: investigation description and surface science results. J. Geophys. Res. **106**, 23823–23871 (2001)

P.R. Christensen, B.M. Jakosky, H.H. Kieffer, M.C. Malin, H.Y. McSween Jr., K. Nealson, G.L. Mehall, S.H. Silverman, S. Ferry, M. Caplinger, M. Ravine, The Thermal Emission Imaging System (THEMIS) for the Mars 2001 Odyssey mission. Space Sci. Rev. **110**, 85–130 (2004)

S.M. Clifford, T.J. Parker, The evolution of the Martian hydrosphere: implications for the fate of a primordial ocean and the current state of the northern plains. Icarus **154**, 40–79 (2001)

R.A. Craddock, M.P. Golombek, Characteristics of terrestrial basaltic rock populations: implications for Mars lander and rover science and safety. Icarus **274**, 50–72 (2016). doi:10.1016/j.icarus.2016.02.042

J.A. Crisp et al., Mars Exploration Rover mission. J. Geophys. Res. **108**(E12), 8061 (2003). doi:10.1029/2002JE002038

I.J. Daubar, A.S. McEwen, S. Byrne, M.R. Kennedy, B. Ivanov, The current martian cratering rate. Icarus **225**, 506–516 (2013). doi:10.1016/j.icarus.2013.04.009

I.J. Daubar, M.P. Golombek, A.S. McEwen, L.L. Tornabene, F.J. Calef III, R. Fergason, R. Kirk, R. Beyer, Depth-diameter ratio of Corinto secondary craters, in *47th Lunar and Planetary Science* (Lunar and Planetary Institute, Houston, 2016). Abstract #2950

G. Di Achille, B.M. Hynek, Ancient ocean on Mars supported by global distribution of deltas and valleys. Nat. Geosci. **3**, 459–463 (2010). doi:10.1038/NGEO891

C.S. Edwards, P.R. Christensen, J. Hill, Mosaicking of global planetary image datasets: 2. Modeling of wind streak thicknesses observed in Thermal Emission Imaging System (THEMIS) daytime and nighttime infrared data. J. Geophys. Res. **116**, E10005 (2011a). doi:10.1029/2011je003857

C.S. Edwards, K.J. Nowicki, P.R. Christensen, J. Hill, N. Gorelick, K. Murray, Mosaicking of global planetary image datasets: 1. Techniques and data processing for Thermal Emission Imaging System (THEMIS) multi-spectral data. J. Geophys. Res. **116**, E10008 (2011b). doi:10.1029/2010je003755

B.L. Ehlmann, C.S. Edwards, Mineralogy of the Martian Surface. Annu. Rev. Earth Planet. Sci. **42**, 291–316 (2014)

B.L. Ehlmann, J.F. Mustard, S.L. Murchie, J.-P. Bibring, A. Meunier, A.A. Fraeman, Y. Langevin, Subsurface water and clay mineral formation during the early history of Mars. Nature **479**, 53–60 (2011). doi:10.1038/nature10582

W. Folkner et al., The Rotation and Interior Structure Experiment (RISE) for the InSight mission to Mars, in *43rd Lunar and Planetary Science* (Lunar and Planetary Institute, Houston, 2012). Abstract #1721

W.C. Feldman et al., The global distribution of near-surface hydrogen on Mars. J. Geophys. Res. **109**, E09006 (2004a). doi:10.1029/2003JE002160

W.C. Feldman, M.T. Mellon, S. Maurice, H. Prettyman et al., Hydrated states of $MgSO_4$ at equatorial latitudes on Mars. Geophys. Res. Lett. **31**, L16702 (2004b). doi:10.1029/2004GL020181

R.L. Fergason, P.R. Christensen, H.H. Kieffer, High-resolution thermal inertia derived from the Thermal Emission Imaging System (THEMIS): thermal model and applications. J. Geophys. Res. **111**, E12004 (2006a). doi:10.1029/2006JE002735

R.L. Fergason, P.R. Christensen, J.F. Bell III, M.P. Golombek, K.E. Herkenhoff, H.H. Kieffer, Physical properties of the Mars Exploration Rover landing sites as inferred from Mini-TES derived thermal inertia. J. Geophys. Res. **111**(E2), E02S21 (2006b). doi:10.1029/2005JE002583

R.L. Fergason, P.R. Christensen, M.P. Golombek, T.J. Parker, Surface properties of the Mars Science Laboratory candidate landing sites: characterization from orbit and predictions. Space Sci. Rev. **170**, 739–773 (2012). doi:10.1007/s11214-012-9891-3

R.L. Fergason, R.L. Kirk, G. Cushing, D.M. Galuzska, M.P. Golombek, T.M. Hare, E. Howington-Kraus, D.M. Kipp, B.L. Redding, Generation of digital elevation models and analysis of local slopes at the InSight landing site region. Space Sci. Rev. (2016, this issue). doi:10.1007/s11214-016-0292-x

H.V. Frey, Impact constraints on, and a chronology for, major events in early Mars history. J. Geophys. Res. **111**, E08S91 (2006). doi:10.1029/2005JE002449

J.B. Garvin, J.J. Frawley, J.B. Abshire, Vertical roughness of Mars from Mars Orbiter Laser Altimeter. Geophys. Res. Lett. **26**, 381–384 (1999)

J.B. Garvin, S.E.H. Sakimoto, J.J. Frawley, Craters on Mars: global geometric properties from gridded MOLA topography, in *6th International Conference on Mars* (Lunar and Planetary Institute, Houston, 2003). Abstract #3277

J.J. Gilvarry, Fracture of brittle solids I. Distribution function for fragment size in single fracture (theoretical). J. Appl. Phys. **32**, 391–399 (1961)

J.J. Gilvarry, B.H. Bergstrom, Fracture of brittle solids II. Distribution function for fragment size in single fracture (experimental). J. Appl. Phys. **32**, 400–410 (1961)

M.P. Golombek, R.J. Phillips, Mars Tectonics, in *Planetary Tectonics*, ed. by T.R. Watters, R.A. Schultz (Cambridge University Press, Cambridge, 2010), pp. 183–232, Chap. 5

M. Golombek, D. Rapp, Size-frequency distributions of rocks on Mars and Earth analog sites: Implications for future landed missions. J. Geophys. Res. **102**, 4117–4129 (1997)

M.P. Golombek, R.A. Cook, H.J. Moore, T.J. Parker, Selection of the Mars Pathfinder landing site. J. Geophys. Res. **102**, 3967–3988 (1997)

M.P. Golombek et al., Selection of the Mars Exploration Rover landing sites. J. Geophys. Res. **108**(E12), 8072 (2003a). doi:10.1029/2003JE002074

M.P. Golombek, A.F.C. Haldemann, N.K. Forsberg-Taylor, E.N. DiMaggio, R.D. Schroeder, B.M. Jakosky, M.T. Mellon, J.R. Matijevic, Rock size-frequency distributions on Mars and implications for Mars Exploration Rover landing safety and operations. J. Geophys. Res. **108**(E12), 8086 (2003b). doi:10.1029/2002JE002035

M.P. Golombek et al., Assessment of Mars Exploration Rover landing site predictions. Nature **436**, 44–48 (2005). doi:10.1038/nature03600

M.P. Golombek et al., Geology of the Gusev cratered plains from the Spirit rover traverse. J. Geophys. Res. **110**, E02S07 (2006). doi:10.1029/2005JE002503

M.P. Golombek et al., Size-frequency distributions of rocks on the northern plains of Mars with special reference to Phoenix landing surfaces. J. Geophys. Res. **113**, E00A09 (2008b). doi:10.1029/2007JE003065

M.P. Golombek, A.F.C. Haldemann, R.A. Simpson, R.L. Fergason, N.E. Putzig, R.E. Arvidson, J.F. Bell III, M.T. Mellon, Martian surface properties from joint analysis of orbital, Earth-based, and surface observations, in *The Martian Surface: Composition, Mineralogy and Physical Properties*. ed. by J.F. Bell III (Cambridge University Press, Cambridge, 2008a), pp. 468–497 Chap. 21

M. Golombek, J. Grant, D.D. Kipp, A. Vasavada, R. Kirk, R. Fergason, P. Bellutta, F. Calef, K. Larsen, Y. Katayama, A. Huertas, R. Beyer, A. Chen, T. Parker, B. Pollard, S. Lee, R. Hoover, H. Sladek, J. Grotzinger, R. Welch, E. Noe Dobrea, J. Michalski, M.M. Watkins, Selection of the Mars Science Laboratory landing site. Space Sci. Rev. **170**, 641–737 (2012a). doi:10.1007/s11214-012-9916-y

M. Golombek, A. Huertas, D. Kipp, F. Calef, Detection and characterization of rocks and rock size-frequency distributions at the final four Mars Science Laboratory landing sites. Mars **7**, 1–22 (2012b). doi:10.1555/mars.2012.0001

M. Golombek, L. Redmond, H. Gengl, C. Schwartz, N. Warner, B. Banerdt, S.S. Smrekar, Selection of the InSight landing site: constraints, plans, and progress, in *44th Lunar and Planetary Science* (Lunar and Planetary Institute, Houston, 2013a). Abstract #1691

M. Golombek, N. Warner, C. Schwartz, J. Green, Surface characteristics of prospective InSight landing sites in Elysium Planitia, in *44th Lunar and Planetary Science* (Lunar and Planetary Institute, Houston, 2013b). Abstract #1696

M. Golombek, C. Bloom, N. Wigton, N. Warner, Constraints on the age of Corinto crater from mapping secondaries in Elysium Planitia on Mars, in *45th Lunar and Planetary Science* (Lunar and Planetary Institute, Houston, 2014b). Abstract #1470

M.P. Golombek, N.H. Warner, V. Ganti, M.P. Lamb, T.J. Parker, R.L. Fergason, R. Sullivan, Small crater modification on Meridiani Planum and implications for erosion rates and climate change on Mars. J. Geophys. Res. **119**, 2522–2547 (2014c). 10 Dec. 2014. doi:10.1002/2014JE004658

M. Golombek, N. Warner, N. Wigton, C. Bloom, C. Schwartz, S. Kannan, D. Kipp, A. Huertas, B. Banerdt, Final four landing sites for the InSight geophysical lander, in *45th Lunar and Planetary Science* (Lunar and Planetary Institute, Houston, 2014a). Abstract #1499

M. Golombek, N. Warner, I.J. Daubar, D. Kipp, R. Fergason, R. Kirk, A. Huertas, R. Beyer, S. Piqueux, N.E. Putzig, F. Calef, W.B. Banerdt, Surface and subsurface characteristics of western Elysium Planitia, Mars, in *47th Lunar and Planetary Science* (Lunar and Planetary Institute, Houston, 2016). Abstract #1572

J. Gomez-Elvira et al., REMS: the environmental sensor suite for the mars science laboratory rover. Space Sci. Rev. **2012**, 1–58 (2012)

J.A. Grant, S.A. Wilson, S.W. Ruff, M.P. Golombek, D.L. Koestler, Distribution of rocks on the Gusev plains and on Husband Hill, Mars. Geophys. Res. Lett. **33**, L16202 (2006). doi:10.1029/2006GL026964

R. Greeley, J.D. Iversen, J.B. Pollack, N. Udovich, B. White, Wind tunnel simulations of light and dark streaks on Mars. Science **183**, 847–849 (1974)

R. Greeley, R.O. Kuzmin, S.C. Rafkin, T.I. Michaels, R. Haberle, Wind-related features in Gusev crater, Mars. J. Geophys. Res. **108**(E12) (2003). doi:10.1029/2002je002006

T.K.P. Gregg, J.H. Fink, R.W. Griffiths, Formation of multiple fold generations on lava flow surfaces: influence on strain rate, cooling rate and lava composition. J. Volcanol. Geophys. Res. **80**, 281–292 (1998)

C. Grima, W. Kofman, A. Herique, R. Orosei, R. Seu, Quantitative analysis of Mars surface radar reflectivity at 20 MHz. Icarus **220**, 84–89 (2012). doi:10.1016/j.icarus.2012.04.017

C. Grima, D.M. Schroeder, D.D. Blankenship, D.A. Young, Planetary landing-zone reconnaissance using ice-penetrating radar data: concept validation in Antarctica. Planet. Space Sci. **103**, 191–204 (2014). doi:10.1016/j.pss.2014.07.018

J.P. Grotzinger et al., A habitable fluvio-lacustrine environment at Yellowknife Bay, Gale crater, Mars. Science **343**(6169), 1242777 (2014). doi:10.1126/science.1242777

K. Gwinner, F. Scholten, M. Spiegel, R. Schmidt, B. Giese, J. Oberst, R. Jaumann, C. Heipke, G. Neukum, Derivation and validation of high-resolution digital terrain models from Mars Express HRSC-data. Photogramm. Eng. Remote **75**(9), 1127–1142 (2009)

K. Gwinner, F. Scholten, F. Preusker, S. Elgner, T. Roatsch, M. Spiegel, R. Schmidt, J. Oberst, R. Jaumann, C. Heipke, Topography of Mars from global mapping by HRSC high-resolution digital terrain models and orthoimages: characteristics and performance. Earth Planet. Sci. Lett. **294**, 506–519 (2010a). doi:10.1016/j.epsl.2009.11.007

K. Gwinner, J. Oberst, R. Jaumann, G. Neukum, Regional HRSC multi-orbit digital terrain models for the Mars science laboratory candidate landing sites, in *41st Lunar and Planetary Science Conference* (Lunar and Planetary Institute, Houston, 2010b). Abstract #2727

K. Gwinner et al., The High Resolution Stereo Camera (HRSC) of Mars Express and its approach to science analysis and mapping for Mars and its satellites. Planet. Space Sci. (2016). doi:10.1016/j.pss.2016.02.014

J.K. Harmon, R.E. Arvidson, E.A. Guinness, B.A. Campbell, M.A. Slade, Mars mapping with delay-Doppler radar. J. Geophys. Res. **104**, 14065 (1999)

J.K. Harmon, M.C. Nolan, D.I. Husmann, B.A. Campbell, Arecibo radar imagery of Mars: the major volcanic provinces. Icarus **220**, 990–1030 (2012)

W.K. Hartmann, Does crater "equilibrium" occur in the Solar System? Icarus **60**, 56–74 (1984)

W.K. Hartmann, Martian cratering 8: isochron refinement and the chronology of Mars. Icarus **174**, 294–320 (2005)

W.K. Hartmann, G. Neukum, Cratering chronology and the evolution of Mars. Space Sci. Rev. **96**, 165–194 (2001)

W.K. Hartmann, J. Anguita, M. de la Casa, D. Berman, E.V. Ryan, Martian cratering 7: the role of impact gardening. Icarus **149**, 37–53 (2001)

W.K. Hartmann, C. Quantin, S.C. Werner, O. Popova, Do young martian ray craters have ages consistent with the crater count system? Icarus **208**(2), 621–635 (2010)

T.L. Heet, R.E. Arvidson, S.C. Cull, M.T. Mellon, K.D. Seelos, Geomorphic and geologic settings of the Phoenix Lander mission landing site. J. Geophys. Res. **114**, E00E04 (2009). doi:10.1029/2009JE003416

J.L. Hollingsworth, R.M. Haberle, J.R. Barnes, A.F.C. Brider, J.B. Pollack, H. Lee, J. Schaeffer, Orographic control of storm zones on Mars. Nature **380**(6573), 413–416 (1996). doi:10.1038/380413a0

J.W. Holt, A. Safaeinili, J.J. Plaut, J.W. Head, R.J. Phillips, R. Seu, S.D. Kempf, P. Choudhary, D.A. Young, N.E. Putzig, Radar sounding evidence for buried glaciers in the southern mid-latitudes of Mars. Science **322**, 1235–1238 (2008)

B.K.P. Horn, Hill shading and the reflectance map. Proc. IEEE **69**, 14–47 (1981)
E. Howington-Kraus, R.L. Fergason, R.L. Kirk, D. Galuszka, B. Redding, M. Theobald, E. Littlefield, S. Sutton, A. Fennema, D. Kipp, R.E. Otero, M.P. Golombek, High-resolution topographic mapping supporting selection of NASA's next Mars landing sites, in *46th Lunar and Planetary Science* (Lunar and Planetary Institute, Houston, 2015). Abstract #2435
B.A. Ivanov, Mars/Moon cratering ratio estimates. Space Sci. Rev. **96**, 87–104 (2001)
B.M. Jakosky, On the thermal properties of Martian fines. Icarus **66**, 117–124 (1986)
B.M. Jakosky, P.R. Christensen, Global duricrust on Mars: analysis of remote-sensing data. J. Geophys. Res. **91**, 3547–3559 (1986)
R. Jaumann, G. Neukum, T. Behnke, T.C. Duxbury, E. Eichentopf, H. Hoffmann, A. Hoffmeister, U. Köhler, K-D. Matz, T.B. McCord, V. Mertens, J. Oberst, R. Pischel, D. Reiss, E. Ress, T. Roatsch, P. Saiger, F. Scholten, G. Schwartz, K. Stephan, M. Wählisch, the HRSC Co-Investigation Team, The High-Resolution Stereo Camera (HRSC) experiment on the Mars Express: instrument aspects and experiment conduct from interplanetary cruise through the nominal mission. Planet. Space Sci. **55**, 928–952 (2007)
E. Jones, G. Caprarelli, F.P. Mills, B. Doran, J. Clarke, An alternative approach to mapping thermophysical units from martian thermal inertia and albedo data using a combination of unsupervised classification techniques. Remote Sens. **6**, 5184–5237 (2014). doi:10.3390/rs6065184
D.M. Kass, J.T. Schofield, T.I. Michaels, S.C.R. Rafkin, M.I. Richardson, A.D. Toigo, Analysis of atmospheric mesoscale models for entry, descent, and landing. J. Geophys. Res. **108**(E12), 8090 (2003). doi:10.1029/2003JE002065
D.M. Kass, A. Kleinböhl, D.J. McCleese, J.T. Schofield, M.D. Smith, Interannual similarity in the Martian atmosphere during the dust storm season. Geophys. Res. Lett. **43**, 6111–6118 (2016). doi:10.1002/2016GL068978
D.G. Kendall, Stochastic processes and population growth. J. R. Stat. Soc. **11**(2), 230–282 (1949)
H.H. Kieffer, Thermal model for analysis of Mars infrared mapping. J. Geophys. Res. **118**(3), 451–470 (2013)
H.H. Kieffer, S.C. Chase Jr., E. Miner, G. Münch, G. Neugebauer, Preliminary report on infrared radiometric measurements from the Mariner 9 spacecraft. J. Geophys. Res. **78**(20), 4291–4312 (1973)
H.H. Kieffer, T.Z. Martin, A.R. Peterfreund, B.M. Jakosky, E.D. Miner, F.D. Palluconi, Thermal and albedo mapping of Mars during the Viking primary mission. J. Geophys. Res. **82**(28), 4249–4291 (1977)
H.H. Kieffer, B.M. Jakosky, C.W. Snyder, M.S. Matthews (eds.), *Mars* (The University of Arizona Press, Tuscon, 1992). 1498 pp.
Kim, J.P. Muller, Multi-resolution topographic data extraction from Martian stereo imagery. Planet. Space Sci. **57**(14–15), 2095–2112 (2009). doi:10.1016/j.pss.2009.09.024
R. Kirk et al., High-resolution topomapping of candidate MER landing sites with Mars Orbiter Camera narrow angle images. J. Geophys. Res. **108**(E12), 8088 (2003). doi:10.1029/2003JE002131
R.L. Kirk et al., Ultrahigh resolution topographic mapping of Mars with MRO HiRISE stereo images: meter-scale slopes of candidate Phoenix landing sites. J. Geophys. Res. **113**, E00A24 (2008). doi:10.1029/2007JE003000
R.L. Kirk et al., Near-complete 1-m topographic models of the MSL candidate landing sites: site safety and quality evaluation, in *European Planetary Science Conference*, vol. 6 (2011). Abstract EPSC2011-1465
R.L. Kirk et al., The effect of incidence angle on stereo DTM quality: simulations in support of Europa exploration, in *ISPRS Commission IV, WG IV/8*, Prague, Czech Republic (2016)
M.A. Kreslavsky, J.W. Head III, Kilometer-scale roughness of Mars: results from MOLA data analysis. J. Geophys. Res. **105**, 26695–26711 (2000).
M. Lisano, D. Bernard, An almanac of martian dust storms for InSight Project energy system design, in *Aerospace Conference* (2014). doi:10.1109/AERO.2014.6836269. IEEE XPlore, 15 pp.
P. Lognonné, C. Johnson, Planetary seismology, in *Treatise in Geophysics*, ed. by G. Schubert. Planets and Moons, vol. 10 (Elsevier, Amsterdam, 2007), pp. 67–122
P. Lognonné, B. Mosser, Planetary seismology. Surv. Geophys. **14**, 239–302 (1993). doi:10.1007/BF00690946
P. Lognonné et al., Science Goals of the SEIS, the InSight Seismometer Package, in *46th Lunar and Planetary Science* (Lunar and Planetary Institute, Houston, 2015). Abstract #2272
B. Lu, S. Torquato, Chord-length and free-path distribution functions for many-body systems. J. Chem. Phys. **98**(8), 6472–6482 (1993)
M.C. Malin et al., Context Camera Investigation on board the Mars Reconnaissance Orbiter. J. Geophys. Res. **112**, E05S04 (2007). doi:10.1029/2006JE002808
N. Mangold, V. Ansan, P. Masson, C. Vincendon, Estimate of the aeolian dust thickness in Arabia Terra, Mars: Implications of a thick mantle (20 m) for hydrogen detection. Géomorphol., Relief Process. Environ. **1**, 23–32 (2009)

D.J. McCleese, J.T. Schofield, F.W. Taylor, S.B. Calcutt, M.C. Foote, D.M. Kass, C.B. Leovy, D.A. Paige, P.L. Read, R.W. Zurek, Mars climate Sounder: an investigation of thermal and water vapor structure, dust and condensate distributions in the atmosphere, and energy balance of the polar regions. J. Geophys. Res. **112**, E05S06 (2007). doi:10.1029/2006JE002790

D.J. McCleese, N.G. Heavens, J.T. Schofield, W.A. Abdou, J.L. Bandfield, S.B. Calcutt, P.G.J. Irwin, D.M. Kass, A. Kleinbohl, C.B. Leovy, S.R. Lewis, D.A. Paige, P.L. Read, M.I. Richardson, J.H. Shirley, F.W. Taylor, N. Teanby, R.W. Zurek, The structure and dynamics of the martian lower and middle atmosphere as observed by the Mars Climate Sounder: 1. Seasonal variations in zonal mean temperature, dust and water ice aerosols. J. Geophys. Res. **115**, E12016 (2010). doi:10.1029/2010JE003677

A. McEwen, B. Preblich, E. Turtle, N. Artemieva, M. Golombek, M. Hurst, R. Kirk, D. Burr, P. Christensen, The rayed crater Zunil and interpretations of small impact craters on Mars. Icarus **176**, 351–381 (2005). doi:10.1016/j.icarus.2005.02.009

A.S. McEwen et al., Mars Reconnaissance Orbiter's High Resolution Imaging Science Experiment (HiRISE). J. Geophys. Res. **112**, E05S02 (2007). doi:10.1029/2005JE002605

A.S. McEwen et al., The High Resolution Imaging Science Experiment (HiRISE) during MRO's Primary Science Phase (PSP). Icarus **205**, 2–37 (2010). doi:10.1016/j.icarus.2009.04.023

A.S. McEwen et al., For the people: HIRISE data products, in *44th Lunar and Planetary Science* (Lunar and Planetary Institute, Houston, 2016). Abstract #1371

G.E. McGill, A.M. Dimitriou, Origin of the Martian global dichotomy by crustal thinning in the Late Noachian or Early Hesperian. J. Geophys. Res. **95**, 12,595–12,605 (1990)

M. Mehta et al., Explosive erosion during the Phoenix landing exposes subsurface water on Mars. Icarus **211**, 172–194 (2011). doi:10.1016/j.icarus.2010.10.003

M.T. Mellon, B.M. Jakosky, H.H. Kieffer, P.R. Christensen, High-resolution thermal inertia mapping from the Mars Global Surveyor Thermal Emission Spectrometer. Icarus **148**, 437–455 (2000)

M.T. Mellon et al., The thermal inertia of the surface of Mars, in *The Martian Surface: Composition, Mineralogy and Physical Properties*, ed. by J.F. Bell III (Cambridge University Press, Cambridge, 2008), pp. 399–427, Chap. 19

H.J. Melosh, *Impact Craters: A Geologic Process* (Oxford University Press, London, 1989)

D. Mimoun et al., The seismic noise model of the InSight mission to Mars. Space Sci. Rev. (2016, this issue), submitted

I.G. Mitrofanov et al., Soil water content on Mars as estimated from neutron measurements by HEND instrument onboard 2001 Mars Odyssey spacecraft. Sol. Syst. Res. **38**, 253–265 (2004)

L. Montabone et al., Eight-year climatology of dust optical depth on Mars. Icarus **251**, 65–95 (2015). doi:10.1016/j.icarus.2014.12.034

H.J. Moore, B.M. Jakosky, Viking landing sites, remote-sensing observations, and physical properties of martian surface materials. Icarus **81**, 164–184 (1989)

H.J. Moore, J.M. Keller, Surface-material maps of Viking landing sites on Mars. Reports of Planetary Geology and Geophysics Program—1989 (1990), NASA Tech. Memo., TM-4210, pp. 533–535

H.J. Moore, J.M. Keller, Surface-material maps of Viking landing sites on Mars. Reports of Planetary Geology and Geophysics Program—1990 (1991), NASA Tech. Memo., TM-4300, pp. 160–162

Z.M. Moratto, M.J. Broxton, R.A. Beyer, M. Lundy, K. Husmann, Ames stereo pipeline, NASA's open source automated stereogrammetry software, in *Lunar Planet Sci. XLI* (Lunar and Planetary Institute, Houston, 2010). Abstract #2364

G.A. Morgan, B.A. Campbell, L.M. Carter, J.J. Plaut, R.J. Phillips, 3D reconstruction of the source and scale of buried young flood channels on Mars. Science **340**, 607–610 (2013). doi:10.1126/science.1234787

G.A. Morgan, B.A. Campbell, L.M. Carter, J.J. Plaut, Evidence for the episodic erosion of the Medusae Fossae Formation preserved within the youngest volcanic province on Mars. Geophys. Res. Lett. **42**(18), 7336–7342 (2015). http://doi.org/10.1002/2015GL065017

J. Mouginot, A. Pommerol, P. Beck, W. Kofman, S.M. Clifford, Dielectric map of the Martian northern hemisphere and the nature of plain filling materials. Geophys. Res. Lett. **39**, L02202 (2012). doi:10.1029/2011GL050286

K. Mueller, M.P. Golombek, Compressional structures on Mars. Annu. Rev. Earth Planet. Sci. **32**, 435–464 (2004)

N. Murdock, D. Mimoun, R.F. Garcia, T. Kawamura, P. Lognonné, Evaluating the wind-induced mechanical noise on the InSight seismometers. Space Sci. Rev. (2016, this issue). doi:10.1007/s11214-016-0311-y

N.W. Murphy, B.M. Jakosky, S.C. Rafkin, K.W. Larsen, N.E. Putzig, M.T. Mellon, Thermophysical properties of the Isidis basin, Mars. J. Geophys. Res. **112**, E05004 (2007). doi:10.1029/2005JE002586

M. Natarajan, A.D. Cianciolo, T.D. Fairlie, M.I. Richardson, T.H. McConnochie, Sensitivity of simulated Martian atmospheric temperature to prescribed dust opacity distribution: comparison of model results with reconstructed data from Mars Exploration Rover missions. J. Geophys. Res. **120**, 11 (2015). doi:10.1002/2015JE004813

G. Neukum, R. Jaumann, the HRSC Co-Investigator Team, HRSC, The high resolution stereo camera of Mars express. ESA special publications, SP-1240 (2004)
G.A. Neumann, J.B. Abshire, O. Aharonson, J.B. Garvin, X. Sun, M.T. Zuber, Mars Orbiter Laser Altimeter pulse width measurements and footprint scale roughness. Geophys. Res. Lett. **30**, 1561–1565 (2003)
S.A. Nowicki, P.R. Christensen, Rock abundance on Mars from the Thermal Emission Spectrometer. J. Geophys. Res. **112**, E05007 (2007). doi:10.1029/2006JE002798
F.D. Palluconi, H.H. Kieffer, Thermal inertia mapping of Mars from 60°S to 60°N. Icarus **45**, 415–426 (1981)
T.J. Parker, D. Gorsline, R.S. Saunders, D. Pieri, D. Schneeberger, Coastal geomorphology of the martian northern plains. J. Geophys. Res. **98**(E6), 11061–11078 (1993)
R.J. Pike, Control of crater morphology by gravity and target type: Mars, Earth, Moon, in *11th Lunar Planet. Sci. Conf.* (1980), pp. 2159–2189
R.J. Pike, D.E. Wilhelms, Secondary-impact craters on the Moon: topographic form and geologic process, in *9th Lunar Planet. Sci. Conf.* (1978), pp. 907–909
S. Piqueux, P.R. Christensen, A model of thermal conductivity for planetary soils: 2. Theory for cemented soils. J. Geophys. Res. **114**, E09006 (2009). doi:10.1029/2008je003309
S. Piqueux, P.R. Christensen, Temperature-dependent thermal inertia of homogeneous Martian regolith. J. Geophys. Res. **116**, E07004 (2011). doi:10.1029/2011je003805
S. Piqueux, A. Kleinboehl, M.P. Golombek, Thermal inertia mapping using Climate Sounder measurements, in *Fall Meeting*, Dec. 15–19, 2014 (American Geophys. Un., San Francisco, 2014). Abstract P32A-4021
A. Pivarunas, N.H. Warner, M.P. Golombek, Onset diameter of rocky ejecta craters in western Elysium Planitia, Mars: Constraints for regolith thickness at the InSight landing site, in *46th Lunar and Planetary Science* (Lunar and Planetary Institute, Houston, 2015). Abstract #1129
L.K. Pleskot, E.D. Miner, Time variability of Martian bolometric albedo. Icarus **45**, 179–201 (1981)
B.S. Preblich, A.S. McEwen, D.M. Studer, Mapping rays and secondary craters from the Martian crater Zunil. J. Geophys. Res. **112**, E05006 (2007). doi:10.1029/2006JE002817
M.A. Presley, P.R. Christensen, Thermal conductivity measurements of particulate materials, Part II: Results. J. Geophys. Res. **102**, 6551–6566 (1997a)
M.A. Presley, P.R. Christensen, Thermal conductivity measurements of particulate materials, Part I: A review. J. Geophys. Res. **102**, 6535–6549 (1997b)
N.E. Putzig, M.T. Mellon, Apparent thermal inertia and the surface heterogeneity of Mars. Icarus **191**(1), 68–94 (2007a). doi:10.1016/j.icarus.2007.1005.1013
N.E. Putzig, M.T. Mellon, Thermal behavior of horizontally mixed surfaces on Mars. Icarus **191(1)**, 52–67 (2007b). doi:10.1016/j.icarus.2007.1003.1022
N.E. Putzig, M.T. Mellon, R.E. Arvidson, K.A. Kretke, Global thermal inertia and surface properties of Mars from the MGS mapping mission. Icarus **173**, 325–341 (2005)
N.E. Putzig, R.J. Phillips, B.A. Campbell, J.W. Holt, J.J. Plaut, L.M. Carter, A.F. Egan, F. Bernardini, A. Safaeinili, R. Seu, Subsurface structure of Planum Boreum from Mars Reconnaissance Orbiter Shallow Radar soundings. Icarus **204**, 443–457 (2009)
N.E. Putzig, R.J. Phillips, B.A. Campbell, M.T. Mellon, J.W. Holt, B.J. Davis, T.C. Brothers, Shallow Radar soundings and surface roughness at past, present, and proposed landing sites on Mars. J. Geophys. Res. **119**, 1936–1949 (2014). doi:10.1002/2014JE004646
N.E. Putzig, G.A. Morgan, B.A. Campbell, C. Grima, I.B. Smith, R.J. Phillips, M. Golombek, Radar properties of the proposed InSight landing site in western Elysium Planitia on Mars, in *47th Lunar Planetary Science* (Lunar and Planetary Institute, Houston, 2016). Abstract #1655
N.E. Putzig, G.A. Morgan, B.A. Campbell, C. Grima, I.B. Smith, R.J. Phillips, Radar-Derived Properties of the InSight Landing Site in Western Elysium Planitia on Mars. Space Sci. Rev. (2016, this issue). doi:10.1007/s11214-016-0322-8
S.C. Rafkin, R.M. Haberle, T.I. Michaels, The Mars Regional Atmospheric Modeling System (MRAMS): model description and selected simulations. Icarus **151**, 228–256 (2001). doi:10.1006/icar.2001.6605
S.C.R. Rafkin, T.I. Michaels, Meteorological predictions for 2003 Mars Exploration Rover high-priority landing sites. J. Geophys. Res. **108**(E12), 8091 (2003). doi:10.1029/2002JE002027
M.A. Ravine, R.A.F. Grieve, An analysis of morphologic variations in simple lunar craters, J. Geophys. Res, **81**, E75–E83 (1986). Proc. 17th Lunar Planet. Sci. Conf.
J.J. Rennilson, J.L. Dragg, E.C. Morris, E.M. Shoemaker, A. Turkevich, Lunar surface topography. Surveyor I mission report, part II: Scientific data and results. NASA JPL Technical Report #32-1023, p. 7–44 (1966)
P. Rosin, E. Rammler, The laws governing the fineness of powdered coal. J. Inst. Fuel **7**, 29–36 (1933)
S. Ruff, P.R. Christensen, Bright and dark regions on Mars: particle size and mineralogical characteristics based on Thermal Emission Spectrometer data. J. Geophys. Res. **107**(E12), 5127 (2002). doi:10.1029/2001JE001580

J.D. Rummel et al., A new analysis of Mars "special regions": findings of the second MEPAG special regions science analysis group (SR-SAG2). Astrobiology **14**(11), 887–968 (2014). doi:10.1089/ast.2014.1227
P.S. Russell, J.A. Grant, K.K. Williams, L.M. Carter, W. Brent Garry, I.J. Daubar, Ground penetrating radar geologic field studies of the ejecta of Barringer Meteorite Crater, Arizona, as a planetary analog. J. Geophys. Res. **118**, 1915–1933 (2013). doi:10.1002/jgre.20145
P. Schultz, J. Singer, A comparison of secondary craters on the Moon, Mercury, and Mars, in *11th Lunar Planet. Sci. Conf.* (1980), pp. 2243–2259
R. Seu, D. Biccari, R. Orosei, L.V. Lorenzoni, R.J. Phillips, L. Marinangeli, G. Picardi, A. Masdea, E. Zampolini, SHARAD: the MRO 2005 shallow radar. Planet. Space Sci. **52**, 157–166 (2004)
R. Seu, R.J. Phillips, D. Biccari, R. Orosei, A. Masdea, G. Picardi, A. Safaeinili, B.A. Campbell, J.J. Plaut, L. Marinangeli, S.E. Smrekar, D.C. Nunes, SHARAD sounding radar on the Mars Reconnaissance Orbiter. J. Geophys. Res. **112**(E5), E05S05 (2007). doi:10.1029/2006JE002745
E.M. Shoemaker, E.C. Morris, Thickness of the regolith, in *Surveyor: Program Results*, NASA Special Paper, vol. 184 (U.S. Government Printing Office, Washington, 1969), pp. 96–98
D.E. Smith et al., Mars Orbiter Laser Altimeter (MOLA): experiment summary after the first year of global mapping of Mars. J. Geophys. Res. **106**, 23,689–23,722 (2001b)
M.D. Smith, J.C. Pearl, B.J. Conrath, P.R. Christensen, Thermal Emission Spectrometer results: Mars atmospheric thermal structure and aerosol distribution. J. Geophys. Res. **106**(E10), 23929–23945 (2001a)
G.G. Sorrells, J.A. McDonald, Z.A. Der, E. Herrin, Earth motion caused by local atmospheric pressure changes. Geophys. J. R. Astron. Soc. **26**, 83–98 (1971)
D.A. Spencer, D.S. Adams, E. Bonfiglio, M. Golombek, R. Arvidson, K. Seelos, Phoenix landing site hazard assessment and selection. J. Spacecr. Rockets **46**(6), 1196–1201 (2009). doi:10.2514/1.43932
M. Spiegel, Kombinierte Ausgleichung der Mars Express HRSC Zeilenbilddaten und des Mars Global Surveyor MOLA DGM. PhD thesis, DGK-C, 610 (Deutsche Geodätische Kommission, Munich, 2007)
A. Spiga, F. Forget, A new model to simulate the Martian mesoscale and microscale atmospheric circulation: validation and first results. J. Geophys. Res. **114**, E02009 (2009). doi:10.1029/2008JE003242
T. Spohn et al., InSight: Measuring the martian heat flow using the Heat Flow and Physical Properties Package (HP^3), in *43rd Lunar Planetary Science* (Lunar and Planetary Institute, Houston, 2012). Abstract #1445
S.W. Squyres et al., Ice in the Martian regolith, in *MARS*, ed. by H.H. Kieffer, B.M. Jakosky, C.W. Snyder, M.S. Matthews (University of Arizona Press, Tucson, 1992), pp. 523–554. Chap. 16, 1498 pp.
L.J. Steele, S.R. Lewis, M.R. Patel, The radiative impact of water ice clouds from a reanalysis of Mars Climate Sounder data. Geophys. Res. Lett. **41**(13), 4471–4478 (2014). doi:10.1002/2014gl060235
P.M. Stella, J.A. Herman, The Mars surface and solar array performance, in *35th IEEE Photovoltaic Specialists Conference*, Honolulu, 20–25 June 2010 (2010), pp. 002631–002635. doi:10.1109/PVSC.2010.5617185
R. Sullivan et al., Aeolian processes at the Mars Exploration Rover Meridiani Planum landing site. Nature **436**, 58–61 (2005, July). doi:10.1038/nature03641
S. Sutton et al., HIRISE digital terrain models: updates and advances, in *2nd Planetary Data Workshop*, Flagstaff, AZ, June 8–11, 2015 (Lunar and Planetary Institute, Houston, 2015). Abstract #7056
J. Sweeney, N.H. Warner, M.P. Golombek, R. Kirk, R.L. Fergason, A. Pivarunas, Crater degradation and surface erosion rates at the InSight landing site, western Elysium Planitia, Mars, in *47th Lunar Planetary Science* (Lunar and Planetary Institute, Houston, 2016). Abstract #1576
L.K. Tamppari, J. Barnes, E. Bonfiglio, B. Cantor, A.J. Friedson, A. Ghosh, M.R. Grover, D. Kass, T.Z. Martin, M. Mellon, T. Michaels, J. Murphy, S.C.R. Rafkin, M.D. Smith, G. Tsuyuki, D. Tyler Jr., M. Wolff, Expected atmospheric environment for the Phoenix landing season and location. J. Geophys. Res. **113**, E00A20 (2008). doi:10.1029/2007JE003034
K. Tanaka et al., Geologic map of Mars. U.S. Geol. Surv. Sci. Invest. Map 3292 (2014)
T.W. Thompson, W.J. Roberts, W.K. Hartmann, R.W. Shorthill, S.H. Zisk, Blocky craters—implications about the lunar megaregolith. Moon Planets **21**, 319–342 (1979)
A.D. Toigo, M.I. Richardson, Meteorology of proposed Mars Exploration Rover landing sites. J. Geophys. Res. **108**(E12), 8092 (2003). doi:10.1029/2003JE002064
L.L. Tornabene, J.E. Moersch, H.Y. McSween, A.S. McEwen, J.L. Piatek, K.A. Milam, P.R. Christensen, Identification of large (2–10 km) rayed craters on Mars in THEMIS thermal infrared images: implications for possible Martian meteorite source regions. J. Geophys. Res. **111**, E10006 (2006). doi:10.1029/2005JE002600
L.L. Tornabene, V. Ling, G.R. Osinski, J.M. Boyce, T.N. Harrison, A.S. McEwen, A revised global depth-diameter scaling relationship for Mars based on pitted impact melt-bearing craters, in *44th Lunar Planetary Science Conference* (Lunar and Planetary Institute, Houston, 2013). Abstract #2592
D.L. Turcotte, *Fractals and Chaos in Geology and Geophysics*, 2nd edn. (Cambridge U. Press, Cambridge, 1997)

D. Tyler Jr., J.R. Barnes, R.M. Haberle, Simulation of surface meteorology at the Pathfinder and VL1 sites using a Mars mesoscale model. J. Geophys. Res. **107**(E4), 5018 (2002). doi:10.1029/2001JE001618

J. Vaucher, D. Baratoux, N. Mangold, P. Pinet, K. Kurita, M. Grégoire, The volcanic history of central Elysium Planitia: implications for martian magmatism. Icarus **204**, 418–442 (2009)

H. Wang, M.I. Richardson, The origin, evolution, and trajectory of large dust storms on Mars during Mars years 24–30 (1999–2011). Icarus **251**, 112–127 (2015). doi:10.1016/j.icarus.2013.10.033

N.H. Warner, T.K.P. Gregg, Evolved lavas on Mars? Observations from southwest Arsia Mons and Sabancaya volcano. Peru. J. Geophys. Res. **108** (2003). doi:10.1029/2002JE001969

N.H. Warner, M.P. Golombek, C. Bloom, N. Wigton, C. Schwartz, Regolith thickness in western Elysium Planitia: Constraints for the InSight mission, in *45th Lunar Planetary Science* (Lunar and Planetary Institute, Houston, 2014). Abstract #2217

N.H. Warner, M.P. Golombek, J. Sweeney, A. Pivarunas, Regolith thickness estimates from the size frequency distribution of rocky ejecta craters in southwestern Elysium Planitia, Mars, in *47th Lunar Planetary Science* (Lunar and Planetary Institute, Houston, 2016). Abstract #2231

N.H. Warner, M.P. Golombek, J. Sweeney, R. Fergason, R. Kirk, C. Schwartz Near surface stratigraphy and regolith production in southwestern Elysium Planitia, Mars: implications for Hesperian-Amazonian terrains and the InSight lander mission. Space Sci. Rev. (2016, this issue), submitted

T.R. Watters, B. Campbell, L. Carter, C.J. Leuschen, J.J. Plaut, G. Picardi, R. Orosei, A. Safaeinili, S.M. Clifford, W.M. Farrell, A.B. Ivanov, R.J. Phillips, E.R. Stofan, Radar sounding of the Medusae Fossae Formation Mars: equatorial ice or dry, low-density deposits? Science **318**(5853), 1125–1128 (2007). http://doi.org/10.1126/science.1148112

N.R. Wigton, N. Warner, M. Golombek, Terrain mapping of the InSight landing region: Western Elysium Planitia, Mars, in *45th Lunar and Planetary Science* (Lunar and Planetary Institute, Houston, 2014). Abstract #1234

R.M.E. Williams et al., Martian fluvial conglomerates at Gale crater. Science **340**, 1068–1072 (2013). doi:10.1126/science.1237317

R.J. Wilson, S.D. Guzewich, Influence of water ice clouds on nighttime tropical temperature structure as seen by the Mars Climate Sounder. Geophys. Res. Lett. **41**(10), 3375–3381 (2014). doi:10.1002/2014gl060086

M.M. Withers, R.C. Aster, C.J. Young, E.P. Chael, High-Frequency analysis of seismic background noise as a function of wind speed and shallow depth. Bull. Seismol. Soc. Am. **86**, 1507–1515 (1996)

K.H. Wohletz, M.F. Sheridan, W.K. Brown, Particle size distributions and the sequential fragmentation/transport theory applied to volcanic ash. J. Geophys. Res. **94**, 15,703–15,721 (1989). 1989

C.A. Wood, L. Andersson, New morphometric data for fresh lunar craters, in *9th Proc. Lunar Planet. Sci. Conf.* (1978), pp. 3669–3689

M.T. Zuber, D.E. Smith, S.C. Solomon, D.O. Muhleman, J.W. Head, J.B. Garvin, J.B. Abshire, J.L. Bufton, The Mars Observer Laser Altimeter investigation. J. Geophys. Res. **97**(E5), 7781–7797 (1992). doi:10.1029/2005JE002605

R.W. Zurek, L.J. Martin, Interannual variability of planet-encircling dust storms on Mars. J. Geophys. Res. **98**, 3247–3325 (1993)